

**IMPLEMENTATION OF LES/SFMDF FOR  
PREDICTION OF NON-PREMIXED TURBULENT  
FLAMES**

by

**Tomasz G. Drozda**

B.S. in Mechanical Engineering, University at Buffalo, 1999

B.S. in Aerospace Engineering, University at Buffalo, 1999

M.S. in Mechanical Engineering, University at Buffalo, 2002

Submitted to the Graduate Faculty of  
the School of Engineering in partial fulfillment  
of the requirements for the degree of

**Doctor of Philosophy**

University of Pittsburgh

2005

UNIVERSITY OF PITTSBURGH  
SCHOOL OF ENGINEERING

This dissertation was presented

by

Tomasz G. Drozda

It was defended on

August 25, 2005

and approved by

Dr. Peyman Givi, William Kepler Whiteford Professor of Mechanical Engineering

Dr. Giovanni P. Galdi, Professor of Mechanical Engineering

Dr. William J. Layton, Professor of Mathematics

Dr. Laura A. Schaefer, Assistant Professor of Mechanical Engineering

Dissertation Director: Dr. Peyman Givi, William Kepler Whiteford Professor of  
Mechanical Engineering

Copyright © by Tomasz G. Drozda

2005

# IMPLEMENTATION OF LES/SFMDF FOR PREDICTION OF NON-PREMIXED TURBULENT FLAMES

Tomasz G. Drozda

University of Pittsburgh, 2005

Large eddy simulation (LES) is conducted of two experimental flame configurations. The first is the flame studied in the experiments of the Combustion Research Facility at the Sandia National Laboratories (SNL) and the Technische Universität Darmstadt (TUD), namely Flame D.<sup>1-3</sup> This is a turbulent piloted non-premixed methane jet flame. The second flame is also studied by the Combustion Research Facility at the Sandia National Laboratories and at the Thermal Research Group at the University of Sydney.<sup>4-11</sup> This is a turbulent bluff-body stabilized hydrogen-methane jet flame. The subgrid scale (SGS) closure in LES is based on the scalar filtered mass density function (SFMDF) methodology.<sup>12</sup> The SFMDF is the mass weighted probability density function (PDF) of the SGS scalar quantities.<sup>13</sup> A flamelet model<sup>14,15</sup> is used to relate the scalar composition to the mixture fraction. The modeled SFMDF transport equation is solved by a hybrid finite-difference (FD) / Monte Carlo (MC) scheme. This is the first LES of realistic turbulent flames using the transported PDF method as the SGS closure. The results via this method capture some of the important features of the flames as observed experimentally.

**Keywords:** LES, FDF, PDF, turbulent reacting flows, diffusion flame, non-premixed combustion, subgrid scale closure, Monte Carlo simulation.

## TABLE OF CONTENTS

<b>PREFACE</b> . . . . .	xvi
<b>ACKNOWLEDGMENTS</b> . . . . .	xvii
<b>1.0 INTRODUCTION</b> . . . . .	1
<b>2.0 FORMULATION</b> . . . . .	4
2.1 Governing Equations . . . . .	4
2.2 Scalar Filtered Mass Density Function . . . . .	7
2.3 Stochastic System . . . . .	10
2.4 Chemical Reaction Model . . . . .	11
2.5 Numerical Procedure . . . . .	11
<b>3.0 RESULTS</b> . . . . .	19
3.1 Sandia/TUD Flame . . . . .	19
3.1.1 Configuration . . . . .	19
3.1.2 Numerical Specifications . . . . .	20
3.1.3 Consistency of the LES/SFMDF . . . . .	22
3.1.4 Comparisons with Experimental Data . . . . .	24
3.2 Sydney/Sandia Bluff-Body Flame . . . . .	55
3.2.1 Configuration . . . . .	55
3.2.2 Numerical Specifications . . . . .	57
3.2.3 Comparisons with Experimental Data . . . . .	59
3.2.3.1 Non-Reacting Flows. . . . .	59
3.2.3.2 Reacting Flows. . . . .	62
3.2.3.3 PDF Comparisons. . . . .	64

<b>4.0 CONCLUSION</b> . . . . .	91
<b>APPENDIX. ADDITIONAL LES/SF MDF DATA ON SYDNEY/SANDIA FLAME</b> . . . . .	93
<b>BIBLIOGRAPHY</b> . . . . .	103

## LIST OF TABLES

1	Sandia/TUD: Summary of the LES/SF MDF parameters and reference quantities.	21
2	Sydney/Sandia: Summary of the LES/SF MDF parameters and reference quantities. . . . .	57
3	Sydney/Sandia: Experimental specifications. . . . .	60
4	Sydney/Sandia: Simulation specifications. . . . .	61

## LIST OF FIGURES

1	Ensemble averaging procedure. . . . .	16
2	Ensemble averaging procedure visualization. . . . .	17
3	Contours of the ensembled particle weights and particle number density. . . . .	18
4	Sandia/TUD: Flame Configuration. . . . .	26
5	Sandia/TUD: Radial profiles of the mean and the resolved RMS values of the streamwise velocity at the inlet. . . . .	27
6	Sandia/TUD: Flamelet tables. . . . .	28
7	Sandia/TUD: Instantaneous contours of the mixture fraction. . . . .	29
8	Sandia/TUD: Instantaneous contours of the density. . . . .	30
9	Sandia/TUD: Instantaneous profiles of the density. . . . .	31
10	Sandia/TUD: Scatter plots of the instantaneous values of the mixture fraction. . . . .	32
11	Sandia/TUD: Scatter plots of the time averaged values of the mixture fraction. . . . .	33
12	Sandia/TUD: Instantaneous profiles of the mixture fraction. . . . .	34
13	Sandia/TUD: Temporal evolution of the correlation coefficients computed from the mixture fraction data. . . . .	35
14	Sandia/TUD: Scatter plots of the instantaneous values of the mixture fraction variance. . . . .	36
15	Sandia/TUD: Scatter plots of the time averaged values of the mixture fraction variance. . . . .	37
16	Sandia/TUD: Instantaneous profiles of the mixture fraction variance. . . . .	38
17	Sandia/TUD: Temporal evolution of the correlation coefficients computed from the mixture fraction variance data. . . . .	39

18	Sandia/TUD: Profiles of the mean and the resolved RMS values of the streamwise velocity. . . . .	40
19	Sandia/TUD: Profiles of the mean and the resolved RMS values of the radial velocity. . . . .	41
20	Sandia/TUD: Contours of the mean values of the mixture fraction and temperature. . . . .	42
21	Sandia/TUD: Profiles of the mean and the RMS values of the mixture fraction. . . . .	43
22	Sandia/TUD: Profiles of the mean and the RMS values of the temperature. . . . .	44
23	Sandia/TUD: Profiles of the mean and the RMS values of the methane mass fraction. . . . .	45
24	Sandia/TUD: Profiles of the mean and the RMS values of the water mass fraction. . . . .	46
25	Sandia/TUD: Profiles of the mean and the RMS values of the oxygen mass fraction. . . . .	47
26	Sandia/TUD: Profiles of the mean and the RMS values of the carbon monoxide mass fraction. . . . .	48
27	Sandia/TUD: Profiles of the mean values of the select mass fractions. . . . .	49
28	Sandia/TUD: PDF locations. . . . .	50
29	Sandia/TUD: PDFs of the resolved mixture fraction. . . . .	51
30	Sandia/TUD: PDFs of the resolved temperature. . . . .	52
31	Sandia/TUD: PDFs of the resolved mixture fraction compared to experiment. . . . .	53
32	Sandia/TUD: PDFs of the resolved temperature compared to experiment. . . . .	54
33	Sydney/Sandia: Flame Configuration. . . . .	65
34	Sydney/Sandia: Radial profiles of the mean and the resolved RMS values of the streamwise velocity at the inlet. . . . .	66
35	Sydney/Sandia: Flamelet tables. . . . .	67
36	Sydney/Sandia: Instantaneous and time averaged contours of the mixture fraction for the LES/SFMDF. . . . .	68
37	Sydney/Sandia: Time averaged recirculation features in the non-reacting experiments and simulation. . . . .	69

38	Sydney/Sandia: Instantaneous recirculation features in the non-reacting simulations. . . . .	70
39	Sydney/Sandia: Radial profiles of the mean and the resolved RMS values of the streamwise velocity for the non-reacting flow. . . . .	71
40	Sydney/Sandia: Radial profiles of the mean and the resolved RMS values of the radial velocity for the non-reacting flow. . . . .	72
41	Sydney/Sandia: Time averaged recirculation features in the non-reacting simulations. . . . .	73
42	Sydney/Sandia: Instantaneous and time averaged contours of the mixture fraction in the non-reacting simulations. . . . .	74
43	Sydney/Sandia: Radial profiles of the mean values of the mixture fraction for the non-reacting flow. . . . .	75
44	Sydney/Sandia: Radial profiles of the resolved RMS values of the mixture fraction for the non-reacting flow. . . . .	76
45	Sydney/Sandia: Time averaged recirculation features in the reacting flow. . .	77
46	Sydney/Sandia: Radial profiles of the mean values of the streamwise velocity for the reacting flow. . . . .	78
47	Sydney/Sandia: Radial profiles of the resolved RMS values of the streamwise velocity for the reacting flow. . . . .	79
48	Sydney/Sandia: Radial profiles of the mean values of the radial velocity for the reacting flow. . . . .	80
49	Sydney/Sandia: Radial profiles of the resolved RMS values of the radial velocity for the reacting flow. . . . .	81
50	Sydney/Sandia: Radial profiles of the mean values of the mixture fraction for the reacting flow. . . . .	82
51	Sydney/Sandia: Radial profiles of the RMS values of the mixture fraction for the reacting flow. . . . .	83
52	Sydney/Sandia: Radial profiles of the mean values of the temperature for the reacting flow. . . . .	84

53	Sydney/Sandia: Radial profiles of the RMS values of the temperature for the reacting flow. . . . .	85
54	Sydney/Sandia: PDF locations. . . . .	86
55	Sydney/Sandia: PDFs of the resolved mixture fraction. . . . .	87
56	Sydney/Sandia: PDFs of the resolved temperature . . . . .	88
57	Sydney/Sandia: PDFs of the resolved mixture fraction compared to experiment. . . . .	89
58	Sydney/Sandia: PDFs of the resolved temperature compared to experiment. . . . .	90
59	Sydney/Sandia: Radial profiles of the mean values of the oxygen mass fraction. . . . .	94
60	Sydney/Sandia: Radial profiles of the RMS values of the oxygen mass fraction. . . . .	95
61	Sydney/Sandia: Radial profiles of the mean values of the water mass fraction. . . . .	96
62	Sydney/Sandia: Radial profiles of the RMS values of the water mass fraction. . . . .	97
63	Sydney/Sandia: Radial profiles of the mean values of the carbon monoxide mass fraction. . . . .	98
64	Sydney/Sandia: Radial profiles of the RMS values of the carbon monoxide mass fraction. . . . .	99
65	Sydney/Sandia: Radial profiles of the mean values of the hydrogen mass fraction. . . . .	100
66	Sydney/Sandia: Radial profiles of the mean values of the carbon dioxide mass fraction. . . . .	101
67	Sydney/Sandia: Radial profiles of the mean values of the hydroxyl radical mass fraction. . . . .	102

## LIST OF SYMBOLS

### Roman:

- $C_I$  : SGS model parameter.
- $C_\Omega$  : SGS model parameter.
- $c_p$  : Mixture averaged specific heat at constant pressure.
- $C_R$  : SGS model parameter.
- $D$  : Fickian molecular diffusivity coefficient.
- $D_B$  : Bluff-body diameter.
- $D_J$  : Jet diameter.
- $D_t$  : SGS diffusivity coefficient.
- $F_\ell$  : Scalar filtered mass density function.
- $F_N$  : Discrete weighted scalar filtered mass density function.
- $\mathcal{G}$  : Filter kernel.
- $h$  : Total specific enthalpy.
- $J_i^\alpha$  :  $i^{th}$  component of the scalar flux of scalar  $\alpha$ .
- $k$  : Thermal conductivity.
- $Le$  : Lewis number.
- $m_i$  : Stochastic drift vector corresponding to the  $i^{th}$  stochastic diffusion process.
- $M_i^\alpha$  : SGS scalar fluxes.
- $N_E$  : Number of particles residing inside an ensemble domain.
- $N_p$  : Total number of Monte Carlo particles inside the computational domain.
- $N_s$  : Number of species.

- $p$  : Pressure.  
 $Pr$  : Prandtl number.  
 $r$  : Radial length,  $r = \sqrt{z^2 + y^2}$ .  
 $R_B$  : Bluff-body radius.  
 $Re$  : Reynolds number.  
 $\mathcal{R}$  : Universal gas constant.  
 $R$  : Gas constant for a mixture.  
 $S_\alpha$  : Chemical reaction source term for scalar  $\alpha$ .  
 $Sc$  : Schmidt number.  
 $\mathcal{S}_{ij}$  : Strain rate tensor.  
 $t$  : Time.  
 $T$  : Temperature.  
 $T_{ij}$  : SGS stresses.  
 $\mathbf{u}$  : Velocity vector.  
 $U_{BO}$  : 100% blow-off velocity.  
 $\mathcal{U}$  : Reference velocity vector used in MKEV SGS model.  
 $U_{CL}$  : Mean streamwise velocity at the centerline.  
 $U_{CO}$  : Coflow velocity.  
 $U_J$  : Bulk jet velocity.  
 $W_\alpha$  : Molecular weight of species  $\alpha$ .  
 $W_i$  : Wiener-Lévy process.  
 $\mathbf{x}$  : Position vector.  
 $\mathcal{X}$  : Vector of stochastic diffusion processes.  
 $x, y, z$  : Streamwise ( $x$ ), and two lateral ( $y, z$ ) directions.  
 $Y_\alpha$  : Mass fraction of species  $\alpha$ .  
 $Z$  : Mixture fraction.  
 $Z_s$  : Stoichiometric mixture fraction.
- Greek:**
- $\delta$  : Dirac delta function.  
 $\Delta$  : Finite difference grid size.

$\Delta_E$  : Characteristic length of an ensemble domain.  
 $\Delta_L$  : Filter width.  
 $\Delta m$  : Small unit of mass.  
 $\Delta x, \Delta y, \Delta z$  : Grid spacing in the corresponding directions.  
 $\mathcal{E}$  : SGS kinetic energy resolved with respect to some reference velocity.  
 $\zeta$  : Fine-grained density function.  
 $\mu$  : Dynamic viscosity.  
 $\nu_t$  : SGS eddy viscosity coefficient.  
 $\rho$  : fluid density.  
 $\sigma_\alpha^2$  : SGS variance of scalar  $\alpha$ .  
 $\Sigma_{ij}$  : Stochastic diffusion tensor.  
 $\tau_{ij}$  : Viscous stress tensor.  
 $\phi$  : Scalar variable vector.  
 $\psi$  : Sample space vector of the scalar array,  $\phi$ .  
 $\chi$  : Strain rate.  
 $\omega$  : Particle weight.  
 $\Omega_m$  : Frequency of mixing.

**Superscripts:**

$(n)$  :  $n^{th}$  particle.  
 $+$  : Lagrangian variable.

**Subscripts:**

$\alpha$  : Species index.  
 $B$  : Property of a bluff-body.  
 $i$  : Dimensional index.  
 $k$  :  $k^{th}$  time step in a numerical simulation.  
 $\ell$  : Filtered information related to filter width  $\Delta_L$ .  
 $L$  : Favré information related to filter width  $\Delta_L$ .  
 $ref$  : Reference state.  
 $t$  : Quantity related to the SGS.

**Symbols:**

$\langle Q(\mathbf{x}, t) \rangle_L$  : Favré filtered value of quantity  $Q$  with a filter of width  $\Delta_L$ .

$\langle Q(\mathbf{x}, t) \rangle_\ell$  : Filtered value of quantity  $Q$  with a filter of width  $\Delta_L$ .

$\overline{Q}$  : Time average (ensemble) of quantity  $Q$ .

$RMS(Q)$  : Temporal root mean square of quantity  $Q$ .

**Abbreviations:**

3D : Three-dimensional.

FD : Finite difference.

FDF : Filtered density function.

FMDF : Filtered mass density function.

IEM : Interaction by exchange with the mean.

LES : Large eddy simulation.

LMSE : Linear mean square estimation.

MC : Monte Carlo.

MKEV : Modified kinetic energy viscosity.

PDF : Probability density function.

RAS : Reynolds Averages Simulation.

SDE : Stochastic differential equation.

SFDF : Scalar filtered density function.

SFMDF : Scalar filtered mass density function.

SGS : Subgrid scale.

VFDF : Velocity Filtered Density Function.

VSFDF : Velocity Scalar Filtered Density Function.

VSFMDF : Velocity Scalar Filtered Mass Density Function.

*To my family and friends ...*

## ACKNOWLEDGMENTS

I would like to thank my Advisor, Professor Peyman Givi, for his multilateral support, patience and guidance through the course of my research. I also thank professor Stephen B. Pope of Cornell University for his collaborations and guidance on many aspects of this work. I am indebted to my colleagues and friends at the Computational Transport Phenomena Laboratory at the University of Pittsburgh, especially Mr. M. Reza H. Sheikhi and Mr. S. Levent Yilmaz, and more recently Mr. S. Mehdi Bostandoost Nik and Mr. Mahdi Mohebbi, for providing invaluable feedback and excellent atmosphere to conduct research. I am grateful to the members of my Thesis Defense Committee, Professors Giovanni P. Galdi, William J. Layton and Laura A. Schaefer.

The love and support provided by my parents, my wife Maria, and my friends remain an irreplaceable element in my completion of this work.

This work is part of a research sponsored by the U.S. Air Force Office of Scientific Research under Grant F49620-03-1-0022 (Program Manager: Dr. Julian M. Tishkoff), the National Science Foundation under Grant CTS-0426857, and the Office of the Secretary of Defense through Contract FA9101-04-C-0014 with Arnold Air Force Base. Computational resources are provided by the Pittsburgh Supercomputing Center (PSC), the National Center for Supercomputing Applications (NCSA) at the University of Illinois at Urbana-Champaign, and the School of Engineering Computational Support Team at the University of Pittsburgh.

## 1.0 INTRODUCTION

There has been significant progress in developments of subgrid scale (SGS) closures for large eddy simulation (LES) of turbulent reacting flows. Several recent reviews are available.<sup>13,16–23</sup> One such closure is via the filtered density function (FDF) methodology, first introduced by Givi<sup>24</sup> and Pope.<sup>25</sup> The FDF is the counterpart of the probability density function (PDF) method which has proven quite effective in Reynolds averaged simulations (RAS).<sup>13,26</sup> The approach has proven particularly useful for prediction of reacting flows.<sup>12,13,21,24,25,27–41</sup> The fundamental property of the PDF is the closed form nature of the chemical source term appearing in the transport equation governing the FDF. This property is very important as evidenced in several applications of FDF for LES of a variety of turbulent reacting flows.<sup>12,30–32,34,37,42</sup> The developments in FDF can be summarized as follows; Colucci *et al.*<sup>30</sup> developed a transport equation for the scalar FDF (SFDF) in constant density turbulent reacting flows, Jaber *et al.*<sup>12</sup> extended the methodology for LES of variable density flows by consideration of the “scalar filtered mass density function” (SFMDf) which is essentially the mass weighted SFDF. Gicquel *et al.*<sup>33</sup> developed the velocity FDF (VFDF) method in which the effects of velocity SGS convection appear in closed form. Drozda<sup>43</sup> and Sheikhi *et al.*<sup>44</sup> developed the velocity-scalar FDF (VSFDF) method in which the effects of velocity, scalar, and velocity-scalar SGS convection appear in closed form. Work is in progress on extending the VSFDF method to variable density flows by developing the velocity-scalar filtered mass density function (VSFMDf).<sup>45</sup>

A review of the current state of progress in FDF is available.<sup>23</sup> The encouraging results attained thus far warrant further improvements and implementations of this methodology for a wider class of reacting flows. The specific objective of this work is to implement the SFMDf for LES of hydrocarbon diffusion flames.

LES/SFMDF is conducted of two experimental flame configurations. The first is the flame studied in the experiments of the Combustion Research Facility at the Sandia National Laboratories (SNL) and the Technische Universität Darmstadt (TUD), namely Flame D.<sup>1-3</sup> This is a turbulent piloted non-premixed methane jet flame. The second flame is also studied by the Combustion Research Facility at the Sandia National Laboratories and at the Thermal Research Group at the University of Sydney.<sup>4-11</sup> This is a turbulent bluff-body stabilized hydrogen-methane jet flame. These flame are labeled as the Sandia/TUD and the Sydney/Sandia, respectively.

Piloted jet flames have been the subject of broad investigations by other computational and modeling methodologies.<sup>42,46-49</sup> In the experiments, three turbulent flames are considered: Flames D, E and F. The geometrical configuration in these flames is the same, but the jet inlet velocity is varied. In Flame D, the fuel jet velocity is the lowest and the flame is close to equilibrium. The jet velocity increases from flames D to E to F, with noticeable non-equilibrium effects in the latter two. Only Flame D is considered in this work. The objective is to assess the predictive capability of the LES/SFMDF in capturing the essential flow field characteristics.

The bluff-body stabilized flames have also been studied by several investigators.<sup>9,50-58</sup> These flames produce complex flow patterns characteristic of practical combustors, and are therefore important for industrial applications. In the experiments, a variety of operating conditions are considered. The most complete set of measurements, however, has been compiled for the hydrogen-methane flames. These flames are considered at 50%, 75% and 91% blow-off (extinction). Here, only the 50% blow-off case is considered. The objective is to further assess the predictive capability of the LES/SFMDF. This is an important step before considering of the flames with strong extinction and reignition phenomena.

Both flames are simulated via the near-equilibrium chemistry model. This model is constructed by considering the one-dimensional counterflow (opposed-jet) laminar flame<sup>14,15,59–62</sup> in which the chemical reaction is modeled via detailed chemical kinetics.<sup>63,64</sup> It is useful to note that the approach here is fundamentally different from those followed in previous flamelet based SGS models. In most previous contributions,<sup>48,54,65–68</sup> the FDF of the mixture fraction is *assumed* (*e.g.* beta or other distribution). Here, a modeled transport equation for the FDF is considered. This represents a much more systematic approach.

## 2.0 FORMULATION

This chapter provides the descriptions of the governing equations, mathematical formulation of the FDF, the proposed modeling of the FDF transport, the chemical reaction model, and the numerical solution procedure for LES/SFMDF.

### 2.1 GOVERNING EQUATIONS

Implementation of LES involves the use of the spatial filtering operation<sup>13,69</sup>

$$\langle Q(\mathbf{x}, t) \rangle_\ell = \int_{-\infty}^{+\infty} Q(\mathbf{x}', t) \mathcal{G}(\mathbf{x}', \mathbf{x}) d\mathbf{x}' \quad (2.1)$$

where  $\mathcal{G}$  denotes the filter kernel of width  $\Delta_L$ , and  $\langle Q(\mathbf{x}, t) \rangle_\ell$  represents the filtered value of the transport variable  $Q(\mathbf{x}, t)$ . In variable density flows it is convenient to consider the Favré filtered quantity,  $\langle Q(\mathbf{x}, t) \rangle_L = \langle \rho Q \rangle_\ell / \langle \rho \rangle_\ell$ . We consider spatially invariant and localized filter functions,  $\mathcal{G}(\mathbf{x}', \mathbf{x}) \equiv \mathcal{G}(\mathbf{x}' - \mathbf{x})$  with the properties<sup>70</sup>  $\mathcal{G}(\mathbf{x}) = \mathcal{G}(-\mathbf{x})$ , and  $\int_{-\infty}^{\infty} \mathcal{G}(\mathbf{x}) d\mathbf{x} = 1$ . Moreover, we only consider “positive” filter functions<sup>71</sup> for which all the moments  $\int_{-\infty}^{\infty} x^m \mathcal{G}(x) dx$  exist for  $m \geq 0$ .

The flow field to be simulated is unsteady, three-dimensional (3D), and involves gaseous (single-phase) hydrocarbon combustion. Newton’s law of viscosity, Fourier’s law of heat conduction and Fick’s law of mass diffusion are employed. The caveats in the use of these laws in reacting flows are recognized.<sup>72,73</sup> The primary transport variables are the fluid density  $\rho$ , the velocity vector  $u_i$ ,  $i = 1, 2, 3$  along the  $x_i$  direction and at a time  $t$ , the pressure  $p$ , the mass fractions of  $N_s$  species,  $Y_\alpha$  ( $\alpha = 1, 2, \dots, N_s$ ), and the total specific enthalpy  $h$ .

The transport variables satisfy the conservation equations of mass, momentum, species' mass fractions, and enthalpy (energy).<sup>72,73</sup> The filtered form of these equations is:

$$\frac{\partial \langle \rho \rangle_\ell}{\partial t} + \frac{\partial \langle \rho \rangle_\ell \langle u_i \rangle_L}{\partial x_i} = 0 \quad (2.2)$$

$$\frac{\partial \langle \rho \rangle_\ell \langle u_j \rangle_L}{\partial t} + \frac{\partial \langle \rho \rangle_\ell \langle u_i \rangle_L \langle u_j \rangle_L}{\partial x_i} = -\frac{\partial \langle p \rangle_\ell}{\partial x_j} + \frac{\partial \langle \tau_{ij} \rangle_\ell}{\partial x_i} - \frac{\partial T_{ij}}{\partial x_i} \quad (2.3)$$

$$\frac{\partial \langle \rho \rangle_\ell \langle \phi_\alpha \rangle_L}{\partial t} + \frac{\partial \langle \rho \rangle_\ell \langle u_i \rangle_L \langle \phi_\alpha \rangle_L}{\partial x_i} = -\frac{\partial \langle J_i^\alpha \rangle_\ell}{\partial x_i} - \frac{\partial M_i^\alpha}{\partial x_i} + \langle \rho S_\alpha \rangle_\ell \quad (2.4)$$

where the scalar fields are denoted by  $\phi_\alpha \equiv Y_\alpha$ ,  $\alpha = 1, \dots, N_s$ ,  $\phi_\sigma \equiv h = \sum_{\alpha=1}^{N_s} h_\alpha Y_\alpha$ , and  $S_\alpha$  is the production rate of species  $\alpha$ . Equations (2.2,2.3,2.4) are closed by the constitutive relations,<sup>74</sup>

$$\langle p \rangle_\ell \approx \langle \rho \rangle_\ell \mathcal{R} \langle T \rangle_L \sum_{\alpha=1}^{N_s} \frac{\langle Y_\alpha \rangle_L}{W_\alpha} \quad (2.5)$$

where  $\mathcal{R}$  is the Universal Gas Constant,  $W_\alpha$  is the molecular weight of species  $\alpha$  and  $T$  is the temperature.  $\tau_{ij}$  and  $J_i^\alpha$  denote the viscous stress tensor and the scalar fluxes, respectively.

$$\langle \tau_{ij} \rangle_\ell \approx \langle \mu \rangle_\ell \left( \frac{\partial \langle u_i \rangle_L}{\partial x_j} + \frac{\partial \langle u_j \rangle_L}{\partial x_i} - \frac{2}{3} \frac{\partial \langle u_k \rangle_L}{\partial x_k} \delta_{ij} \right) \quad (2.6)$$

$$\langle J_i^\alpha \rangle_\ell \approx -\langle \rho \rangle_\ell \langle D \rangle_L \frac{\partial \langle \phi_\alpha \rangle_L}{\partial x_i} \quad (2.7)$$

$$\langle \mu \rangle_\ell = Pr \left\langle \frac{k}{c_p} \right\rangle_\ell, \quad \langle D \rangle_L = \frac{1}{\langle \rho \rangle_\ell Le} \left\langle \frac{k}{c_p} \right\rangle_\ell, \quad \left\langle \frac{k}{c_p} \right\rangle_\ell = \mu_{ref} \left( \frac{\langle T \rangle_L}{T_{ref}} \right)^{0.7} \quad (2.8)$$

where  $\mu$  is the molecular coefficient of viscosity,  $Pr$  is the Prandtl number,  $D$  is the molecular diffusion coefficient,  $Le$  is the Lewis number, and a power law relationship is used for the ratio of  $k$ , thermal conductivity, and  $c_p$ , the mixture averaged specific heat at constant pressure. Subscript *ref* denotes a reference state.

The SGS closure problem is associated with  $T_{ij} = \langle \rho \rangle_\ell (\langle u_i u_j \rangle_L - \langle u_i \rangle_L \langle u_j \rangle_L)$  and  $M_i^\alpha = \langle \rho \rangle_\ell (\langle u_i \phi_\alpha \rangle_L - \langle u_i \rangle_L \langle \phi_\alpha \rangle_L)$ , respectively denoting the SGS stresses and SGS fluxes. In reacting flows, an additional model is required for the filtered reaction rates of the mass

fractions, *i.e.*  $\langle \rho S_\alpha \rangle_\ell$ ,  $\alpha = 1, \dots, N_s$  (at low Mach numbers,  $\langle \rho S_\sigma \rangle_\ell \approx 0$ ). It is the modeling of the latter that SFMDF is the subject of.

The hydrodynamic SGS closure is based on models well established in non-reacting flows.<sup>75,76</sup> The first SGS model considered is the Smagorinsky-Yoshizawa<sup>77,78</sup> closure.

$$T_{ij} = -2 \langle \rho \rangle_\ell C_S^2 \Delta_L^2 |\langle \mathcal{S} \rangle_L| \left( \langle \mathcal{S}_{ij} \rangle_L - \frac{1}{3} \langle \mathcal{S}_{kk} \rangle_L \delta_{ij} \right) + \frac{2}{3} \langle \rho \rangle_\ell C_I \Delta_L^2 |\langle \mathcal{S} \rangle_L|^2 \delta_{ij} \quad (2.9)$$

where the  $\langle \mathcal{S}_{ij} \rangle_L$  is the strain rate tensor

$$\langle \mathcal{S}_{ij} \rangle_L = \frac{1}{2} \left( \frac{\partial \langle u_i \rangle_L}{\partial x_j} + \frac{\partial \langle u_j \rangle_L}{\partial x_i} \right) \quad (2.10)$$

and

$$|\langle \mathcal{S} \rangle_L| = \sqrt{2 \langle \mathcal{S}_{ij} \rangle_L \langle \mathcal{S}_{ij} \rangle_L} \quad (2.11)$$

The values of the model constants  $C_S$  and  $C_I$  vary with applications. Pope<sup>13</sup> suggests a value for  $C_S$  in the range of 0.1 to 0.24. Moin *et al.*<sup>79</sup> suggest that  $C_I \approx 0.0175$ .

The second SGS model is the modified kinetic energy viscosity (MKEV) closure. It was introduced by Jaber *et al.*<sup>12</sup> and is essentially a modified version of the model proposed by Bardina *et al.*<sup>80</sup>. The SGS stresses are modeled by,

$$T_{ij} = -2 C_R \langle \rho \rangle_\ell \Delta_L \mathcal{E}^{\frac{1}{2}} \left( \langle \mathcal{S}_{ij} \rangle_L - \frac{1}{3} \langle \mathcal{S}_{kk} \rangle_L \delta_{ij} \right) + \frac{2}{3} C_I \langle \rho \rangle_\ell \mathcal{E} \delta_{ij} \quad (2.12)$$

where  $\mathcal{E} = |\langle u_i^* \rangle_L \langle u_i^* \rangle_L - \langle \langle u_i^* \rangle_L \rangle_g \langle \langle u_i^* \rangle_L \rangle_g|$ ,  $u_i^* = u_i - \mathcal{U}_i$ , and  $\mathcal{U}_i$  is a reference velocity in the  $x_i$  direction. In this work, the  $\mathcal{U}_i$  is set to zero in the cross-stream and spanwise directions, and to the average of the high- and low-speed streams in the streamwise direction at the inlet. The subscript  $g$  denotes a secondary filter level with characteristic filter width  $\Delta_G > \Delta_L$ . Further improvements to the SGS closure can be made by implementing a VSFDF methodology. The LES/VSFDF is essentially equivalent to a second order moment closure<sup>43,44</sup> in LES.

The subgrid eddy viscosity is expressed as  $\nu_t = C_S^2 \Delta_L^2 |\langle \mathcal{S} \rangle_L|$  and  $\nu_t = C_R \Delta_L \mathcal{E}^{\frac{1}{2}}$  for the Smagorinsky and the MKEV SGS models, respectively. The SGS scalar fluxes are modeled by a similar closure<sup>81</sup>

$$M_i^\alpha = - \langle \rho \rangle_\ell D_t \frac{\partial \langle \phi_\alpha \rangle_L}{\partial x_i} \quad (2.13)$$

where  $D_t = \frac{\nu_t}{Sc_t}$  is the subgrid diffusivity.  $Sc_t$  is the subgrid Schmidt number, and has the same value for all of the scalar variables.

## 2.2 SCALAR FILTERED MASS DENSITY FUNCTION

The “scalar filtered mass density function” (SF MDF), denoted by  $F_\ell$ , is formally defined as

$$F_\ell(\boldsymbol{\phi}; \mathbf{x}, t) \equiv \int_{-\infty}^{+\infty} \rho(\mathbf{x}', t) \zeta(\boldsymbol{\psi}, \boldsymbol{\phi}(\mathbf{x}', t)) \mathcal{G}(\mathbf{x}' - \mathbf{x}) d\mathbf{x}' \quad (2.14)$$

$$\zeta(\boldsymbol{\psi}, \boldsymbol{\phi}(\mathbf{x}, t)) \equiv \delta(\boldsymbol{\psi} - \boldsymbol{\phi}(\mathbf{x}, t)) \equiv \prod_{\alpha=1}^{N_s} \delta(\psi_\alpha - \phi_\alpha(\mathbf{x}, t)) \quad (2.15)$$

where  $\delta$  denotes the delta function and  $\boldsymbol{\psi}$  denotes the sample space of the scalar array. The term  $\zeta$  is the “fine-grained” density,<sup>26,82</sup> hence Eq. (2.14) defines the SF MDF as the *mass weighted spatially filtered* value of the fine-grained density function. With the filter properties specified in Sec. 2.1,  $F_\ell$  has all of the properties of a PDF.<sup>26</sup>

To further facilitate the mathematical development of the SF MDF, we define the mass weighted conditional filtered mean of a variable  $Q(\mathbf{x}, t)$  as

$$\langle Q(\mathbf{x}, t) | \boldsymbol{\phi}(\mathbf{x}, t) = \boldsymbol{\psi} \rangle_\ell \equiv \langle Q(\mathbf{x}, t) | \boldsymbol{\psi} \rangle_\ell \quad (2.16)$$

$$\langle Q(\mathbf{x}, t) | \boldsymbol{\psi} \rangle_\ell = \frac{\int_{-\infty}^{+\infty} Q(\mathbf{x}', t) \rho(\mathbf{x}', t) \zeta(\boldsymbol{\psi}; \boldsymbol{\phi}(\mathbf{x}', t)) \mathcal{G}(\mathbf{x}' - \mathbf{x}) d\mathbf{x}'}{F_\ell(\boldsymbol{\psi}; \mathbf{x}, t)} \quad (2.17)$$

Equation (2.17) implies the following properties of the SF MDF

$$(i) \quad \text{For } Q(\mathbf{x}, t) = c, \quad \langle Q(\mathbf{x}, t) | \boldsymbol{\psi} \rangle_\ell = c \quad (2.18a)$$

$$(ii) \quad \text{For } Q(\mathbf{x}, t) \equiv \hat{Q}(\boldsymbol{\phi}(\mathbf{x}, t)) \quad \langle Q(\mathbf{x}, t) | \boldsymbol{\psi} \rangle_\ell = \hat{Q}(\boldsymbol{\psi}) \quad (2.18b)$$

$$(iii) \quad \text{Integral property:} \quad \int_{-\infty}^{+\infty} \langle Q(\mathbf{x}, t) | \boldsymbol{\psi} \rangle_\ell F_\ell(\boldsymbol{\psi}; \mathbf{x}, t) d\boldsymbol{\psi} = \langle \rho(\mathbf{x}, t) \rangle_\ell \langle Q(\mathbf{x}, t) \rangle_L \quad (2.18c)$$

where  $c$  is a constant and  $Q(\mathbf{x}, t) \equiv \hat{Q}(\boldsymbol{\phi}(\mathbf{x}, t))$  denotes the case where the variable  $Q$  is fully described by the scalar vector variable,  $\boldsymbol{\phi}(\mathbf{x}, t)$ . From Eqs. (2.18) it follows that the filtered value of any function of scalar variable is obtained by integration over the scalar sample space.

$$\langle \rho(\mathbf{x}, t) \rangle_\ell \langle Q(\mathbf{x}, t) \rangle_L = \int_{-\infty}^{+\infty} \hat{Q}(\boldsymbol{\psi}) F_\ell(\boldsymbol{\psi}; \mathbf{x}, t) d\boldsymbol{\psi} \quad (2.19)$$

The transport equation for the SFMDF is developed by considering a time derivative of the fine-grained density function<sup>82,83</sup>

$$\frac{\partial \zeta(\boldsymbol{\psi}; \boldsymbol{\phi})}{\partial t} = \frac{\partial \phi_\alpha(\mathbf{x}, t)}{\partial t} \frac{\partial \zeta(\boldsymbol{\psi}; \boldsymbol{\phi})}{\partial \phi_\alpha} = - \frac{\partial \phi_\alpha(\mathbf{x}, t)}{\partial t} \frac{\partial \zeta(\boldsymbol{\psi}; \boldsymbol{\phi})}{\partial \psi_\alpha} \quad (2.20)$$

Substituting the scalar conservation transport equation for the first derivative on the RHS of Eq. (2.20) we obtain the transport equation for the fine-grained density function

$$\frac{\partial \hat{\rho}(\boldsymbol{\phi}) \zeta(\boldsymbol{\psi}; \boldsymbol{\phi})}{\partial t} + \frac{\partial \hat{\rho}(\boldsymbol{\phi}) u_i(\mathbf{x}, t) \zeta(\boldsymbol{\psi}; \boldsymbol{\phi})}{\partial x_i} = - \left( - \frac{\partial J_i^\alpha}{\partial x_i} + \hat{\rho}(\boldsymbol{\phi}) \hat{S}_\alpha(\boldsymbol{\phi}) \right) \frac{\partial \zeta(\boldsymbol{\psi}; \boldsymbol{\phi})}{\partial \psi_\alpha} \quad (2.21)$$

An alternative form of Eq. (2.21) can be found by rewriting the scalar flux term

$$\begin{aligned} \frac{\partial \hat{\rho}(\boldsymbol{\phi}) \zeta(\boldsymbol{\psi}; \boldsymbol{\phi})}{\partial t} + \frac{\partial \hat{\rho}(\boldsymbol{\phi}) u_i(\mathbf{x}, t) \zeta(\boldsymbol{\psi}; \boldsymbol{\phi})}{\partial x_i} &= - \frac{\partial}{\partial x_i} \left( \hat{\rho}(\boldsymbol{\phi}) D \frac{\partial \zeta(\boldsymbol{\psi}; \boldsymbol{\phi})}{\partial x_i} \right) \\ &+ \hat{\rho}(\boldsymbol{\phi}) D \frac{\partial \phi_\alpha}{\partial x_i} \frac{\partial \phi_\beta}{\partial x_i} \frac{\partial^2 \zeta(\boldsymbol{\psi}; \boldsymbol{\phi})}{\partial \psi_\alpha \partial \psi_\beta} - \hat{\rho}(\boldsymbol{\phi}) \hat{S}_\alpha(\boldsymbol{\phi}) \frac{\partial \zeta(\boldsymbol{\psi}; \boldsymbol{\phi})}{\partial \psi_\alpha} \end{aligned} \quad (2.22)$$

The transport equation for  $F_\ell(\boldsymbol{\psi}; \mathbf{x}, t)$  is obtained by filtering Eq. (2.21) (or Eq. (2.22)) according to Eq. (2.14). The result, after some algebraic manipulation, is

$$\frac{\partial F_\ell(\boldsymbol{\psi}; \mathbf{x}, t)}{\partial t} + \frac{\partial \langle u_i(\mathbf{x}, t) | \boldsymbol{\psi} \rangle_\ell F_\ell(\boldsymbol{\psi}; \mathbf{x}, t)}{\partial x_i} = \frac{\partial}{\partial \psi_\alpha} \left[ \left\langle \frac{\partial J_i^\alpha}{\partial x_i} - \hat{\rho}(\boldsymbol{\phi}) \hat{S}_\alpha(\boldsymbol{\phi}) \mid \boldsymbol{\psi} \right\rangle_\ell \frac{F_\ell(\boldsymbol{\psi}; \mathbf{x}, t)}{\hat{\rho}(\boldsymbol{\psi})} \right] \quad (2.23)$$

The same procedure, when applied to Eq. (2.22), yields

$$\begin{aligned} \frac{\partial F_\ell(\boldsymbol{\psi}; \mathbf{x}, t)}{\partial t} + \frac{\partial \langle u_i(\mathbf{x}, t) | \boldsymbol{\psi} \rangle_\ell F_\ell(\boldsymbol{\psi}; \mathbf{x}, t)}{\partial x_i} &= \frac{\partial}{\partial x_i} \left[ \langle \rho \rangle_\ell \langle D \rangle_L \frac{\partial}{\partial x_i} \left( \frac{F_\ell(\boldsymbol{\psi}; \mathbf{x}, t)}{\langle \rho \rangle_\ell} \right) \right] \\ &- \frac{\partial^2}{\partial \psi_\alpha \partial \psi_\beta} \left( \left\langle \hat{\rho}(\boldsymbol{\phi}) D \frac{\partial \phi_\alpha}{\partial x_i} \frac{\partial \phi_\beta}{\partial x_i} \mid \boldsymbol{\psi} \right\rangle_\ell \frac{F_\ell(\boldsymbol{\psi}; \mathbf{x}, t)}{\hat{\rho}(\boldsymbol{\psi})} \right) - \frac{\partial}{\partial \psi_\alpha} \left( \hat{S}_\alpha(\boldsymbol{\psi}) F_\ell(\boldsymbol{\psi}; \mathbf{x}, t) \right) \end{aligned} \quad (2.24)$$

where the following approximation is made

$$\frac{\partial}{\partial x_i} \left\langle \hat{\rho}(\boldsymbol{\phi}) D \frac{\partial \zeta(\boldsymbol{\psi}; \boldsymbol{\phi})}{\partial x_i} \right\rangle_\ell \approx - \frac{\partial}{\partial x_i} \left[ \langle \rho \rangle_\ell \langle D \rangle_L \frac{\partial}{\partial x_i} \left( \frac{F_\ell(\boldsymbol{\psi}; \mathbf{x}, t)}{\langle \rho \rangle_\ell} \right) \right] \quad (2.25)$$

The transport equations for SFMDF (Eq. (2.24)) contain conditionally filtered terms that are unclosed. The second term on the left hand side represents the effect of the large-scale and SGS convection. This is modeled by the conventional gradient diffusion

$$(\langle u_i | \boldsymbol{\psi} \rangle_\ell - \langle u_i \rangle_L) F_\ell = - \langle \rho \rangle_\ell D_t \frac{\partial}{\partial x_i} \left( \frac{F_\ell}{\langle \rho \rangle_\ell} \right) \quad (2.26)$$

The second term on the right hand side of Eq. (2.24) is related to SGS mixing. The closure adapted for the SGS mixing is based on the linear mean square estimation (LMSE) model,<sup>82,84</sup> also known as the interaction by exchange with the mean (IEM) model,<sup>85</sup>

$$-\frac{\partial^2}{\partial\psi_\alpha\partial\psi_\beta}\left(\left\langle\hat{\rho}D\frac{\partial\phi_\alpha}{\partial x_i}\frac{\partial\phi_\beta}{\partial x_i}\middle|\boldsymbol{\psi}\right\rangle_\ell\frac{F_\ell}{\hat{\rho}}\right)=\frac{\partial}{\partial\psi_\alpha}(\Omega_m(\psi_\alpha-\langle\phi_\alpha\rangle_L)F_\ell)\quad(2.27)$$

where  $\Omega_m$  is the frequency of mixing within the subgrid. This is modeled by

$$\Omega_m(\mathbf{x},t)=C_\Omega\frac{\langle D\rangle_L+D_t}{\Delta_L^2}\quad(2.28)$$

The last term on the right hand side of Eq. (2.24) is due to the chemical reaction and appears in closed form.

Combining Eqs. (2.26), (2.25) and (2.27) with Eq. (2.24) provides the modeled SFMDF transport equation

$$\begin{aligned}\frac{\partial F_\ell(\boldsymbol{\psi};\mathbf{x},t)}{\partial t}+\frac{\partial\langle u_i(\mathbf{x},t)\rangle_\ell F_\ell(\boldsymbol{\psi};\mathbf{x},t)}{\partial x_i}&=\frac{\partial}{\partial x_i}\left[\langle\rho\rangle_\ell(\langle D\rangle_L+D_t)\frac{\partial}{\partial x_i}\left(\frac{F_\ell(\boldsymbol{\psi};\mathbf{x},t)}{\langle\rho\rangle_\ell}\right)\right] \\ &+\frac{\partial}{\partial\psi_\alpha}(\Omega_m(\psi_\alpha-\langle\phi_\alpha\rangle_L)F_\ell(\boldsymbol{\psi};\mathbf{x},t))-\frac{\partial}{\partial\psi_\alpha}\left(\hat{S}_\alpha(\boldsymbol{\psi})F_\ell(\boldsymbol{\psi};\mathbf{x},t)\right)\end{aligned}\quad(2.29)$$

This equation may be integrated to obtain transport equations for the moments. The equations for the first Favré filtered moment,  $\langle\phi_\alpha\rangle_L$ , and the generalized variance,  $\sigma_\alpha^2=\langle\phi_\alpha^2\rangle_L-\langle\phi_\alpha\rangle_L^2$  are

$$\frac{\partial\langle\rho\rangle_\ell\langle\phi_\alpha\rangle_L}{\partial t}+\frac{\partial\langle\rho\rangle_\ell\langle u_i\rangle_L\langle\phi_\alpha\rangle_L}{\partial x_i}=\frac{\partial}{\partial x_i}\left(\langle\rho\rangle_\ell(\langle D\rangle_L+D_t)\frac{\partial\langle\phi_\alpha\rangle_L}{\partial x_i}\right)+\langle\rho\rangle_\ell\langle S_\alpha\rangle_L\quad(2.30)$$

$$\begin{aligned}\frac{\partial\langle\rho\rangle_\ell\sigma_\alpha^2}{\partial t}+\frac{\partial\langle\rho\rangle_\ell\langle u_i\rangle_L\sigma_\alpha^2}{\partial x_i}&=\frac{\partial}{\partial x_i}\left(\langle\rho\rangle_\ell(\langle D\rangle_L+D_t)\frac{\partial\sigma_\alpha^2}{\partial x_i}\right) \\ &+2\langle\rho\rangle_\ell(\langle D\rangle_L+D_t)\frac{\partial\langle\phi_\alpha\rangle_L}{\partial x_i}\frac{\partial\langle\phi_\alpha\rangle_L}{\partial x_i}-2\Omega_m\langle\rho\rangle_\ell\sigma_\alpha^2 \\ &+2\langle\rho\rangle_\ell(\langle\phi_\alpha S_\alpha\rangle_L-\langle\phi_\alpha\rangle_L\langle S_\alpha\rangle_L)\end{aligned}\quad(2.31)$$

### 2.3 STOCHASTIC SYSTEM

The most convenient means of modeling and solving the FDF transport equation is via the “Lagrangian Monte Carlo” procedure.<sup>26,86</sup> The basis of this procedure is the same as that in recent RAS<sup>87–89</sup> and LES/FDF.<sup>12,30,32,33</sup> Therefore, here only some of the fundamental properties of the methodology will be described. With the Lagrangian procedure, the FDF is represented by an ensemble of computational “stochastic elements” (or “particles”) which are transported in the “physical space” by the combined actions of large scale convection and diffusion (molecular and subgrid). In addition, transport in the “composition space” occurs due to chemical reaction and SGS mixing. These physical processes are described by the set of stochastic differential equations (SDEs).<sup>90–92</sup> The diffusion process<sup>92</sup> is considered for this purpose,

$$d\mathcal{X}_i(t) = m_i(\mathcal{X}(t), t)dt + \Sigma_{ij}(\mathcal{X}(t), t)dW_j \quad (2.32)$$

where  $\mathcal{X}_i$  is a vector of  $i = 1, \dots, n$  diffusion processes,  $m_i$  is the drift vector,  $\Sigma_{ij}$  is the diffusion tensor, and  $W_j$  ( $j = 1, \dots, m$ ) denotes the Wiener-Lévy processes.

The SDEs used in this work are

$$dx_i^+ = \left[ \langle u_i \rangle_L + \frac{1}{\langle \rho \rangle_\ell} \frac{\partial \langle \rho \rangle_\ell (\langle D \rangle_L + D_t)}{\partial x_i} \right] dt + \sqrt{2(\langle D \rangle_L + D_t)} dW_i \quad (2.33)$$

$$d\phi_\alpha^+ = [-\Omega_m [\phi_\alpha^+ - \langle \phi_\alpha \rangle_L] + S_\alpha(\phi^+)] dt \quad (2.34)$$

where the  $x^+$  and  $\phi^+$  denote Lagrangian position and composition (mixture fraction), respectively. The Fokker-Planck equation corresponding to Eqs. (2.33) and (2.34) is equivalent to Eq. (2.29).<sup>26</sup> Thus, the solution of these SDEs represents the SFMDF in the probabilistic sense.

## 2.4 CHEMICAL REACTION MODEL

Both flames are simulated via a near-equilibrium chemistry model. This model is constructed by considering the one-dimensional counterflow (opposed jet) laminar flame<sup>14,15,59–62</sup> in which the chemical reaction is modeled via detailed chemical kinetics.<sup>63,64</sup> At low strain rates,  $\chi$ , all of the thermo-chemical variables are related to the “mixture fraction.” The “flamelet” table constructed in this way can be used in conjunction with LES/SFMDF predictions of the mixture fraction. For flames under non-equilibrium, *e.g.* when flame extinction and reignition are expected, it is required to employ more realistic finite-rate kinetics models. Reasonable candidates for such models are the 25-step skeletal mechanism of Smooke *et al.*,<sup>74</sup> 12-step mechanism of Sung *et al.*,<sup>93</sup> 4-step mechanism of Seshadri *et al.*,<sup>94</sup> or the 2-step mechanism of Williams.<sup>95</sup> Work is currently in progress<sup>96</sup> on using several of the reduced mechanisms via the In Situ Adaptive Tabulation methodology developed by Pope.<sup>97</sup>

For a constant strain rate, the SGS statistics of the thermo-chemical variables are directly related to the mixture fraction,  $Z(\mathbf{x}, t)$

$$Q(\mathbf{x}, t) = Q(Z(\mathbf{x}, t)) \quad (2.35)$$

Therefore,

$$\langle \rho(\mathbf{x}, t) \rangle_\ell \langle Q(\mathbf{x}, t) \rangle_L = \int_{-\infty}^{+\infty} Q(Z(\mathbf{x}, t)) F_\ell(\psi_Z; \mathbf{x}, t) d\psi \quad (2.36)$$

## 2.5 NUMERICAL PROCEDURE

The SFMDF is solved via a hybrid Eulerian-Lagrangian finite difference (FD)/ Monte Carlo (MC) procedure.<sup>12,30,44</sup> For numerical solution of the hydrodynamic field in LES/SFMDF, we use a high-order accurate FD procedure. This discretization procedure is based on the “compact parameter” scheme<sup>98</sup> which yields fourth order spatial accuracy. A second order accurate symmetric predictor-corrector sequence is employed for time integration of Eqs. ((2.2)-(2.4)). In addition to the Favré filtered quantities, Eqs. ((2.2)-(2.4)) also provide information needed to compute the SGS eddy viscosity and SGS eddy diffusivity coefficients.

The filtered pressure,  $\langle p \rangle_\ell$ , is obtained from the filtered equation of state,  $\langle p \rangle_\ell = \langle \rho \rangle_\ell \langle RT \rangle_L$  where  $R$  is the gas constant for a mixture and  $\langle RT \rangle_L$  is obtained from the energy equation. The coupling between the finite difference and Monte Carlo procedures is enacted by the heat release source term in the energy equation.

Simulations are conducted on a fixed and equally spaced, by a length  $\Delta$ , grid points. Standard characteristic boundary conditions<sup>21,99</sup> are implemented for the continuity, momentum and energy transport equations. A zero derivative boundary conditions are imposed for the scalar values at the outlet and lateral boundaries.

The MC solver provides the Favré filtered scalar field by considering a set of  $N_p$  particles that evolve according to the diffusion process described by Eqs. (2.33) and (2.34). Each particle carries the information pertaining to its position  $x_i^{(n)}$  and scalar value,  $\phi_\alpha^{(n)}$  for  $n = 1 \dots N_p$ . The scalar values change due to the SGS mixing and the chemical reaction. This process is numerically split into two parts. First, scalar values of each particle are updated via a SGS mixing model. Second, the reaction rates,  $S_\alpha^{(n)}$ , are computed based on updated scalar values and the scalar values. Finally, the SDEs are temporally integrated. The simplest way of performing this integration is via the Euler-Maruyama approximation<sup>100-102</sup>

$$\mathcal{X}_i^{(n)}(t_{k+1}) = \mathcal{X}_i^{(n)}(t_k) + m_i^{(n)}(\mathcal{X}(\mathbf{t}_k), t_k) \Delta t + \Sigma_{ij}^{(n)}(\mathcal{X}(t_k), t_k) \Delta t^{\frac{1}{2}} \xi_j^{(n)}(t_k) \quad (2.37)$$

where  $\xi^{(n)}(t_k)$  is an independent standardized Gaussian random variable. Higher order numerical schemes are also available for stochastic differential equations,<sup>100,102</sup> but caution is advised when selecting one. Since the diffusion terms  $\Sigma_{ij}^{(n)}$  depend on the state variable,  $\mathcal{X}^{(n)}$ , the numerical scheme may alter the solution in a way inconsistent with the true nature of the undiscretized set of SDEs.<sup>103</sup> The numerical scheme must be consistent with Itô-Gikhman calculus.<sup>104,105</sup> Equation (2.37) exhibits this property.

To understand the operational procedures of the hybrid configuration, the elements of the computation are shown, for a two-dimensional case, in Fig. 1. This figure shows the MC particles randomly distributed and freely moving within the domain. This transport is Lagrangian, thus the solution is free of constraints associated with typical convection on fixed grid points. Statistical information is obtained by considering an ensemble of  $N_E$  particles residing within an ensemble domain of characteristic length  $\Delta_E$  and centered around a FD

grid point. The ensemble approach is necessary as the probability of finding a single, or multiple for that matter, particle(s) at a given finite-difference grid point is zero.<sup>106</sup> The process of ensemble averaging of a MC variable is further illustrated in Fig. 2. This figure shows the FD and MC representations of the mixture fraction. By averaging the values carried by the particles residing within an ensemble domain, we obtain the Favré filtered values of the mixture fraction. The size of the ensemble domain cannot be established a priori.<sup>26</sup> The ideal condition for accurate statistics requires  $\Delta_E \rightarrow 0$  and  $N_E \rightarrow \infty$ . For a fixed number of particles in the computational domain, large ensemble domain size decreases statistical error, but increases the spatial resolution error. The latter causes excessive diffusion. For a fixed ensemble domain size, small number of particles diminishes the reliability of the statistics. For reliable statistics with minimal numerical dispersion, it is desired to minimize the size of ensemble domain and maximize the number of MC particles.<sup>26</sup> In this way, the ensemble statistics would tend to the desired filtered values. The transfer of information from FD grid points to the MC particle locations is accomplished via interpolation. The size of the ensemble domain and the number of particles within it is in general determined by a consistency analysis.<sup>30,33,40,44,51,87,88</sup> This analysis can be performed because some filtered quantities are obtained by MC, some by FD, and some by both methods. That is, there is a “redundancy” in determination of some quantities. In general, the consistency analysis can be performed for any filtered quantity for which a FD transport equation is solved and where all the unclosed terms are evaluated from MC. Here, the filtered density, the Favré filtered mixture fraction and the Favré filtered mixture fraction variance are used. The boundary conditions for the Monte Carlo simulation require no special treatment. Particles are free to leave the computational domain as guided by the SDEs. If at any time conditions exist at some location on the boundary that require particles to enter the computational domain away from the inlet, then the values assigned to those particles yield a zero derivative boundary condition at that location

In an attempt to reduce the computational cost and maintain a nearly uniform particle distribution in a variable density flow, the MC particles enter the computational domain uniformly but carry a weight ( $\omega$ ) that is proportional to the filtered density at the inlet. This strictly numerical treatment is somewhat analogous to grid compression in FD schemes.

Figure 3 shows the sample instantaneous contours of the ensembled particle weights (*i.e.*  $\sum_{n \in (\Delta_E)^3} \omega^{(n)}$ ) and the particle number density (*i.e.*  $\sum_{n \in (\Delta_E)^3} (1)$ ) at each FD grid point. In practice, the particles evolve according to the discrete weighted SFMDF, denoted by  $F_N$ ,

$$F_N(\boldsymbol{\psi}, \mathbf{x}; t) = \Delta m \sum_{n=1}^{N_p} \omega^{(n)} \delta(\boldsymbol{\psi} - \boldsymbol{\phi}^{(n)}) \delta(\mathbf{x} - \mathbf{x}^{(n)}) \quad (2.38)$$

where  $\omega^{(n)}$  is the weight of the  $n^{\text{th}}$  particle and  $\Delta m$  is the unit mass. The SFMDF is the expectation of the discrete SFMDF<sup>26</sup>

$$F_\ell(\boldsymbol{\psi}, \mathbf{x}; t) = \langle F_N(\boldsymbol{\psi}, \mathbf{x}; t) \rangle \quad (2.39)$$

where the brackets represent ensemble averaging. By integrating Eq. (2.39) over the scalar sample space and within the ensemble domain volume, it can be shown that<sup>107</sup>

$$\langle \rho \rangle_\ell \approx \frac{\Delta m}{(\Delta_E)^3} \sum_{n \in (\Delta_E)^3} \omega^{(n)} \quad (2.40)$$

The Favré filtered value of a quantity  $\hat{Q}(\boldsymbol{\phi}(\mathbf{x}, t))$  is obtained by a weighted average

$$\langle \hat{Q}(\boldsymbol{\phi}(\mathbf{x}, t)) \rangle_L \approx \frac{\sum_{n \in (\Delta_E)^3} \omega^{(n)} \hat{Q}(\boldsymbol{\phi}^{(n)})}{\sum_{n \in (\Delta_E)^3} \omega^{(n)}} \quad (2.41)$$

Equations (2.40), and (2.41) are approximations due to statistical errors associated with finite ensemble domain size and particle number density. In the limit of  $\Delta_E \rightarrow 0$  and  $N_E \rightarrow \infty$  they become exact.<sup>26</sup> An alternate formulation for the filtered density may be obtained from Eq. (2.41), by considering  $\hat{Q}(\boldsymbol{\phi}(\mathbf{x}, t)) = 1/\rho(\boldsymbol{\phi}(\mathbf{x}, t))$ ,

$$\frac{\sum_{n \in (\Delta_E)^3} \omega^{(n)} (1/\rho(\boldsymbol{\phi}^{(n)}))}{\sum_{n \in (\Delta_E)^3} \omega^{(n)}} \approx \left\langle \frac{1}{\rho(\boldsymbol{\phi}(\mathbf{x}, t))} \right\rangle_L = \frac{1}{\langle \rho \rangle_\ell} \quad (2.42)$$

where  $\rho(\boldsymbol{\phi}^{(n)})$  is the fluid density of the  $n^{\text{th}}$  MC particle. This particle “localized” fluid density can be assumed proportional to the particle weight,

$$\rho(\boldsymbol{\phi}^{(n)}) = \frac{\Delta m}{(\Delta_E)^3} N_{E0} \omega^{(n)} \quad (2.43)$$

where  $N_{E0}$  is the nominal particle number density. Combining Eqs. (2.42) and (2.43) yields a modified formulation for the filtered density,

$$\langle \rho \rangle_\ell \approx \frac{\Delta m}{(\Delta_E)^3} \frac{N_{E0}}{N_E} \sum_{n \in (\Delta_E)^3} \omega^{(n)} \quad (2.44)$$

Equation (2.44) essentially considers an average particle weight in an ensemble domain as representative of the weights in that domain. This formulation, therefore, accounts for the local variations in the particle number density and decreases the level of oscillations in the filtered density values. With uniform weights, Eqs. (2.40), and (2.41) become

$$\langle \rho \rangle_\ell \approx \frac{\Delta m}{(\Delta_E)^3} N_E \quad (2.45)$$

$$\left\langle \hat{Q}(\phi(\mathbf{x}, t)) \right\rangle_L \approx \frac{1}{N_E} \sum_{n \in (\Delta_E)^3} \hat{Q}(\phi^{(n)}) \quad (2.46)$$

Equation (2.45) implies that the filtered density is proportional to the particle number density.<sup>26</sup> As such, the particle number density significantly decreases in the regions of high temperature. The implementation of variable weights allows for the increase of the particle number density without a proportional increase outside of the reaction zones.

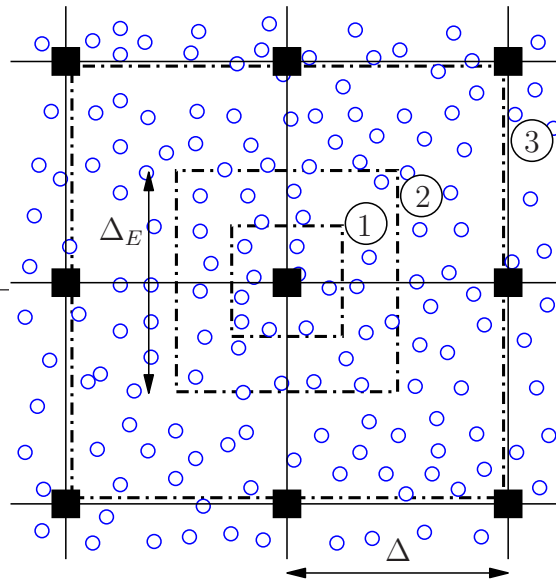


Figure 1: Numerical procedure. Elements of computation as used in a typical LES/FDF. Solid squares denote the FD points, and the circles denote the MC particles. Also shown are three different ensemble domains: 1 ( $\Delta_E = \Delta/2$ ,  $N_E \approx 10$ ), 2 ( $\Delta_E = \Delta$ ,  $N_E \approx 40$ ), 3 ( $\Delta_E = 2\Delta$ ,  $N_E \approx 160$ ).

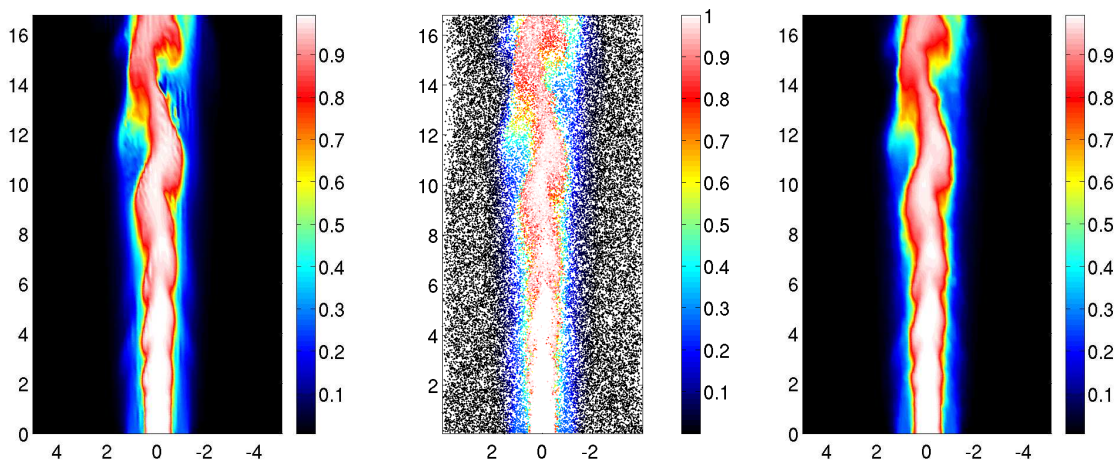


Figure 2: Visualization of the different types of variables present in the hybrid solver. From left-to-right: FD, MC, and ensemble averaged MC (see Figure 1) mixture fraction. The data shown are those of Sandia/TUD simulations as discussed in chapter 3.

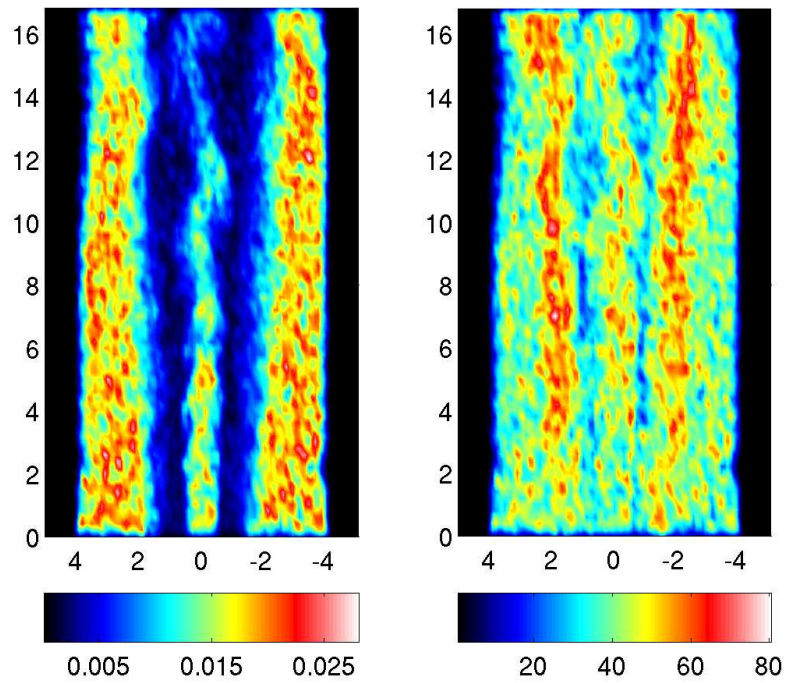


Figure 3: Instantaneous contours of the ensembled particle weights (left) and the particle number density per ensemble domain (right) for the MC simulation. The data shown are that of Sandia/TUD simulations as discussed in chapter 3.

## 3.0 RESULTS

The LES/SFMDF is used for prediction of two flame configurations. The first is considered in the experiments of the Combustion Research Facility at the Sandia National Laboratories (SNL) and the Technische Universität Darmstadt (TUD).<sup>1-3</sup> This is a turbulent piloted non-premixed methane jet flame. The second is considered by the Combustion Research Facility at the Sandia National Laboratories and the Thermal Research Group at the University of Sydney.<sup>4-11</sup> This is a turbulent bluff-body stabilized hydrogen-methane jet flame. These flame are labeled as the Sandia/TUD, and the Sydney/Sandia, respectively. The LES/SFMDF is used in conjunction with the MKEV hydrodynamic SGS model, except where explicitly noted otherwise.

### 3.1 SANDIA/TUD FLAME

#### 3.1.1 Configuration

The Sandia/TUD piloted flames have been studied experimentally by Barlow *et al.*,<sup>1,2</sup> and Schneider *et al.*<sup>3</sup> In the experiments, three turbulent flames are considered: Flames D, E and F. Figure 4 schematically shows the flame configuration. The central jet is maintained at a temperature of 294 K and is composed of 25% methane ( $CH_4$ ) and 75% dry air by volume. Such partial premixing reduces the formation of the soot precursors. The pilot is a lean mixture of acetylene ( $C_2H_2$ ), hydrogen ( $H_2$ ), air, carbon dioxide ( $CO_2$ ) and nitrogen ( $N_2$ ) with the same equilibrium composition as the fuel jet and a temperature of 1880 K. The energy release of the pilot is approximately 6% that of the main jet. The coflow is composed

of air at a temperature of 291 K. The geometrical configuration in all Sandia/TUD flames is the same, but the jet inlet velocity is varied. The jet velocity increases from flames D to E to F increasing the probability of localized non-equilibrium effects. In Flame D, the fuel jet bulk velocity is the lowest,  $49.6 \text{ m/s}$ , and the flame is close to equilibrium with a single reaction zone occurring near the stoichiometric mixture fraction,  $Z_s = 0.351$ . Only Flame D is considered in this work. The objective is to assess the predictive capability of the LES/SFMDF in capturing the essential flow features. This is a necessary step before consideration of the non-equilibrium flames (E and F). The jet diameter  $D_J = 7.2 \text{ mm}$ , and the pilot diameter is  $18.2 \text{ mm}$ . The Reynolds number, based on the jet diameter, is  $Re = 22,400$ .

Sandia/TUD piloted jet flames have been the subject of broad investigations by other computational and modeling methodologies.<sup>42,46–49</sup>

### 3.1.2 Numerical Specifications

The values of the flow variables at the inlet are set to those available from the experiments. This includes the velocity, the turbulent intensity, and the mixture fraction. The flow is excited by superimposing oscillating axisymmetric and helical perturbations onto the velocity profile at the inlet. This procedure is similar to that of Danaila and Boersma,<sup>108</sup> with the amplitude of the forcing adjusted to match the experimental turbulent intensity of the streamwise velocity at the inlet. The key simulation parameters are presented in Table 1. The simulations are conducted on a 3D Cartesian mesh with uniformly spaced grid points. The computational domain spans a region of  $18D_J \times 10D_J \times 10D_J$  in the streamwise ( $x$ ) and the two lateral ( $y, z$ ) directions, respectively. The number of grid points is  $91 \times 101 \times 101$  in the  $x, y$ , and  $z$  directions, respectively. The filter size is set equal to  $\Delta_L = 2(\Delta x \Delta y \Delta z)^{1/3}$ , where the  $\Delta x, \Delta y$ , and  $\Delta z$  are the grid spacing in the corresponding directions. The size of the ensemble domain in the MC simulation is set equal to the filter size. There are approximately 40 particles in each ensemble domain. Per results of extensive previous studies<sup>12,30,33,44</sup> the number is sufficient to yield an excellent statistical accuracy with minimal dispersive errors. In total, there are about 2.1 million MC particles within the computational domain at all

Table 1: Sandia/TUD: Summary of the LES/SFMDF parameters and reference quantities.

Parameter	Description	Value
$C_I$	MKEV model parameter	0.0
$C_R$	MKEV model parameter	0.026
$C_\Omega$	SGS mixing frequency	8
$Le$	Lewis number	1
$Pr$	Prandtl number	0.75
$Sc$	Schmidt number	0.75
$Sc_t$	SGS Schmidt number	0.75
$t_{ref}$ [s]	Reference time	$1.45 \times 10^{-4}$
$T_{ref}$ [K]	Reference temperature	291
$\nu_{ref}$ [ $m^2/s$ ]	Kinematic viscosity	$1.58 \times 10^{-5}$

times. The simulation results are monitored to ensure that the particles fully encompass and extend well beyond the regions of non-zero vorticity and reaction. First the consistency and accuracy of the simulations are assessed. Next, the predictive capability of the LES/SFMDF is demonstrated by comparing the flow statistics and resolved PDFs with the experimental data. The statistics are obtained by long-time averaging of the filtered fields during several flow through times. The collection of the data is initialized after the flow has swept the domain during the initial two flow through times. Simultaneously, the PDFs are constructed based on the LES/SFMDF data resolved at the FD grid points residing within a circular band of width  $\Delta$ . The center of each band is located at a radial location where experimental data are available. The notations  $\overline{Q}$  and  $RMS(Q)$  denote the time-averaged mean and root mean square values of the variable  $Q$ , respectively. The radial ( $r = \sqrt{y^2 + z^2}$ ) profiles of the streamwise velocity<sup>†</sup> at the inlet are compared to the experimental data in Figure 5.

The flamelet table for a constant strain rate of  $\chi = 100$  1/s is used to relate the

---

<sup>†</sup>Unless otherwise stated all of the LES/SFMDF variables in this chapter, except for the filtered density, are Favré filtered. This prefix will be omitted henceforth for clarity.

thermo-chemical variables to the mixture fraction. The choice of the strain rate is consistent with previous studies of Sandia flames.<sup>52</sup> The values of the temperature and several mass fractions as obtained by the flamelet model are compared to the experimental data in Fig. 6. The values for various strain rates are shown. The best agreement is obtained with  $\chi = 100$  1/s. It can also be observed that at low strain rates the experimental data are not predicted well on the fuel rich side ( $Z > Z_s$ ) of the flame.

The computational costs associated with LES/SFMDF depends, obviously, on the parameters of the simulations. For the case reported here, the simulations required about 110 hours of CPU time on a SUN Fire 4800 with 6 processors. This includes the times required for consistency tests and ensemble averaging of data. The computational time for LES without including SGS effects<sup>30</sup> is about 10-12 times less. However such simulations yield erroneous predictions and in many cases lead to numerical instabilities. For further comparative assessment of the computational requirements of the FDF in comparison to non-FDF methods, we refer to previous work.<sup>12,30,33,44</sup>

### 3.1.3 Consistency of the LES/SFMDF

The objective of this subsection is to demonstrate the consistency of the LES/SFMDF in the Sandia/TUD simulations. Typically, this is accomplished by considering various values of the ensemble domain sizes and particle densities. The simplest consistency check is via flow visualization. For example, Fig. 7 shows the instantaneous contours of the filtered mixture fraction field as obtained by the FD and the MC methods. The central jet lies in the middle along the streamwise coordinate, surrounded by a pilot where the temperature is the highest and encircled by the air coflow. Due to the presence of helical instabilities, the instantaneous flow is asymmetric. The similarity of the results in the two figures is observed at all other times and is also observed for the temperature. This consistency is further assessed by comparing statistics of the redundant quantities. The consistency can be demonstrated in increasing detail by considering both instantaneous and the time averaged values of the redundant variables. These are the density, mixture fraction and the mixture fraction variance.

Figures 8 and 9 show the instantaneous density field. The two results are very close. The MC filtered density in both figures is calculated using Eq. (2.44). The key differences between the two methods are exemplified by the presence of numerical oscillations in the FD and statistical variability errors. The consistency results for the instantaneous and time averaged mixture fraction are shown in Figs. 10–13. The instantaneous scatter plots for the four adjacent streamwise segments of the computational domain show that the level of correlation is reasonable. The corresponding time averaged results show a very good agreement. This indicates that the level of scatter observed in the instantaneous data is a result of combined effects of the numerical oscillations in the FD and localized stochastic diffusion in the MC. Both effects are largely diminished by the time averaging. Furthermore, these results indicate that for the mean of the mixture fraction, the statistical errors associated with a finite number of particles are small. The correlation is further quantified by calculating the correlation coefficients for the FD and MC data residing within several streamwise segments of the computational domain. Figure 13 shows the temporal evolution of the correlations coefficients calculated for the eight adjacent streamwise segments. The values vary little with time hence implying a consistent LES/SFMDF at all times. Similarly to the mixture fraction, the mixture fraction variance is also subjected to the consistency analysis. The instantaneous and time averaged results are shown in Figs. 14–17. As before, the scatter plots for the four adjacent streamwise segments of the computational domain are considered. The instantaneous correlation is affected by a combined effect of numerical oscillations in the FD and a combination of stochastic diffusion and statistical errors in the MC. The MC also overpredicts the FD result in both instantaneous and time averaged results. This is consistent with previous studies.<sup>12,30,43,44</sup> Figure 17 shows the temporal evolution of the correlations coefficients calculated for the eight adjacent streamwise segments. While the values are lower than those for the mixture fraction, they vary little with time again suggesting a similar level of consistency of the mixture fraction variance at all times.

### 3.1.4 Comparisons with Experimental Data

The capability of the method to predict the hydrodynamics field is demonstrated by comparison with the (reported) flow statistics. The mean and the RMS values of the streamwise and radial velocities are shown in Figs. 18 and 19, respectively. The region close to the inlet is dominated by the molecular diffusion and the jet exhibits a laminar-like behavior. Farther downstream, the growth of perturbations is manifested by the formation of large scale coherent vortices. The figures indicate that the flow is adequately excited and the predicted results are in good agreement with data.

The comparison of the time averaged mixture fraction and temperature statistics with the data are shown in Fig. 20. While most of the experimental data are linearly interpolated for comparison, the figure shows a good qualitative agreement.

The radial distribution of the mixture fraction is shown to compare well with data (Fig. 21). Similar agreement is observed at other available streamwise locations. The mean temperature values in Fig. 22 are overpredicted on the fuel rich side. This is due to the premixing of methane with air as indicated previously.<sup>48</sup>

The “resolved” RMS values of the mixture fraction and temperature are in good agreement with data (Figs. 21, 22). However, the “total” RMS values, including the contributions of both the resolved and the SGS fields, are higher than values reported experimentally. The contribution of the SGS to the total scalar energy is about 20% which is expected in LES. The higher values of the total RMS, as predicted by LES/SF MDF, are not due to MC numerical dispersion because the FD results do indeed yield the same values. The level of SGS variance can be decreased by increasing the magnitude of  $C_\Omega$ . However, this would not alter the total RMS values as well. It is possible that some contributions to this variance is not included in the measurements due to finite probe size. Higher resolution measurements would determine the allocations of scalar variance to the resolved and the SGS fields.

The statistics of the mass fractions (denoted by  $Y$ ) of several of the species are compared with data in Figs. 23–27. The reactants’ mass fractions are underpredicted and the products are overpredicted on the fuel rich side of the flame. The mean values of the mass fractions

of the major and the minor species compare well with experimental data. All of the results indicate the adequacy of the flamelet table in relating the thermo-chemical variables to the mixture fraction, and also the good predictive capability of the LES/SFMDF for this flame.

The PDFs of the resolved scalar fields are compared with those measured experimentally. Figure 28 specifies the spacial locations where the PDFs are constructed. Figures 29 and 30 show the PDFs of the resolved mixture fraction and temperature, respectively. The comparison of the resolved PDFs at select radial locations with the experimental data is shown in Fig. 31 for the mixture fraction and Fig. 30 for the temperature. The overall agreement between LES/SFMDF and experimental measurements is good. The most visible differences appear for the mixture fraction at:  $x/D_J = 7.5$  and  $r = 0.0 \text{ mm}$ , where the LES/SFMDF predicts a sharp peak of the fuel rich mixture while the experiment indicates a broader PDF, and at  $x/D_J = 7.5$  and  $r = 16.0 \text{ mm}$  where the LES/SFMDF predicts a bimodal PDF while the experiment shows a narrow PDF of the oxidizer mixture. The discrepancies can be partly attributed to the experimental errors. The latter are most pronounced in the pure fuel or oxidizer streams where the experiments over- and under-predict the mixture fraction, respectively. However, at  $r = 16 \text{ mm}$ , LES/SFMDF appears to predict an intermittent vortical structures that convect a small amount of pilot mixture. The discrepancies between the PDFs of the temperature at  $r = 8 \text{ mm}$  and  $r = 12 \text{ mm}$  can be attributed to the excessive diffusion of the temperature in the simulations.

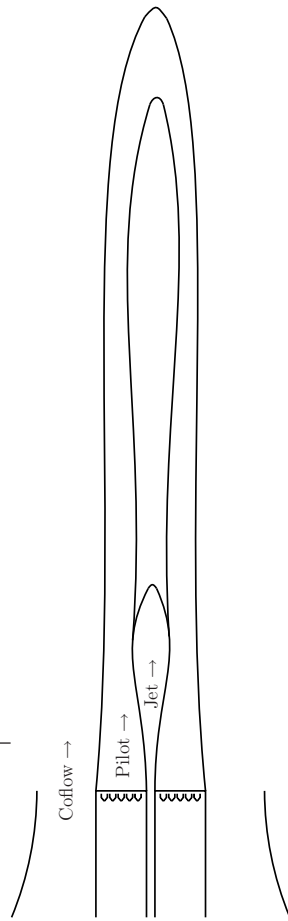


Figure 4: Sandia/TUD: Flame configuration.

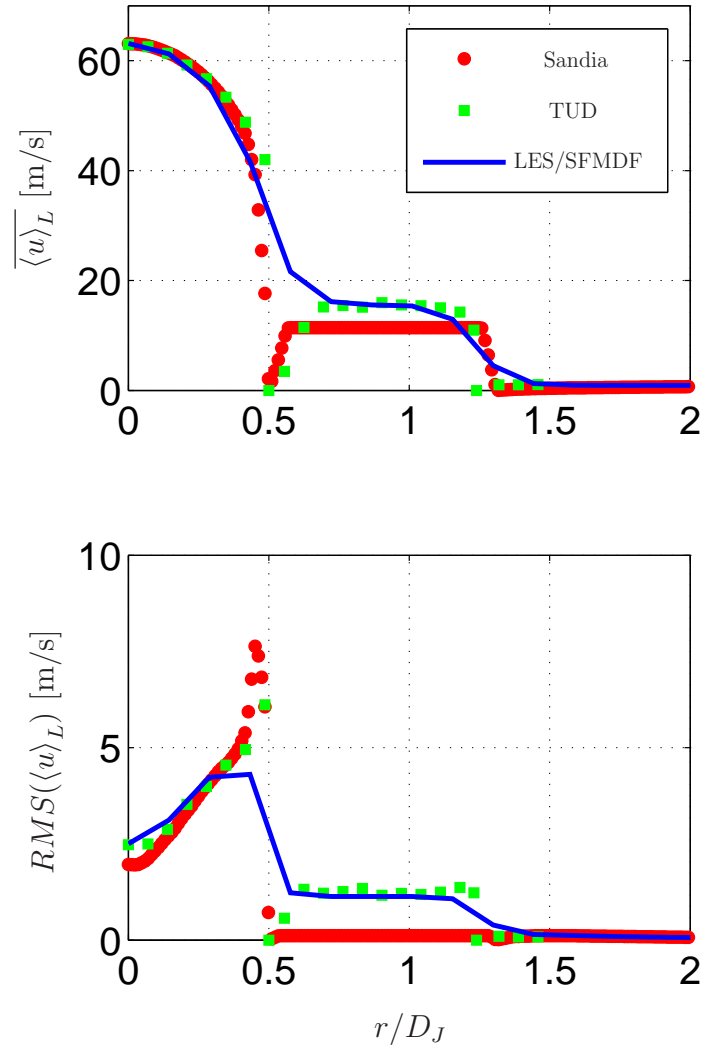


Figure 5: Sandia/TUD: Radial profiles of the mean and the resolved RMS values of the streamwise velocity at the inlet.

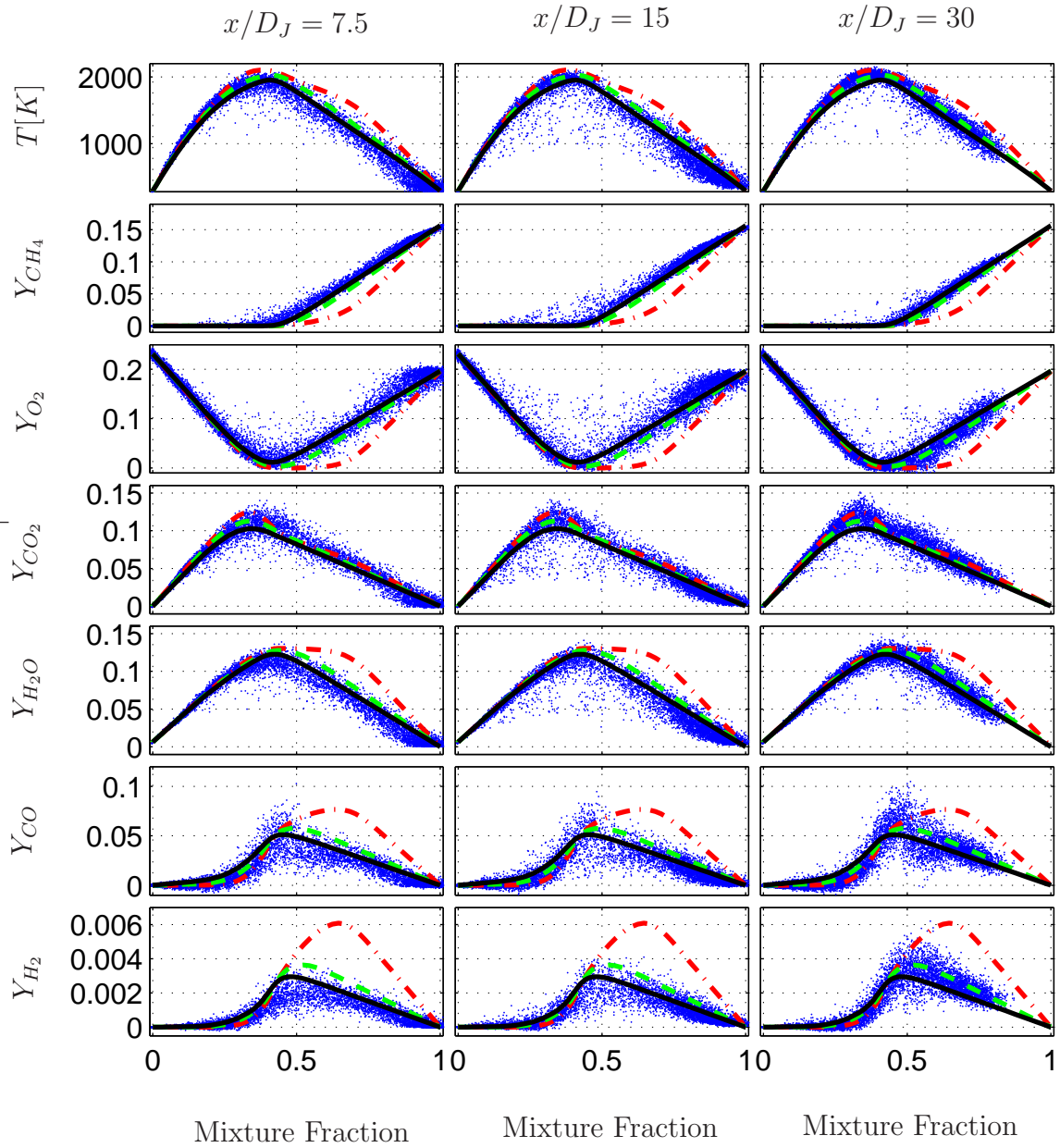


Figure 6: Scalar values versus the mixture fraction as predicted by the flamelet model with several strain rates ( $\chi$ ), and measured experimentally. Dots denote the experimental data,  $\text{---}$   $\chi = 10 \text{ 1/s}$ ,  $\text{---}$   $\chi = 100 \text{ 1/s}$ ,  $\text{---}$   $\chi = 400 \text{ 1/s}$ .

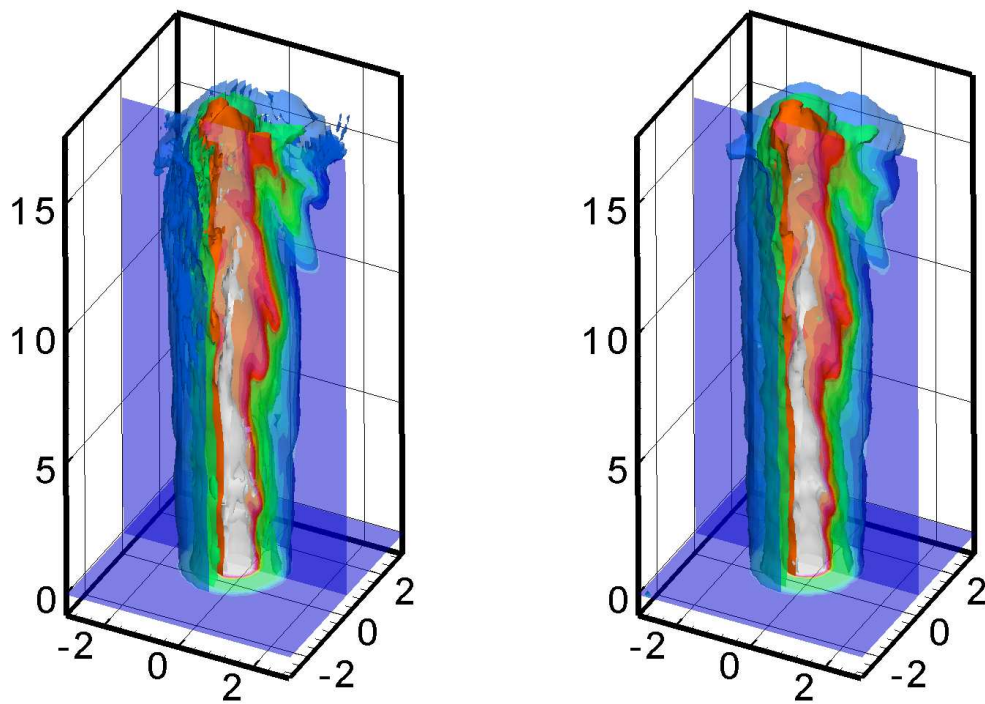


Figure 7: Sandia/TUD: Instantaneous contours of the mixture fraction as obtained by FD (left) and MC (right) at  $t = 287.95t_{ref}$ . The four iso-surfaces displayed are 0.08 (blue), 0.26, 0.6, and 0.98 (white).

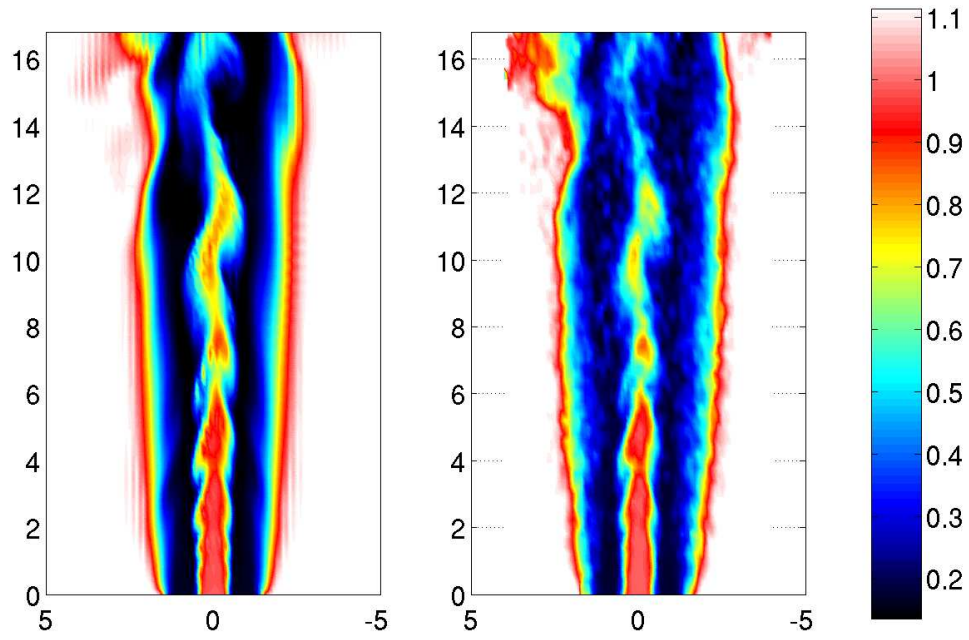


Figure 8: Sandia/TUD: Instantaneous contours of the density obtained by FD (left) and MC (right) at  $z/D_J = 0$  and  $t = 143.98t_{ref}$ .

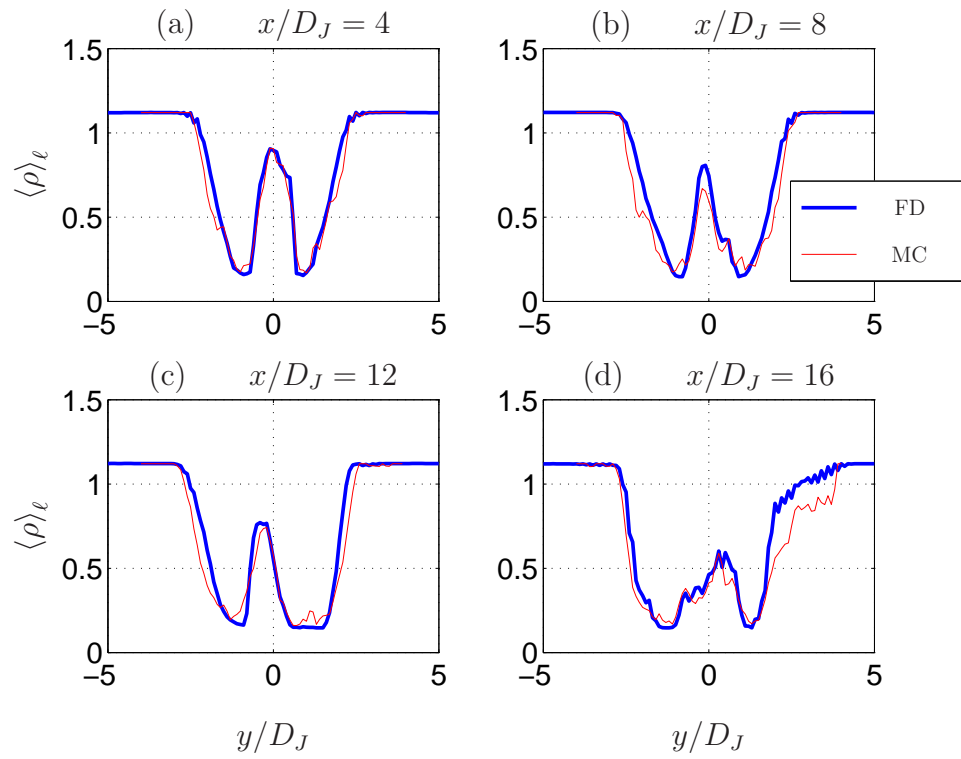


Figure 9: Sandia/TUD: Instantaneous profiles of the density at  $z/D_J = 0$  and  $t = 143.98t_{ref}$ .

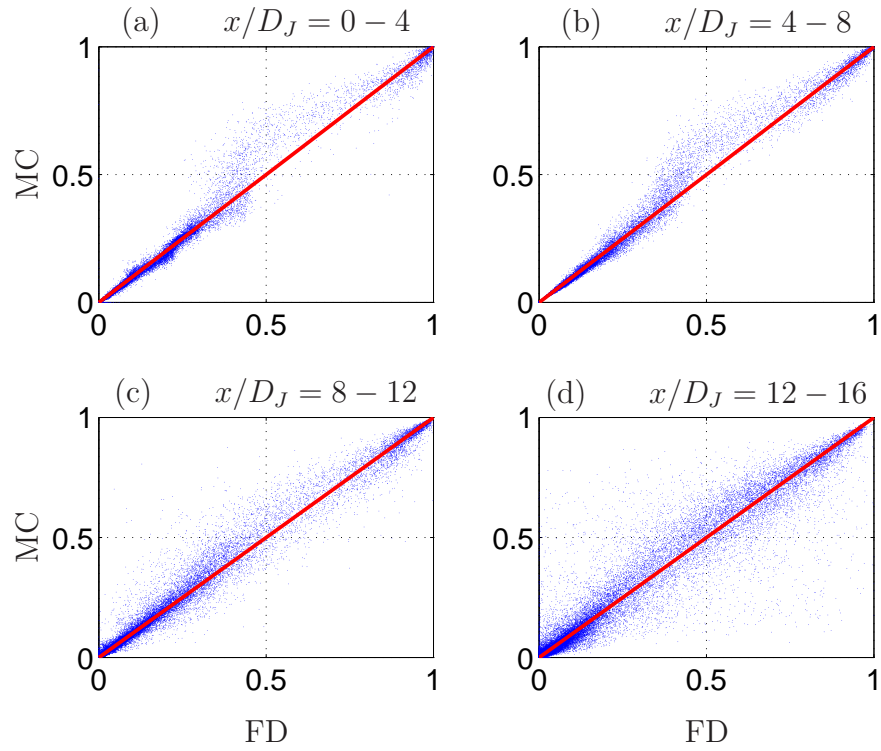


Figure 10: Sandia/TUD: Scatter plots of the instantaneous FD and MC values of the mixture fraction at  $t = 143.98t_{ref}$ . Correlation coefficients are (a) 0.9941, (b) 0.9956, (c) 0.9925, and (d) 0.9760.

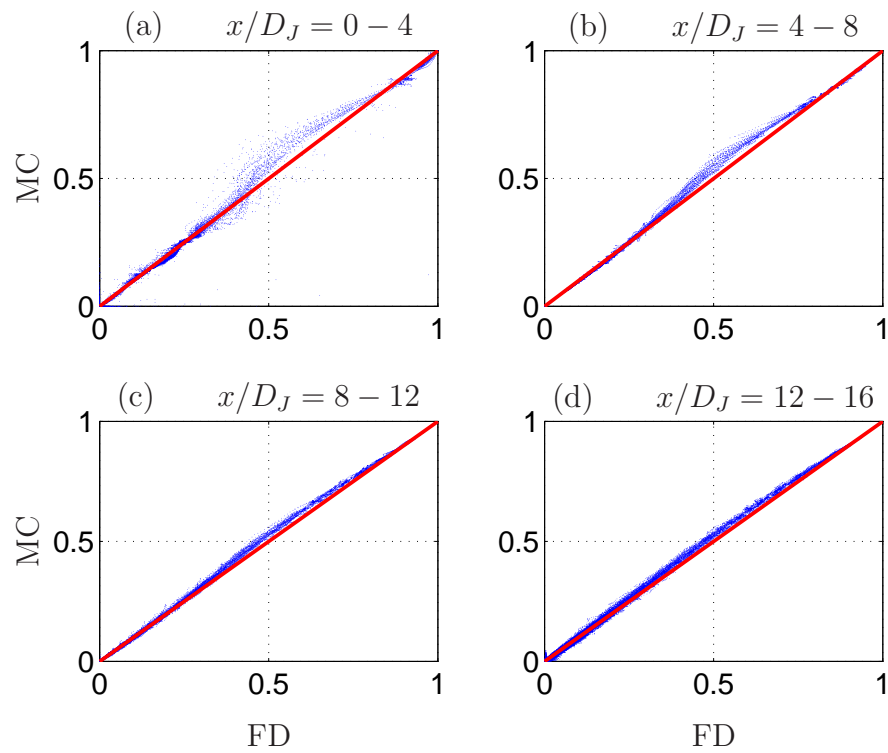


Figure 11: Sandia/TUD: Scatter plots of the time averaged FD and MC values of the mixture fraction. Correlation coefficients are (a) 0.9979, (b) 0.9993, (c) 0.9996, and (d) 0.9994.

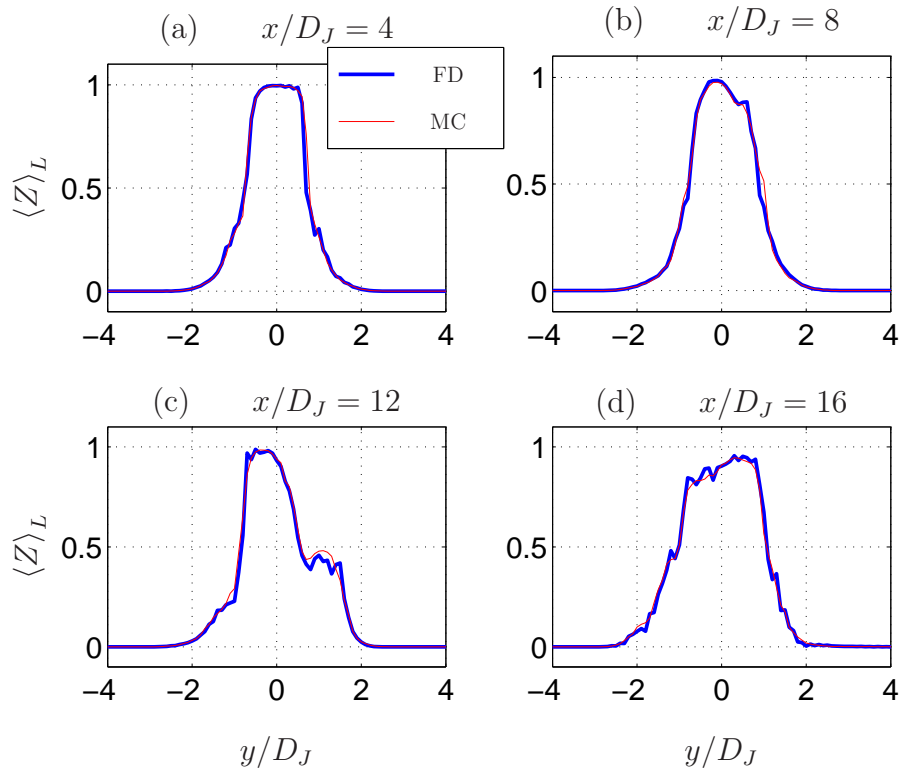


Figure 12: Sandia/TUD: Instantaneous profiles of the mixture fraction at  $z/D_J = 0$  and  $t = 143.98t_{ref}$ .

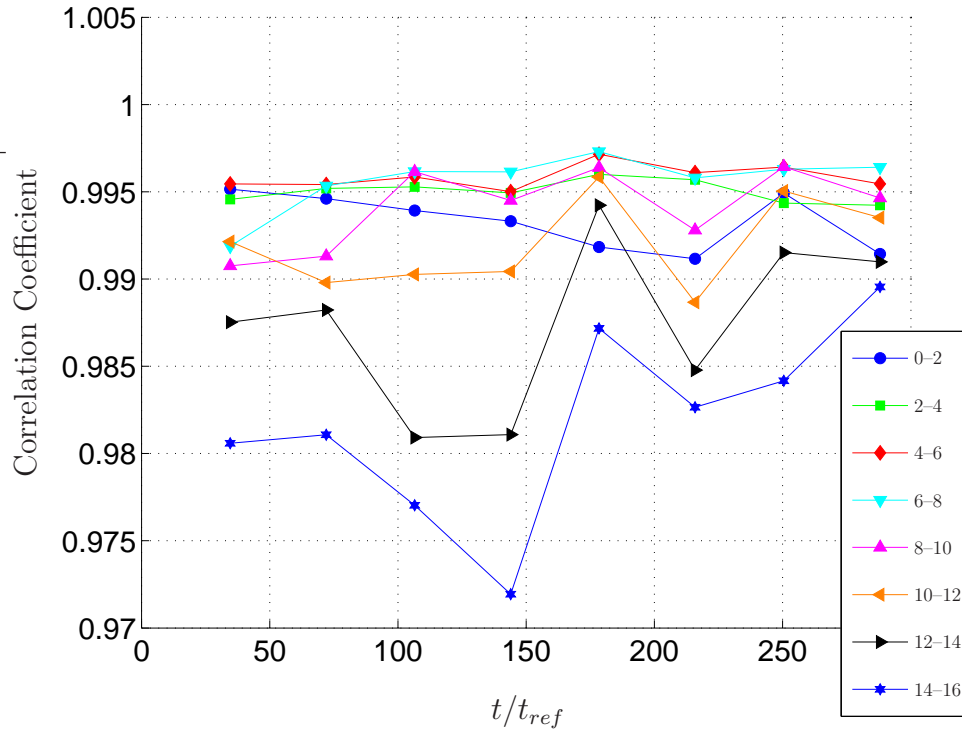


Figure 13: Sandia/TUD: Temporal evolution of the correlation coefficients computed from the instantaneous FD and MC mixture fraction data. The legend denotes the streamwise segment of the computational domain for which the correlation coefficient is computed.

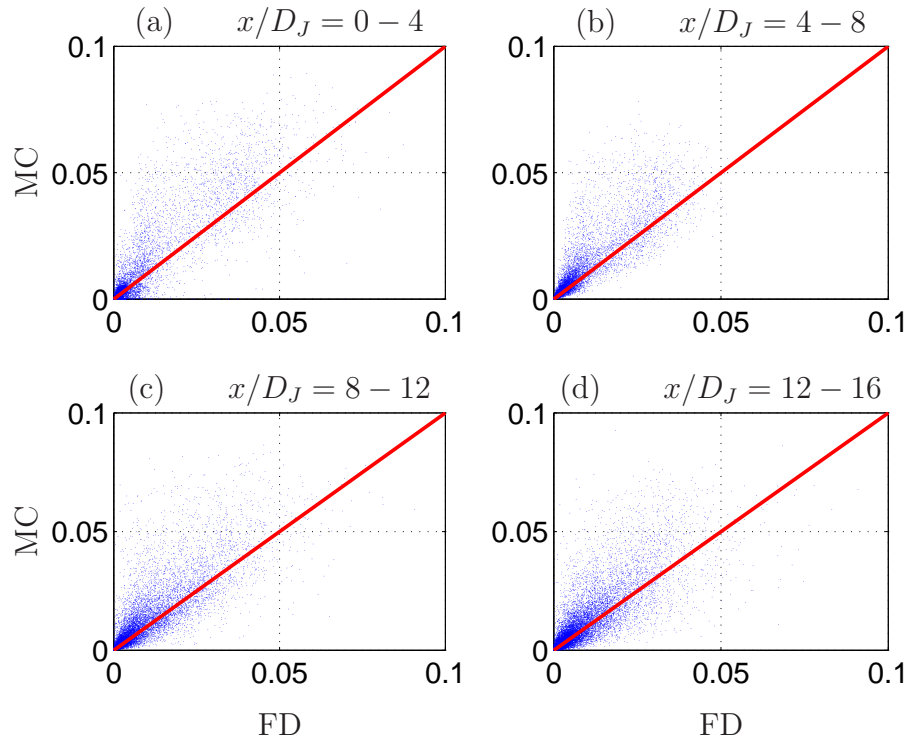


Figure 14: Sandia/TUD: Scatter plots of the instantaneous FD and MC values of the mixture fraction variance at  $t = 143.98t_{ref}$ . Correlation coefficients are (a) 0.9128, (b) 0.9015, (c) 0.8879, and (d) 0.8204.

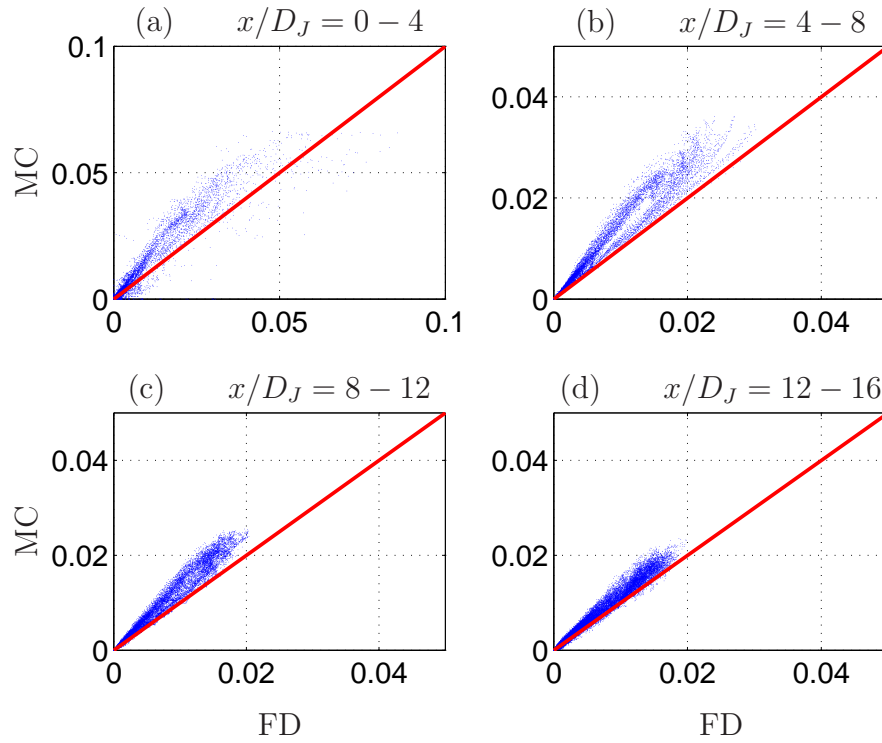


Figure 15: Sandia/TUD: Scatter plots of the time averaged FD and MC values of the mixture fraction variance. Correlation coefficients are (a) 0.9672, (b) 0.9886, (c) 0.9928, and (d) 0.9939.

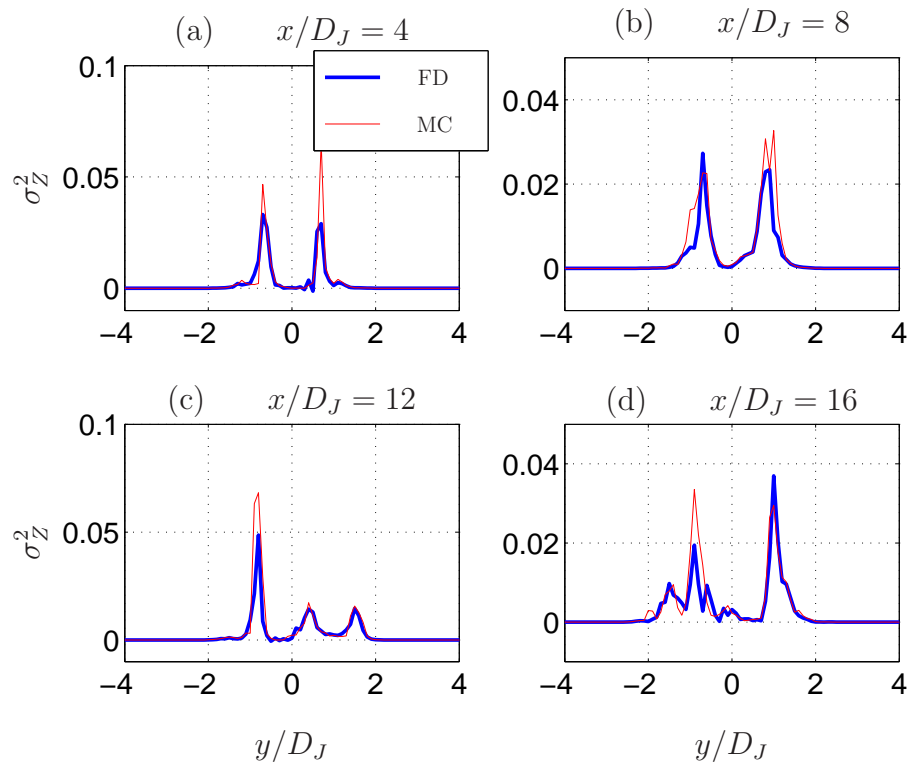


Figure 16: Sandia/TUD: Instantaneous profiles of the mixture fraction variance at  $z/D_J = 0$  and  $t = 143.98t_{ref}$ .

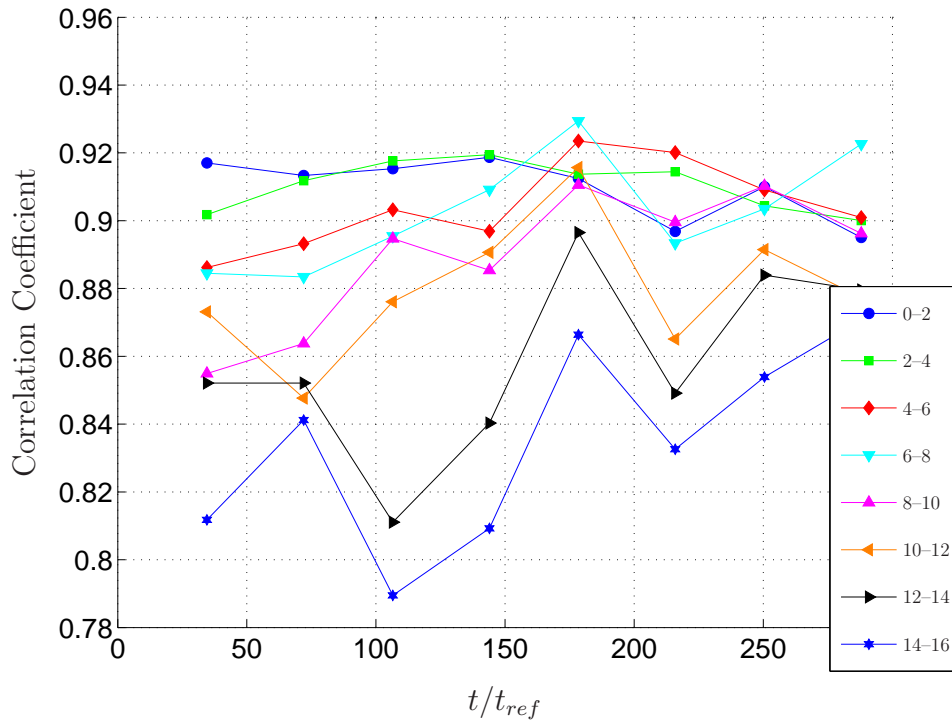


Figure 17: Sandia/TUD: Temporal evolution of the correlation coefficients computed from the instantaneous FD and MC mixture fraction variance data. The legend denotes the streamwise segment of the computational domain for which the correlation coefficient is computed.

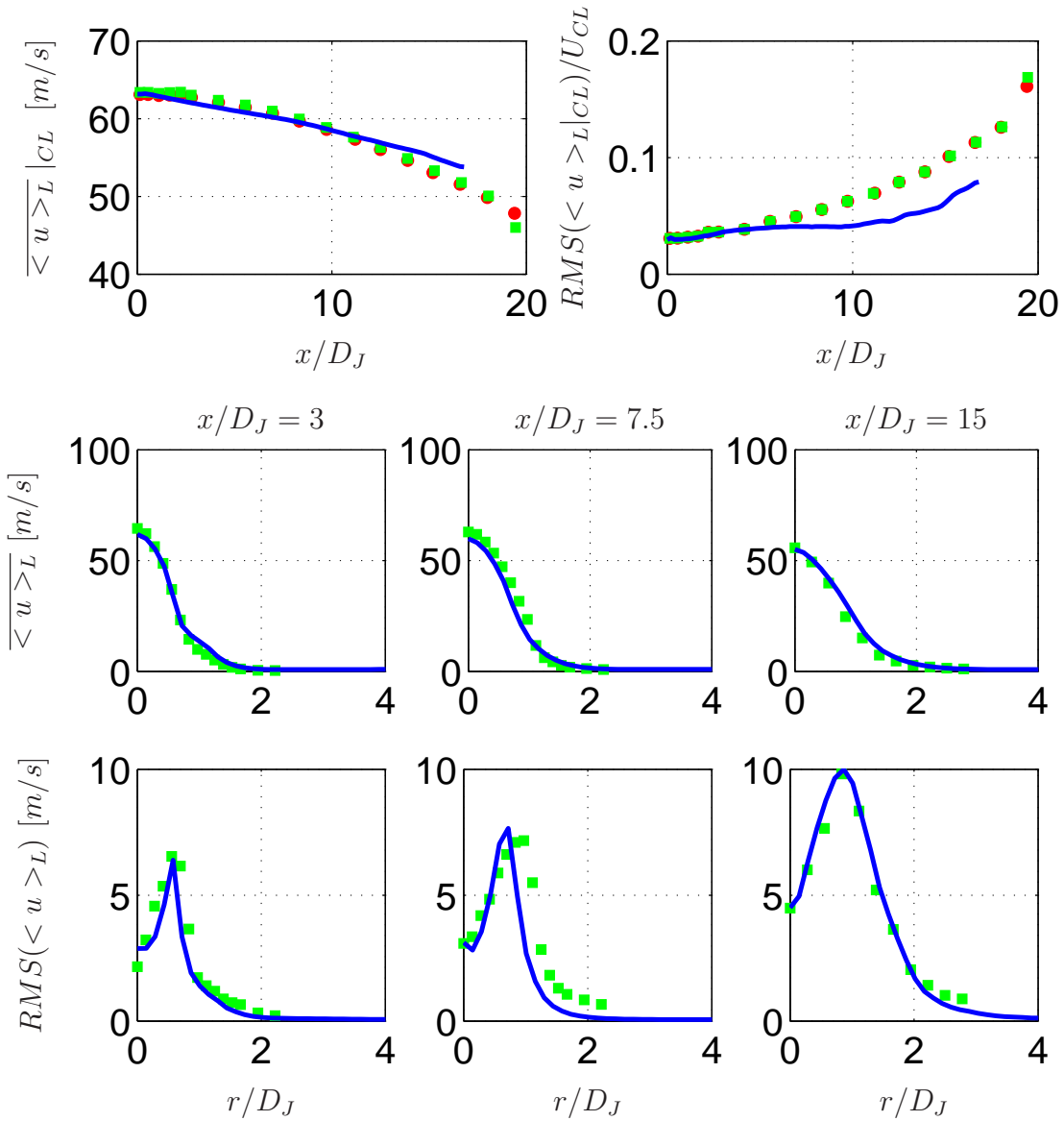


Figure 18: Sandia/TUD: Profiles of the mean and the resolved RMS values of the streamwise velocity. — LES/SFMDP, • Sandia experiment, ■ TUD experiment.

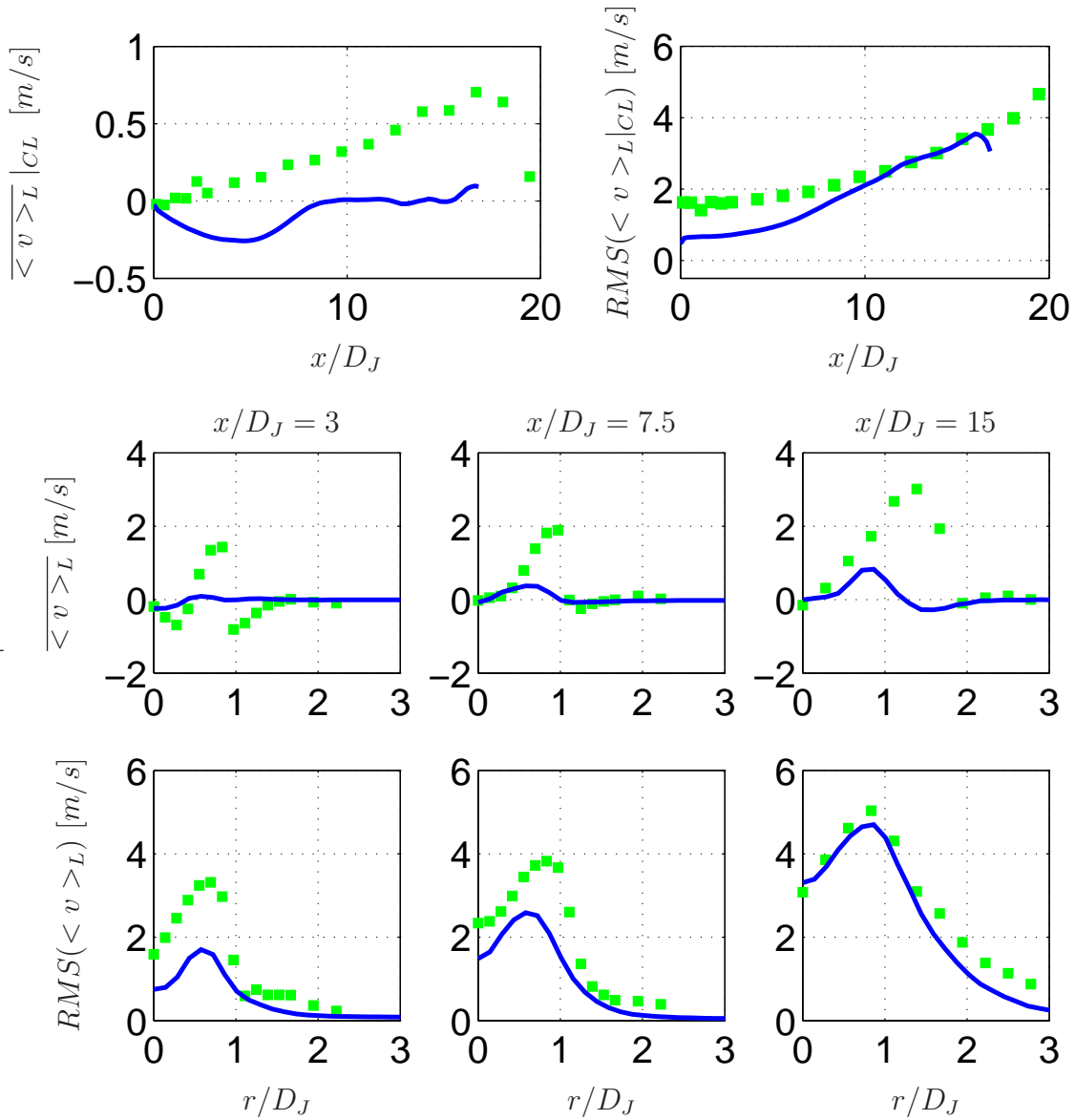


Figure 19: Sandia/TUD: Profiles of the mean and the resolved RMS values of the radial velocity. — LES/SFMDP, ■ TUD experiment.

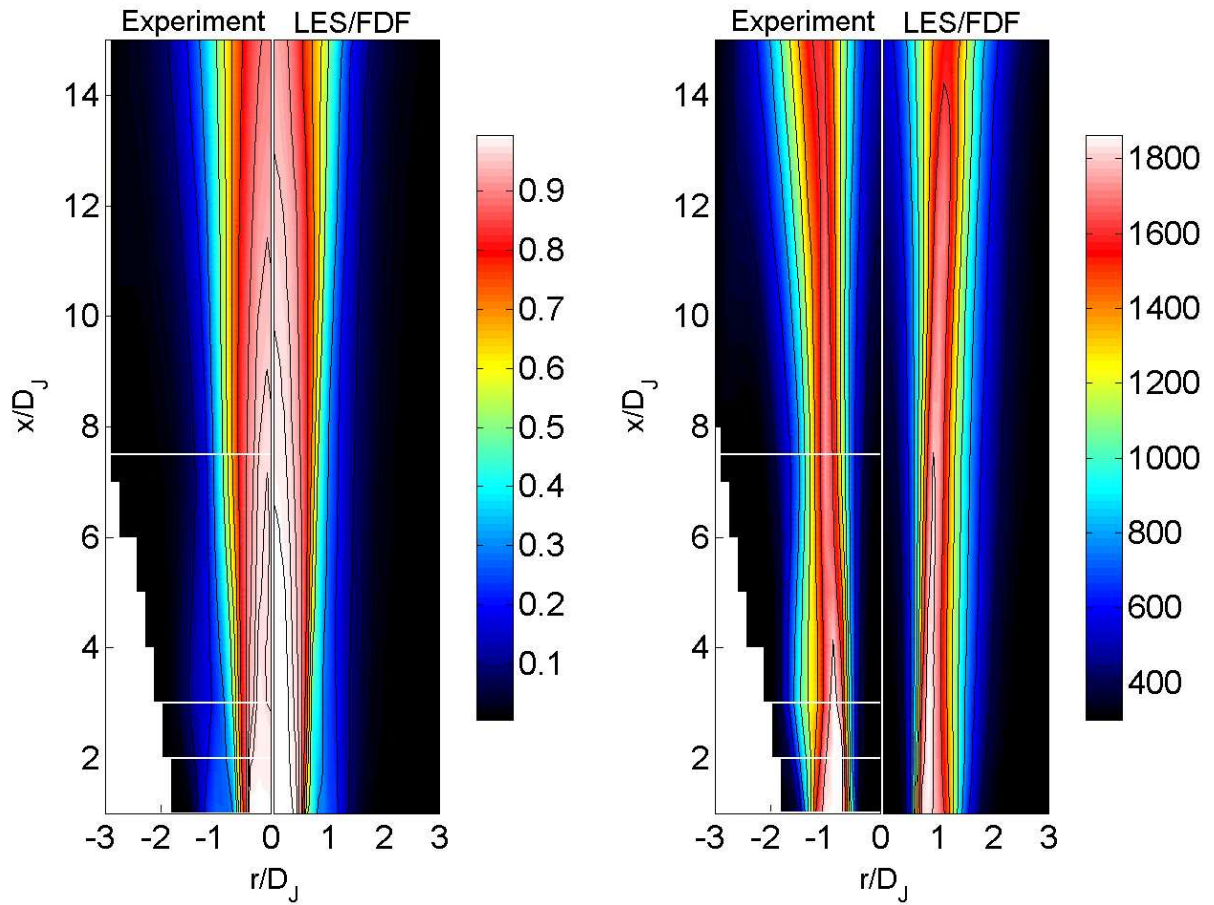


Figure 20: Sandia/TUD: Time averaged contours of the mean values of the mixture fraction (left) and temperature (right). Beyond the first and the end points, the horizontal lines denote the locations of the experimental data. These data are interpolated at all other locations.

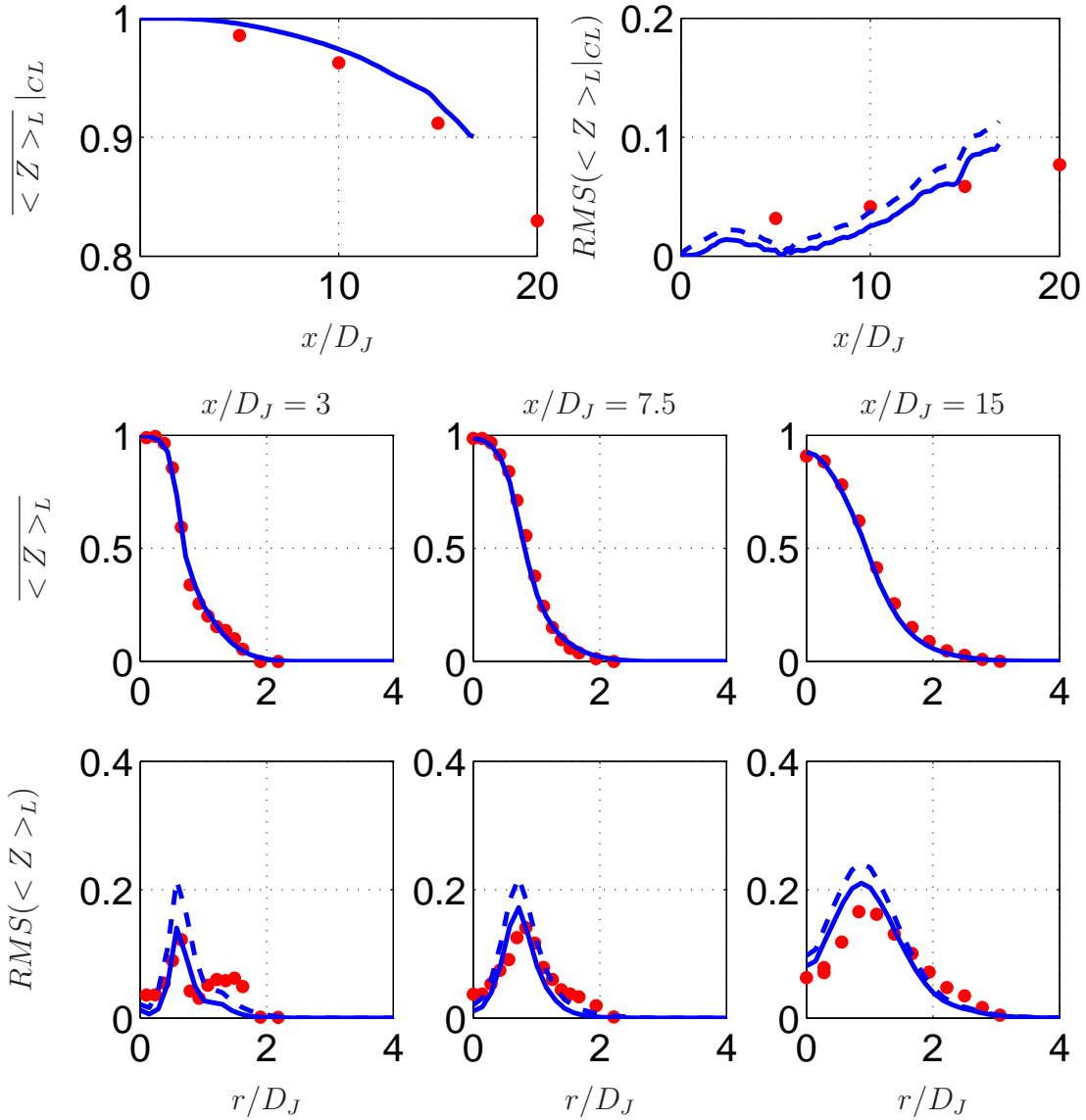


Figure 21: Sandia/TUD: Profiles of the mean and the RMS values of the mixture fraction.

— Resolved LES/SFMDF, - - Total LES/SFMDF, • Sandia experiment.

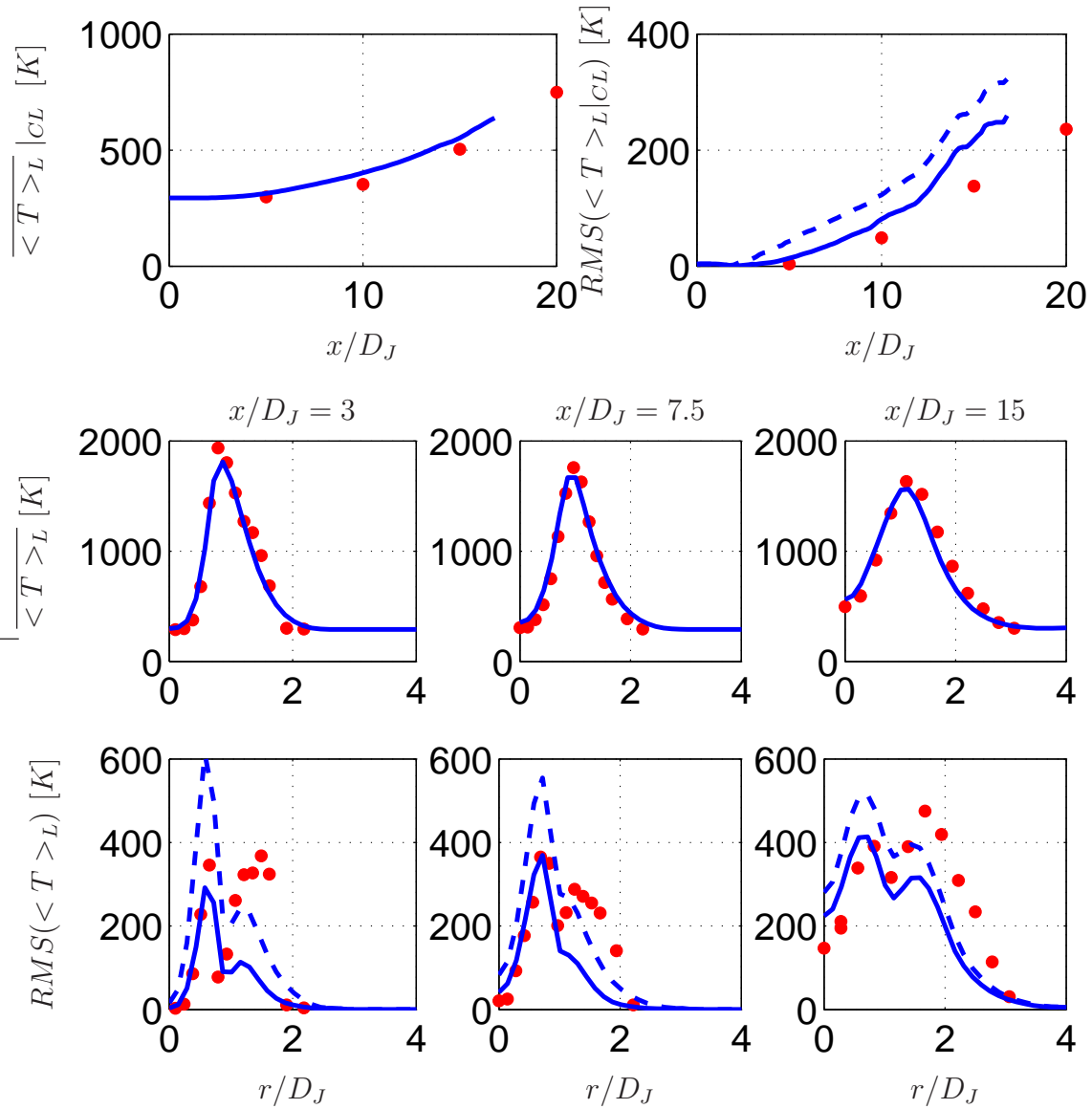


Figure 22: Sandia/TUD: Profiles of the mean and the RMS values of the temperature.

— Resolved LES/SFMDF, - - Total LES/SFMDF, • Sandia experiment.

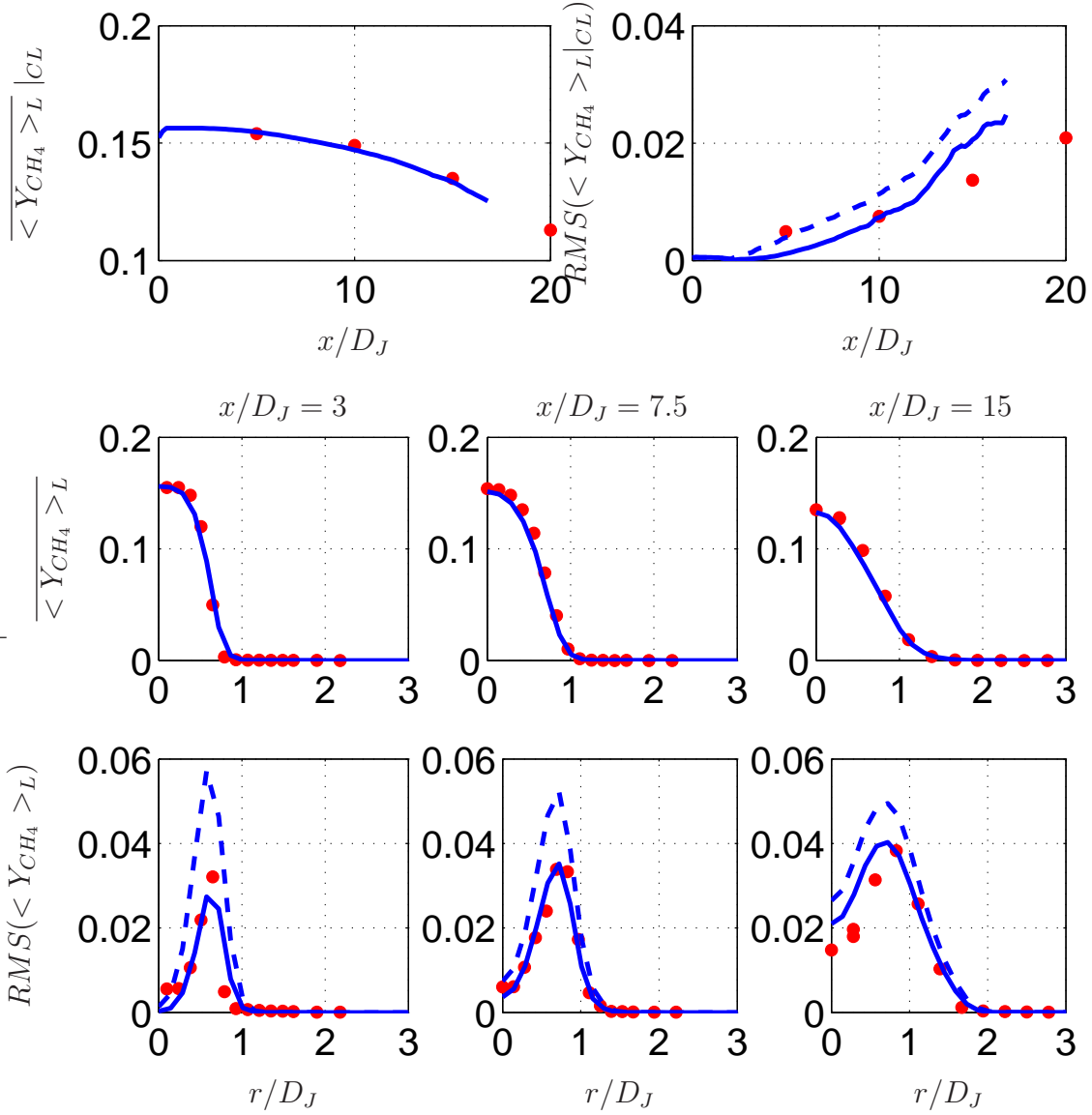


Figure 23: Sandia/TUD: Profiles of the mean and the RMS values of the methane mass fraction. — Resolved LES/SFMDF, - - Total LES/SFMDF, • Sandia experiment.

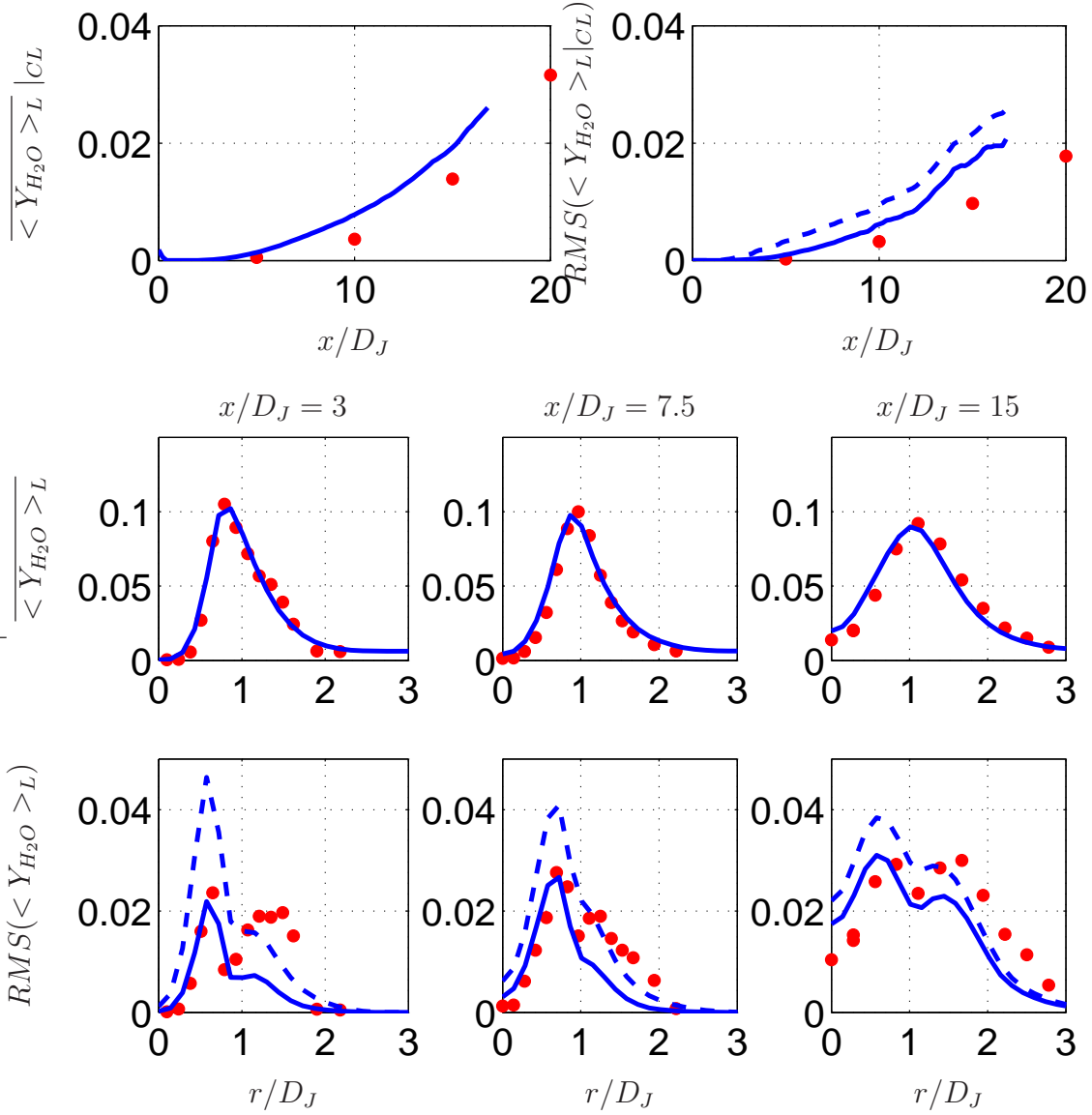


Figure 24: Sandia/TUD: Profiles of the mean and the RMS values of the water mass fraction.

— Resolved LES/SFMDF, - - Total LES/SFMDF, • Sandia experiment.

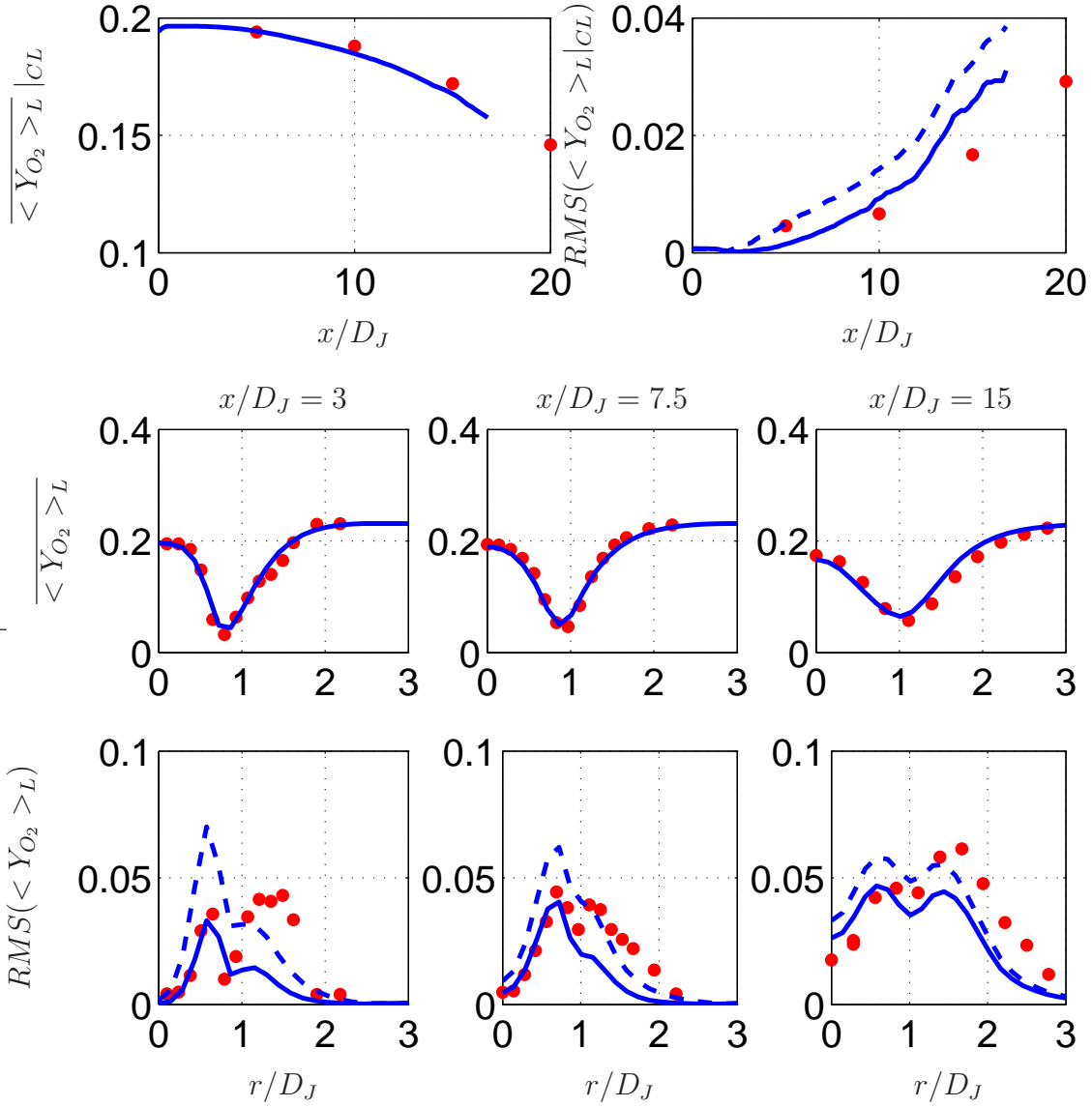


Figure 25: Sandia/TUD: Profiles of the mean and the RMS values of the oxygen mass fraction. — Resolved LES/SFMDF, - - Total LES/SFMDF, • Sandia experiment.

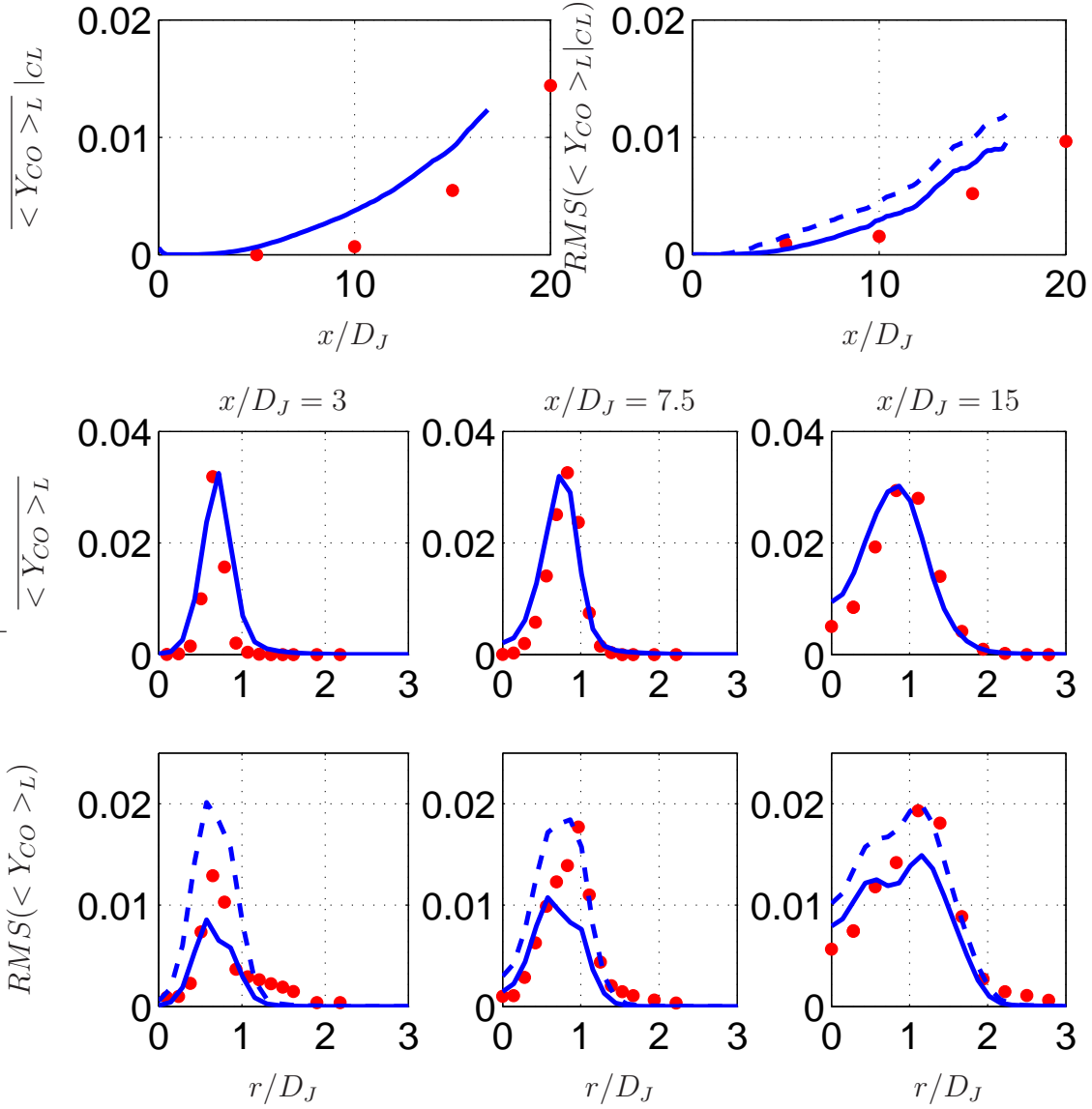


Figure 26: Sandia/TUD: Profiles of the mean and the RMS values of the carbon monoxide mass fraction. — Resolved LES/SFMDf, - - Total LES/SFMDf, • Sandia experiment.

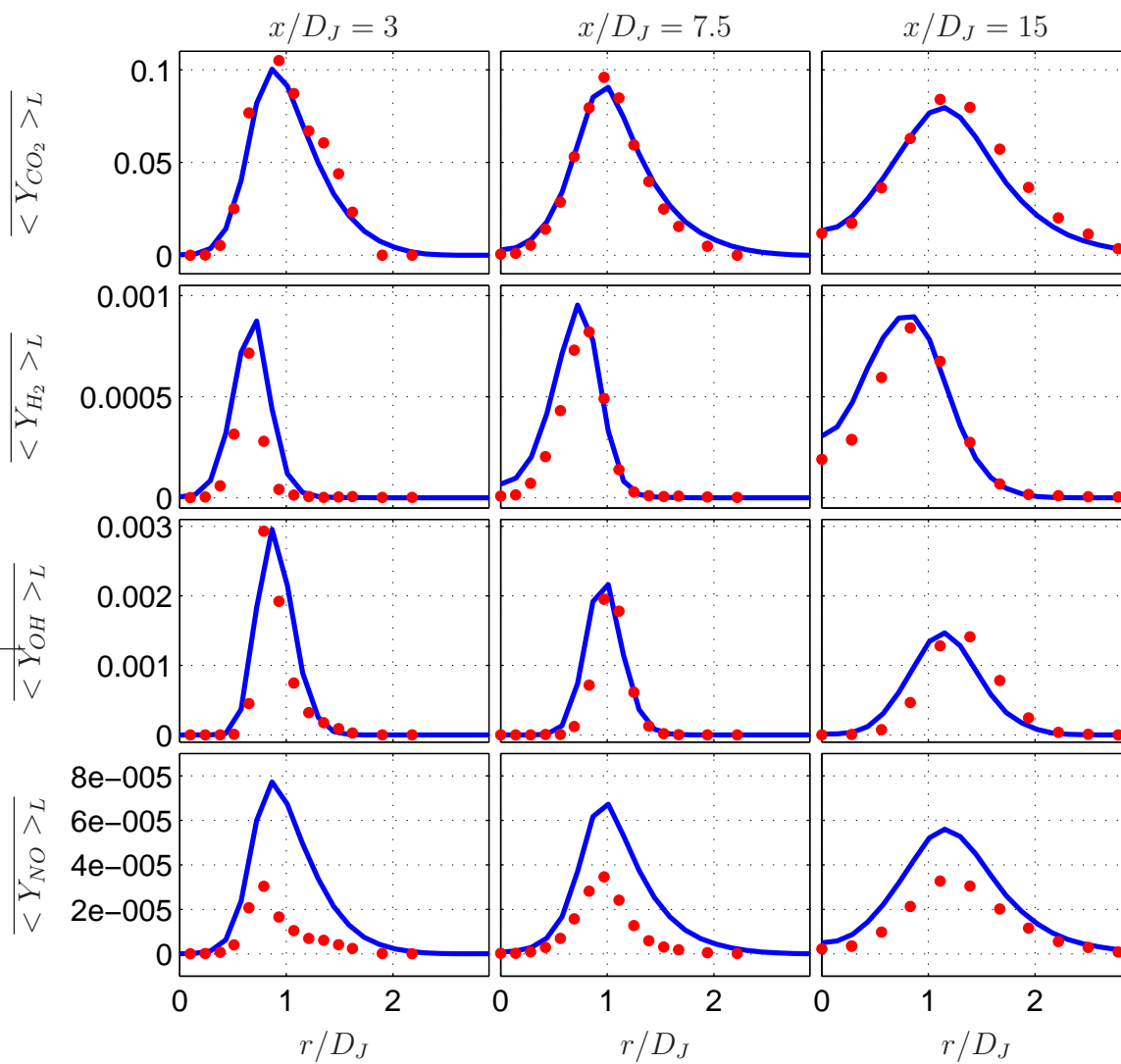


Figure 27: Sandia/TUD: Profiles of the mean values of the selected mass fractions.

— LES/SFMDF, • Sandia experiment.

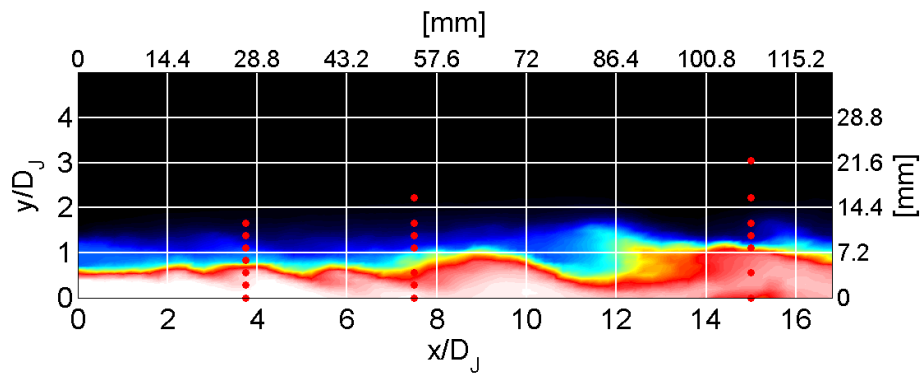
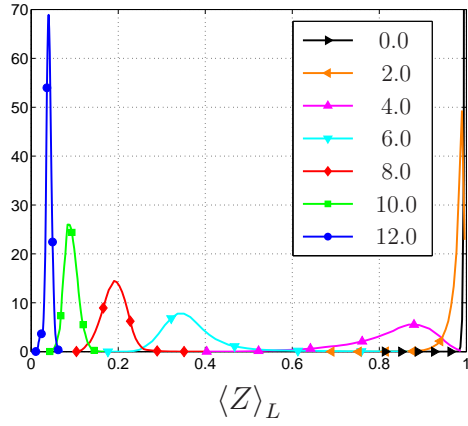
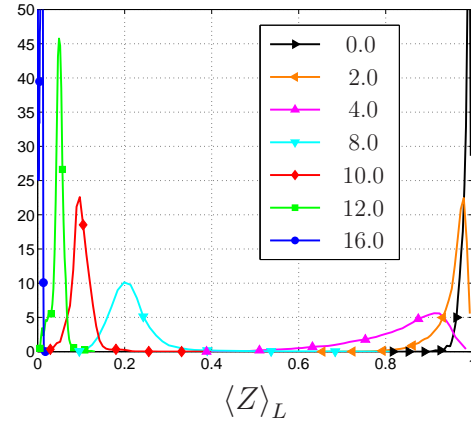


Figure 28: Sandia/TUD: Locations ( $\bullet$ ) where the PDFs are constructed. The experimental data are available at the streamwise locations of  $x/D_J = 7.5$  and  $x/D_J = 15$ .

(a)  $x/D_J = 3.75$



(b)  $x/D_J = 7.5$



(c)  $x/D_J = 15$

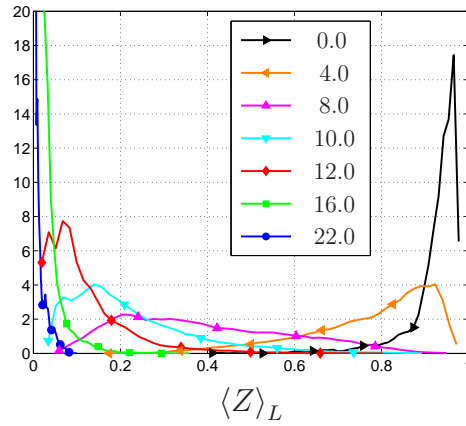
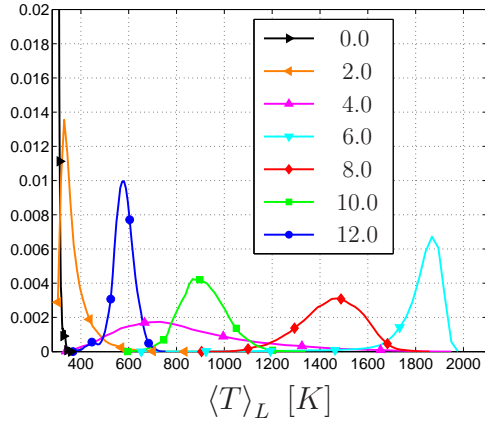
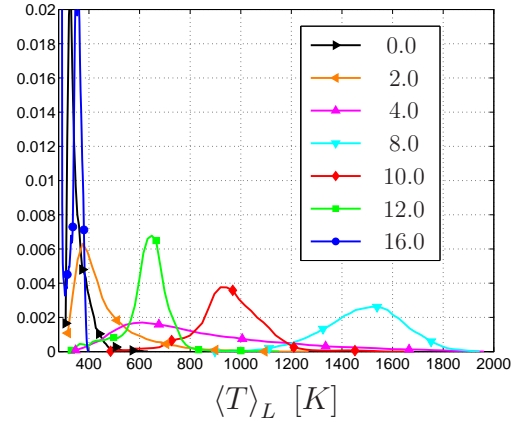


Figure 29: Sandia/TUD: PDFs of the resolved mixture fractions at several streamwise locations. The legends denote the radial ( $r$  [mm]) locations.

(a)  $x/D_J = 3.75$



(b)  $x/D_J = 7.5$



(c)  $x/D_J = 15$

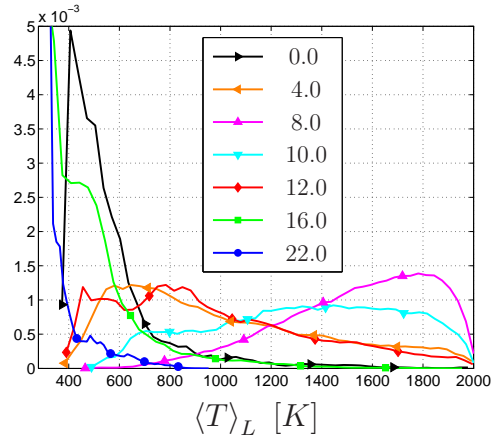


Figure 30: Sandia/TUD: PDFs of the resolved temperature at several streamwise locations. The legends denote the radial ( $r$  [mm]) locations.

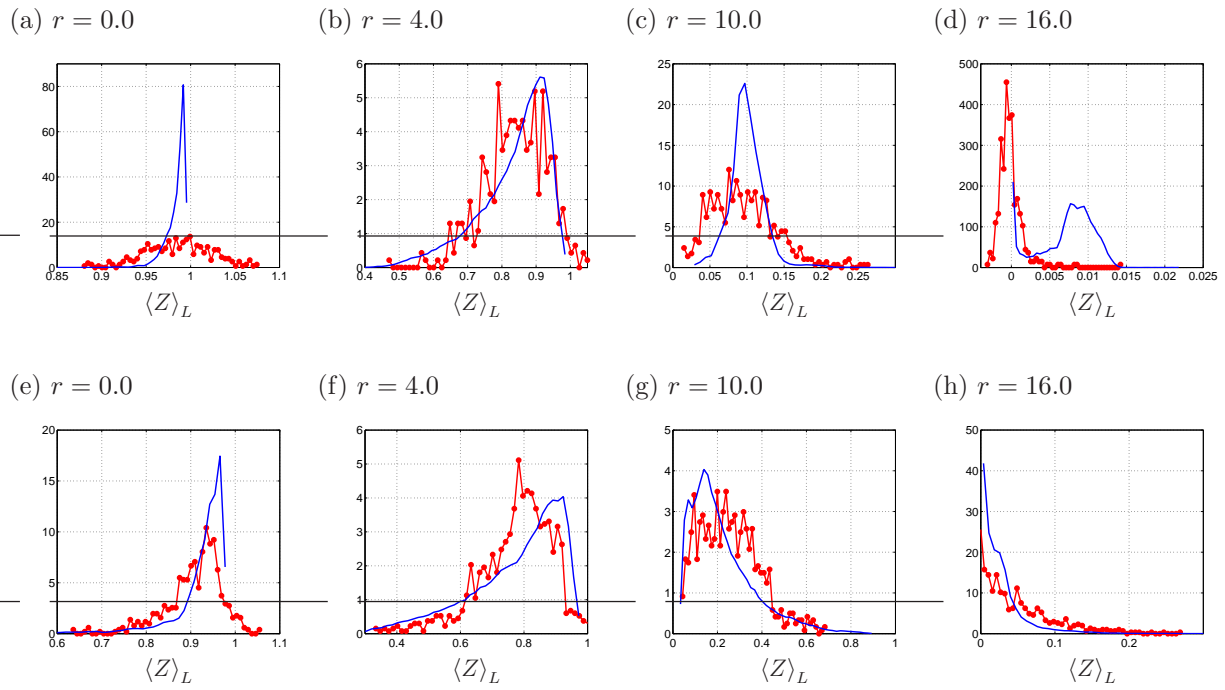


Figure 31: Sandia/TUD: PDFs of the resolved mixture fraction at streamwise locations of  $x/D_J = 7.5$  (top) and  $x/D_J = 15$  (bottom) at selected radial locations ( $r$ [mm], see Figure 28). — LES/SFMDF, —●— Experimental data.

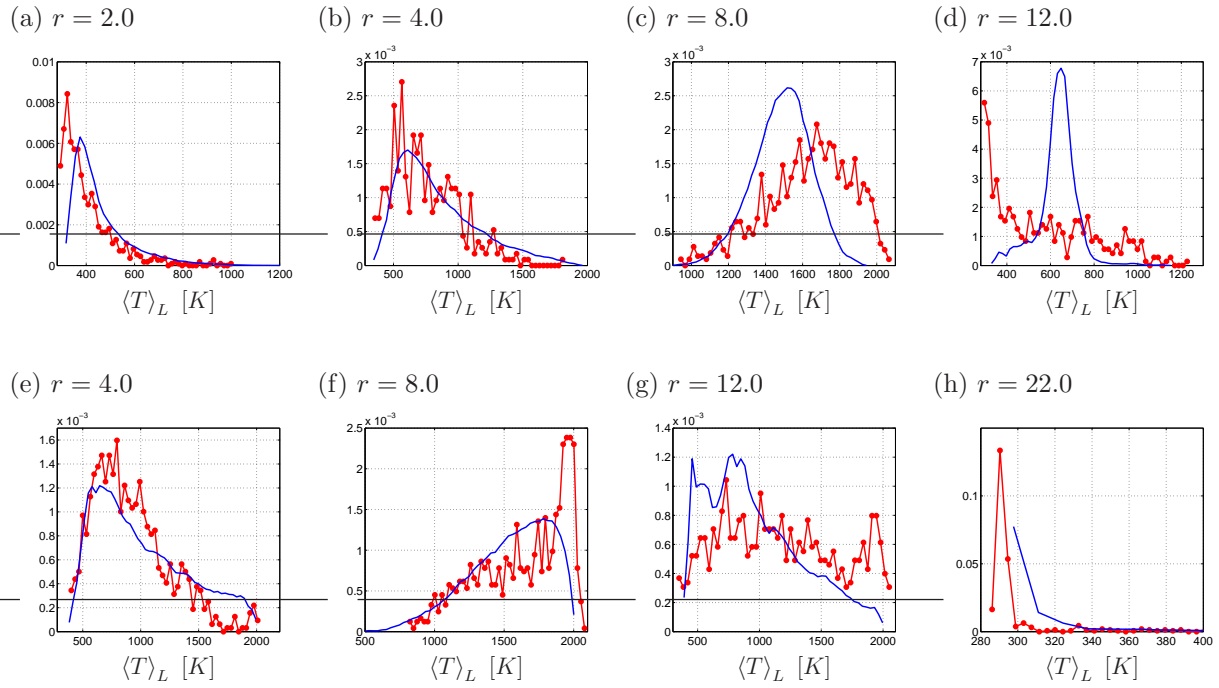


Figure 32: Sandia/TUD: PDFs of the resolved temperature at streamwise locations of  $x/D_J = 7.5$  (top) and  $x/D_J = 15$  (bottom) at selected radial locations ( $r$ [mm], see Figure 28). — LES/SFMDF, —●— Experimental data.

## 3.2 SYDNEY/SANDIA BLUFF-BODY FLAME

### 3.2.1 Configuration

The bluff-body flames have been the subject of extensive investigations.<sup>4-9,109-111</sup> The Sydney/Sandia configurations, considered here, have been studied by Masri *et al.*<sup>4-6</sup> and Dally *et al.*<sup>7-9</sup> Their data are available online.<sup>10,11</sup> The bluff-body flames are stabilized by complex recirculation zones next to the bluff-body surface that are characteristic of practical combustors. Moreover, the boundary conditions are simple and well defined, providing a convenient benchmark to study the turbulence-chemistry interactions. In the experiments, several geometries, flow configurations, and fuels are considered. The schematic representation of these flames is shown in Fig. 33. The central round fuel jet is surrounded by a round bluff-body and air coflow. The jet diameter,  $D_J=3.6\text{ mm}$  and the bluff-body diameter,  $D_B=50\text{ mm}$ . The recirculation zone immediately follows the bluff-body surface. Downstream of the recirculation zone, there is a neck zone which provides a controlled region where the turbulent mixing rate is significant and flame blow-off (extinction) can occur.<sup>9</sup> Further downstream, the flame exhibits a jet like behavior. The most complete set of experimental measurements, consisting of both hydrodynamic and scalar field data for both non-reacting and the reacting cases, have been compiled for the hydrogen-methane flames. For a given geometry and fuel, the non-reacting cases are distinguished by their corresponding bulk jet velocities,  $U_J$ , while the reacting flames are distinguished by their blow-off parameter. The recirculation zones differ in length from  $\sim 1.0D_B$  for the non-reacting cases to  $\sim 1.6D_B$  for the reacting cases. The lengthening is caused by the density stratification within the reaction zone. All cases exhibit a double counter-rotating vortex structure which controls flow and mixing in the recirculation zone. The inner vortex is adjacent the fuel stream and the outer vortex lies between the inner vortex and the coflow. Three complex mixing layers develop between the coflow and the outer vortex, the outer and inner vortices, and the inner vortex and the jet. The flames are stabilized by the hot products circulated toward the bluff-body surface by the middle mixing layer of the counter-rotating vortices. These products provide a continuing ignition source. At large jet velocities, the inner vortex

breaks down causing a portion of the air stream that would be otherwise heated, mixed and convected towards the bluff-body by the counter-rotating motion of both vortices, to be transported downstream.

The non-reacting cases considered here are characterized by the bulk jet velocities of 50, 61, 85, and 143  $m/s$  and the coflow velocity,  $U_{CO}$ , of 20  $m/s$ . Air is used for both the fuel and coflow streams for  $U_J = 61 m/s$ . This case provides data for hydrodynamics validation. The remaining three cases consider CNG<sup>‡</sup> and air for the fuel and coflow streams, respectively.

The reacting case considered is characterized by the Reynolds number of 15,800 based on fuel jet diameter and bulk jet velocity. The bulk jet and the coflow velocities are 118  $m/s$  and 40  $m/s$ , respectively. This corresponds to the conditions at 50% blow-off. The flame's 100% blow-off velocity is  $U_{BO}=235 m/s$ . In the experiments, the blow-off parameter increases from 50% to 75% to 91% increasing the localized extinction in the neck zone, and changing the structure of the recirculation zone. In this work, the lower level of flame blow-off is selected to allow for more accurate representation of chemical reaction via the flamelet chemistry model. The objective is to further assess the predictive capability of the LES/SFMDF in capturing the essential flow field characteristics. The jet is maintained at a temperature of 298 K and is composed of 50% hydrogen ( $H_2$ ) and 50% methane ( $CH_4$ ) by volume.<sup>8</sup> The dilution of hydrogen in methane reduces the formation of soot. The coflow is maintained at about room the temperature and is composed of air. The bluff-body is a ceramic surface that heats up to an average of 1003 K during operation. Hossain *et al.*<sup>55</sup> showed that the effects of the radiative heat transfer on the temperature and other major species are small. However, the inclusion of radiation heat transfer significantly improves the predictions of the hydroxyl radical.<sup>56</sup> The stoichiometric value of the mixture fraction is  $Z_s = 0.05$ .

The bluff-body flames as described here have been the subject of broad previous investigations via other computational and modeling methodologies.<sup>9,50-58</sup>

---

<sup>‡</sup>CNG is typically composed of 90% methane, with the remaining fraction made up of butane and other hydrocarbons.

Table 2: Sydney/Sandia: Summary of the LES/SFMDF parameters and reference quantities.

Parameter	Description	Value
$C_I$	MKEV/Smagorinsky model parameter	0.0/0.0
$C_R$	MKEV model parameter	0.026
$C_S$	Smagorinsky model parameter	0.2
$C_\Omega$	SGS mixing frequency	4
$Le$	Lewis number	1
$Pr$	Prandtl number	1
$Sc$	Schmidt number	1
$Sc_t$	SGS Schmidt number	1
$t_{ref}$ [s]	Reference time	$3.05 \times 10^{-5}$
$T_{ref}$ [K]	Reference temperature	283

### 3.2.2 Numerical Specifications

The values of the flow variables at the inlet are set to those available from the experiments, including the velocity, turbulent intensity, and the mixture fraction. The flow is excited by superimposing oscillating axisymmetric and helical perturbations onto the velocity profile at the inlet. This procedure is similar to that of Danaila and Boersma,<sup>108</sup> with the amplitude of the forcing adjusted to match the experimentally obtained turbulent intensity of the streamwise velocity at the inlet. The key simulation parameters are presented in Table 2. The simulations are conducted on a 3D Cartesian mesh with uniformly spaced grid points. The computational domain spans a region of  $30D_J \times 22.5D_J \times 22.5D_J$  in the streamwise ( $x$ ), and the two lateral ( $y, z$ ) directions, respectively. The number of grid points is  $101 \times 151 \times 151$  in the  $x, y$ , and  $z$  directions, respectively. The filter size is set equal to  $\Delta_L = 2(\Delta x \Delta y \Delta z)^{1/3}$ , where the  $\Delta x$ ,  $\Delta y$ , and  $\Delta z$  are the grid spacing corresponding directions. The size of the ensemble domain in the MC simulation is set equal to the filter size. There are approximately 40 particles in each ensemble domain. Per results of extensive previous studies<sup>12,30,33,44</sup> this

number is sufficient to yield an excellent statistical accuracy with minimal dispersive errors. In total, there are about 6.8 million MC particles within the computational domain at all times. The simulation results are monitored to ensure that the particles fully encompass and extend well beyond the regions of non-zero vorticity and reaction. First, the consistency and the accuracy of the simulations are assessed. Next, the predicative capability of the LES/SFMDF is demonstrated by comparing the results with the experimental data. The statistics are obtained by long-time averaging of the Favré filtered fields during several flow through times. The collection of the data is initialized after the flow has swept the domain during the initial four flow through times. The PDFs are constructed based on the LES/SFMDF data resolved at the FD grid points residing within a circular band of width  $\Delta$ . The center of each band is located at a radial location where experimental data are available. The notations  $\overline{Q}$  and  $RMS(Q)$  denote the time-averaged mean and root mean square values of the variable  $Q$ , respectively. The radial ( $r = \sqrt{y^2 + z^2}$ ) profiles of the streamwise velocity at the inlet are compared with the experimental data in Figure 34. The parameter  $R_B$  denotes the radius of the bluff-body. The RMS of the velocity components on the bluff-body surface are set, such that the flow is properly excited at  $x/D_B = 0.3$ . This, or similar, approximation is appropriate when no attempt is made to resolve the near wall region, and the flow is dominated by large recirculation zones.<sup>51</sup>

The flamelet table with a constant strain rate of  $\chi = 100$  1/s is used to relate the thermo-chemical variables to the mixture fraction. The choice of the strain rate is consistent with previous studies of bluff-body flames<sup>52</sup> and experimental assessments.<sup>8</sup> Figure 35 shows the comparison of the flamelet tables for several thermo-chemical variables with the experimental data. The temperature, oxygen ( $O_2$ ) and hydrogen ( $H_2$ ) mass fractions are well represented. However, the carbon dioxide ( $CO_2$ ) and carbon monoxide ( $CO$ ) are underpredicted, while water and hydroxyl radical ( $OH$ ) are overpredicted. Although, a complex chemical mechanism for hydrocarbon combustion (GRI mechanism<sup>63,64</sup>) is used to generate the flamelet table, modifications may be needed in applications to turbulent flames.<sup>56,112</sup>

The computational costs associated with LES/SFMDF depends, obviously, on the parameters of the simulations. For the case reported here, the simulations required about

540 hours of CPU time on a SGI Altix with 6 processors. This includes the times required for consistency tests and ensemble averaging of data. The computational time for LES without including SGS effects<sup>30</sup> is about 10-12 times less. However such simulations yield erroneous predictions and in many cases lead to numerical instabilities. For further comparative assessment of the computational requirements of the FDF in comparison to non-FDF methods, we refer to previous work.<sup>12,30,33,44</sup>

### 3.2.3 Comparisons with Experimental Data

Tables 3 and 4 show the specifications of the experiments and simulation data, respectively. The experimental flow fields of the reacting cases HM1E-S(1-2) considered at Sydney are meant to represent the same flame conditions as the HM1 experiments considered at Sandia. However, the wind tunnel in Sydney did not provide the same exact hydrodynamic conditions. The streamwise velocities are  $U_J = 118\text{m/s}$  and  $U_C = 40\text{m/s}$  in the HM1, but  $U_J = 108\text{m/s}$  and  $U_C = 35\text{m/s}$  in the HM1E-S experiments. The new jet and coflow velocities were chosen such that the HM1 and HM1E-S flames are equally proportional (within 50% blow-off) from their corresponding blow-off velocities. To facilitate comparisons of the flow statistics of the HM1E-S data with those of HM1 and LES/SFMDF, the former's values of the streamwise velocity are scaled by a ratio of the bulk jet velocities; that is 118/108.

The consistency of the LES/SFMDF results is briefly assessed by examining the instantaneous and the time averaged contours of the mixture fraction (Fig. 36). The similarity of the results in the instantaneous figures is observed at all other times. The time averaged values also indicate good agreementS between the FD and the MC.

**3.2.3.1 Non-Reacting Flows.** The non-reacting experiments, B4C1-S(1-3), consider air at both the fuel and coflow streams. The bulk streamwise velocity of 61 m/s and the coflow streamwise velocity of 20 m/s are considered. The simulations are conducted with both the MKEV and the conventional Smagorinsky models. No LES/SFMDF simulations are conducted for these flows. Therefore, only the values of the scalar field statistics resolved

Table 3: Sydney/Sandia: Experimental specifications.<sup>11</sup>

Label	Fuel(Ratio <sup>†</sup> )	$U_J$ <sup>‡</sup>	$U_{CO}$ <sup>‡</sup>	Available data	Year
B4C1-S1	Air	61	20	$\bar{U}, \bar{V},$ $RMS(U), RMS(V)$	1995
B4C1-S2	Air	61	20	$\bar{U}, \bar{V}, RMS(U),$ $RMS(V), RMS(UV)$	12/01/1999
B4C1-S3	Air	61	20	$\bar{U}, \bar{V}, RMS(U)$ $RMS(V), RMS(UV)$	12/15/1999
B4C2-50	CNG	50	20	$\bar{Z}, RMS(Z)$	
B4C2-85	CNG	85	20	$\bar{Z}, RMS(Z)$	
B4C2-143	CNG	143	20	$\bar{Z}, RMS(Z)$	
HM1	$H_2 : CNG$ (1 : 1)	118	40	$\bar{U}, \bar{V},$ $RMS(U), RMS(V)$	1995
HM1	$H_2 : CH_4$ (1 : 1)	118	40	$\bar{Z}, \bar{T}, \bar{Y}_\alpha$ <sup>§</sup> , $RMS(Z),$ $RMS(T), RMS(Y_\alpha),$ PDFs	1995
HM1E-S1	$H_2 : CNG$ (1 : 1)	108	35	$\bar{U}, \bar{V}, RMS(U),$ $RMS(V), RMS(UV)$	01/21/2000
HM1E-S2	$H_2 : CNG$ (1 : 1)	108	35	$\bar{U}, \bar{V}, RMS(U),$ $RMS(V), RMS(UV)$	02/11/2000

<sup>†</sup>Volumetric.

<sup>‡</sup>[m/s]

<sup>§</sup> $O_2, N_2, H_2, H_2O, CO, CO_2, OH, NO$

Table 4: Sydney/Sandia: Simulation specifications.

Label	Fuel(Ratio <sup>†</sup> )	$U_J$ <sup>‡</sup>	$U_{CO}$ <sup>‡</sup>	Re <sup>§</sup>	$\nu_{ref}$ [ $m^2/s$ ] <sup>¶</sup>	SGS model
MKEV	Air	61	20	13,899	$1.58 \times 10^{-5}$	MKEV
SMAG	Air	61	20	13,899	$1.58 \times 10^{-5}$	Smagorinsky
LES-50	$CH_4$	50	20	10,580	$1.7013 \times 10^{-5}$	MKEV
LES-85	$CH_4$	85	20	17,987	$1.7013 \times 10^{-5}$	MKEV
LES-143	$CH_4$	143	20	30,260	$1.7013 \times 10^{-5}$	MKEV
LES/SFMDF	$H_2 : CH_4$ (1 : 1)	118	40	15,800	$2.6886 \times 10^{-5}$ <sup>  </sup>	MKEV

<sup>†</sup>Volumetric.

<sup>‡</sup>[m/s]

<sup>§</sup>Reynolds number based on  $D_J$  and  $U_J$

<sup>¶</sup>Kinematic viscosity at standard conditions. <sup>113</sup>

<sup>||</sup>Value yields Re number reported for the reacting bluff-body experiments at 50% blow-off.

by the LES are considered. The recirculation zone with the double vortex structures captured by the experiments and LES are shown via the time averaged streamwise velocity contours with superimposed streamlines and velocity vectors in Fig. 37. Both of the SGS models capture the two recirculation zones well. The length of the recirculation region behind the bluff-body surface is slightly overpredicted. The counter-rotating vortices are also predicted slightly further downstream of their experimentally reported counterparts. The instantaneous snapshots of the streamwise velocity, streamlines, and velocity vectors are shown in Fig. 38. The radial profiles of the mean and the RMS values of the streamwise velocity are shown in Figs. 39, and those of the radial velocity are shown in Fig. 40 for several downstream locations. Both the mean and the RMS values compare well with the experiments.

The non-reacting experiments, B4C2, consider a “cold” methane fuel stream with the bulk streamwise velocities of 50, 85, and 143  $m/s$ , and the air coflow stream with the streamwise velocity of 20  $m/s$ . Only the mixture fraction statistics are measured in these

experiments. The time averaged streamwise velocity with superimposed streamlines and velocity vectors are shown in Fig. 41. As observed previously, a set of two counter-rotating vortices forms behind the bluff-body surface. The recirculation region shortens as the fuel stream velocity increases. In addition, the two vortices reposition themselves with the inner vortex shifting downstream with respect to the outer one. The shift is accompanied by a loss in inner vortex’s circulation strength that becomes most noticeable in LES-143. In the latter case the jet’s large streamwise velocity causes the inner vortex to partially break down. The instantaneous and the time averaged 3D contours of the mixture fraction are shown in Fig. 42. Different mixing structures are observed in the instantaneous values as the streamwise velocity of the fuel stream increases. The time averaged plots accentuate the shortening of the recirculation zone. This is highlighted by the “cone” of the mixture fraction iso-surface of 0.06. Figures 43 and 44 show the radial profiles of the mean and the RMS values of the mixture fraction at several downstream locations. The general agreement of the mean values is satisfactory with the largest discrepancy occurring near the centerline for the case with the lowest streamwise velocity (LES-50). The RMS values are also predicted well with the discrepancies occurring on the oxidizer side of the bluff-body surface and near the centerline farthest downstream of the inlet. The general trends are also captured by the simulations. For example, at the centerline, the value of the mixture fraction mean is the lowest for the LES-50 case but downstream of the bluff-body surface this value is the largest for the same case. Also downstream of the bluff-body surface, the RMS values are the lowest for the LES-143 followed by LES-50 and LES-85. Both trends are present in the experiments. The correct representation of such trends in the simulations suggests a successful capture of important mixing structures.

**3.2.3.2 Reacting Flows.** The capability of the LES/SFMDF to predict the reacting flow field is demonstrated here. The time averaged streamwise velocity contours with the streamlines and velocity vectors superimposed are shown in Fig. 45. This figure shows the recirculation region and the two characteristic counter-rotating vortices. The recirculating zones are well captured by the simulations. However, there are a few discrepancies that are manifested by the relative position of the inner and outer vortices. In the HM1 experiment,

as well as in the simulation, the inner vortex is located behind the outer vortex. However, in the HM1E-S experiments the situation is reversed. The recirculating region extends to about  $\sim 1.6D_B$ , as compared to about  $\sim 1D_B$  in the isothermal cases, due to the density gradient and the heat release. The central jet more easily penetrates the low density region. The mean profiles of the streamwise and the radial velocities at several downstream locations are shown in Figs. 46 and 48, respectively. The corresponding RMS profiles are shown in Fig. 47 and Fig. 49. The comparisons show good overall qualitative agreement with the experimental data. The mean and the RMS values of the streamwise velocity show an excellent agreement with the HM1E-S data. The mean and the RMS values of the radial velocity are underpredicted at downstream locations. The discrepancies may be attributed, at least in part, to the experimental errors in the measurements caused by the spacial resolution effects.<sup>9</sup> The radial profiles of the mean and the RMS values of the mixture fraction are shown in Figs. 50 and 51, respectively. The mean values are in excellent agreement with the experiment, while the total and resolved RMS values are overpredicted in the fuel stream in the recirculation zone. The radial profiles of the mixture fraction RMS exhibit three regions of interest in the recirculation zone ( $x/D_B < 1.6$ ). These regions correspond to the inner, central, and outer mixing layers located at  $r/R_B \approx 0.2, 0.5, 0.9$ , respectively. In the experiments, the downstream RMS values corresponding to the inner and central layers are approximately equal. The RMS value of the central mixing layer increases downstream of the recirculation zone. The LES/SFMDF, however, predicts the RMS value of the inner layer as the largest in the recirculation zone. The RMS values corresponding to the outer mixing layer are slightly overpredicted at all downstream locations.

The radial profiles of the mean and the RMS values of the temperature are shown in Figs. 52 and 53, respectively. The near field mean values compare well with the experimental data. The downstream locations, however, are overpredicted on the oxidizer stream side of the bluff-body. The overprediction can be traced to that of the temperature on the fuel lean side ( $Z < Z_s$ ) of the flamelet table (see Fig. 35). Similar, over-, or under-predictions are present in the species' mean and RMS values (see Appendix ). The mean temperature is the highest in the central mixing layer region where the hot products of combustion are convected toward the bluff-body by the counter-rotating vortical structures. The

experimental temperature RMS values are overpredicted by the total RMS values and are generally well predicted by the resolved RMS values with the exception of the oxidizer stream side of the bluff-body at downstream locations. Similarly to the mixture fraction RMS, the effects of the three mixing layers, generated by the counter-rotating vortical structures, are pronounced at  $x/D_B = 0.8$  and  $r/R_B \approx 0.2, 0.5, 0.9$  by the peaking RMS values of the temperature.

**3.2.3.3 PDF Comparisons.** The PDFs of the resolved scalar fields as predicted by LES/SFMDF are compared with those measured experimentally. Figure 54 shows the locations where the PDFs are constructed. Figures 55 and 56 show the PDFs of the resolved mixture fraction and temperature, respectively. The comparison of the LES/SFMDF results at select radial locations with the experimentally available PDF data is shown in Fig. 57 for the resolved mixture fraction and Fig. 56 for the resolved temperature. The overall agreement between LES/SFMDF and the experiment is very good.

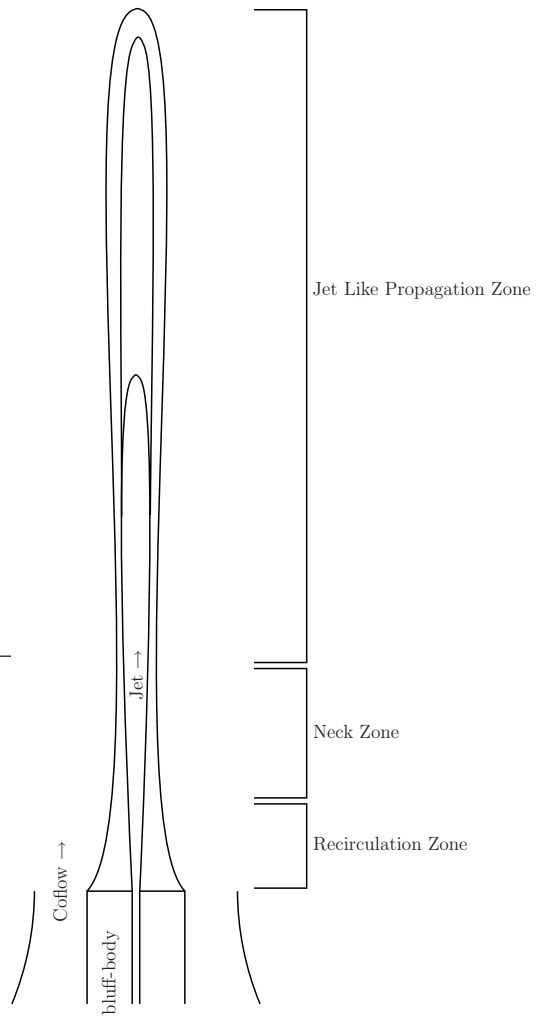


Figure 33: Sydney/Sandia: Flame configuration.

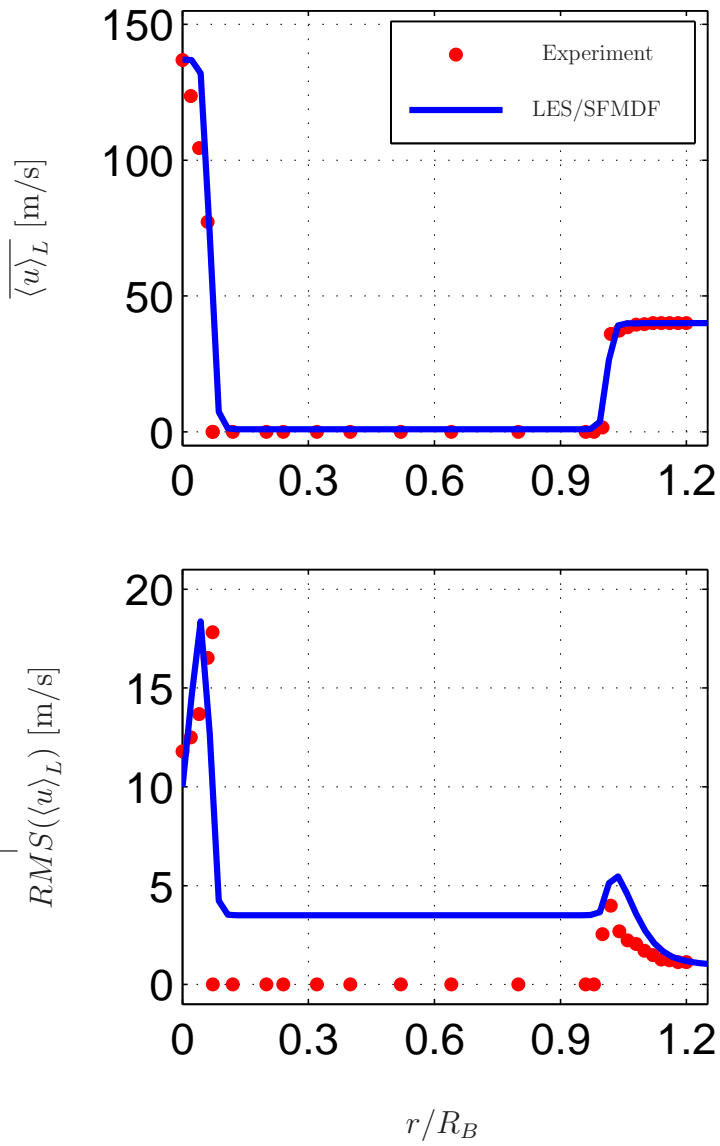


Figure 34: Sydney/Sandia: Radial profiles of the mean and the resolved RMS values of the streamwise velocity at the inlet.

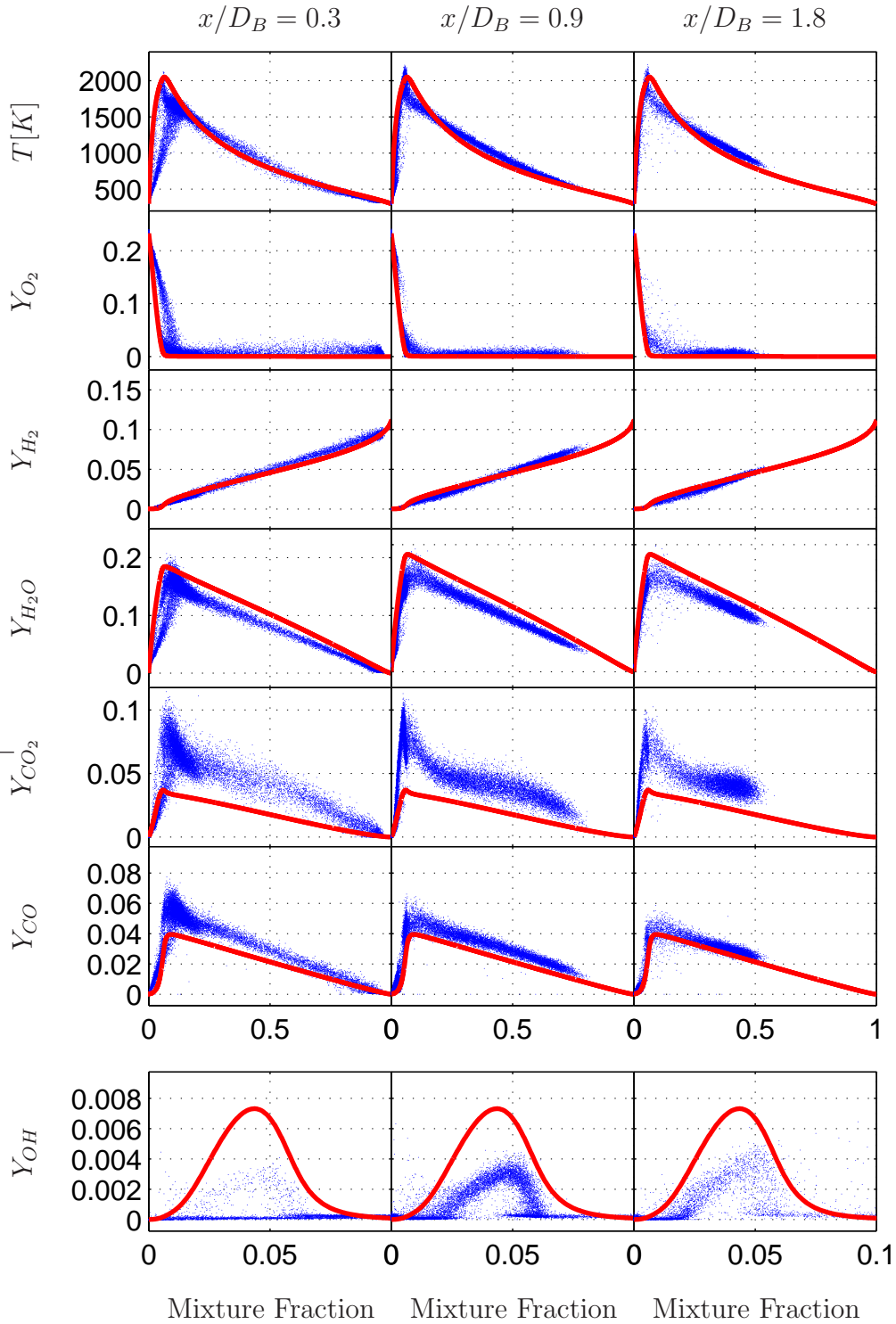


Figure 35: Scalar values versus the mixture fraction as predicted by the flamelet chemistry model and measured experimentally. Dots denote the experimental data, —  $\chi = 100$  1/s.

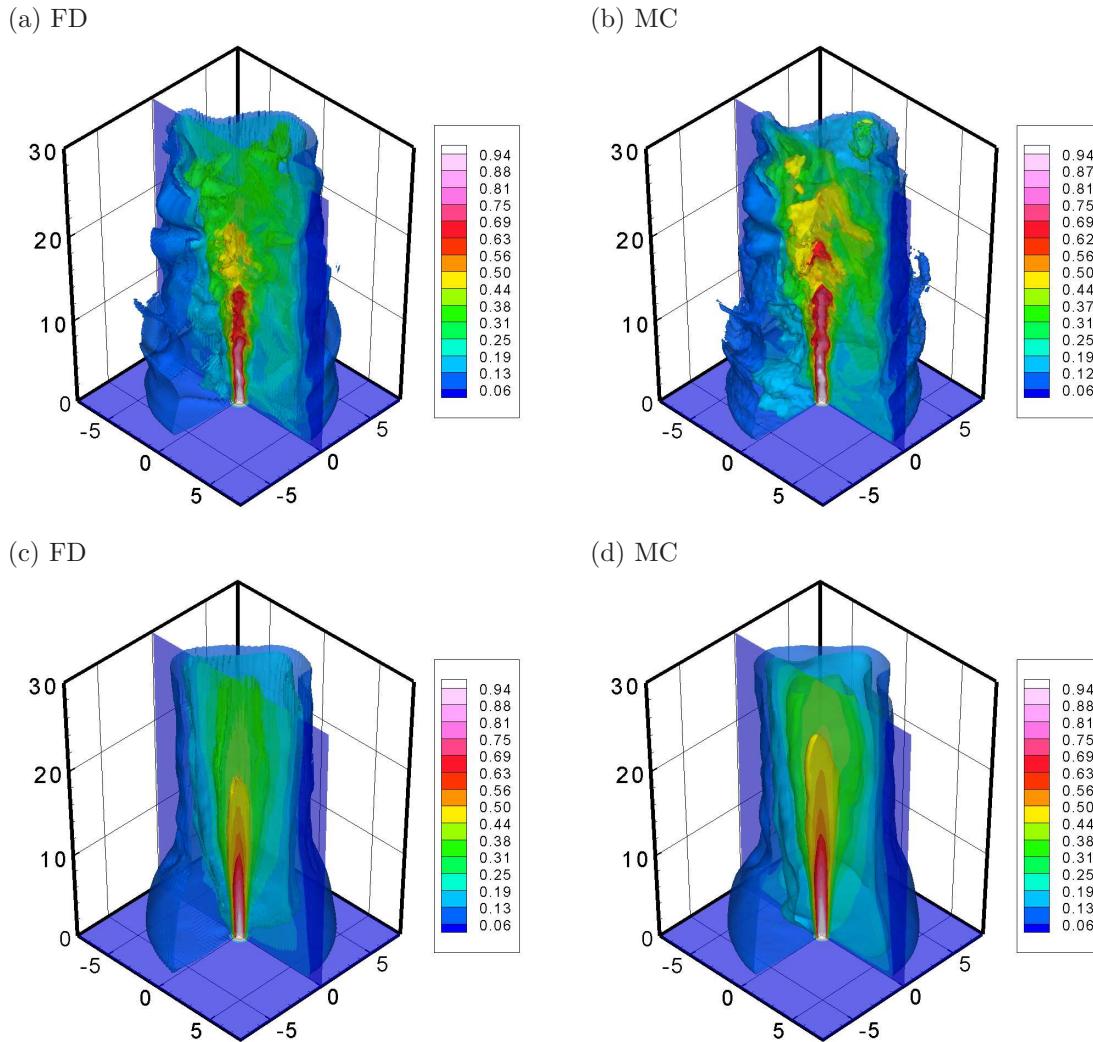


Figure 36: Sydney/Sandia: Comparison of the instantaneous (a, b), and the time averaged (c, d) contours of the mixture fraction. The six iso-surfaces shown are of 0.07 (blue), 0.15, 0.34, 0.45, 0.63, 0.9 (white). The axis are normalized by the diameter of the fuel stream.

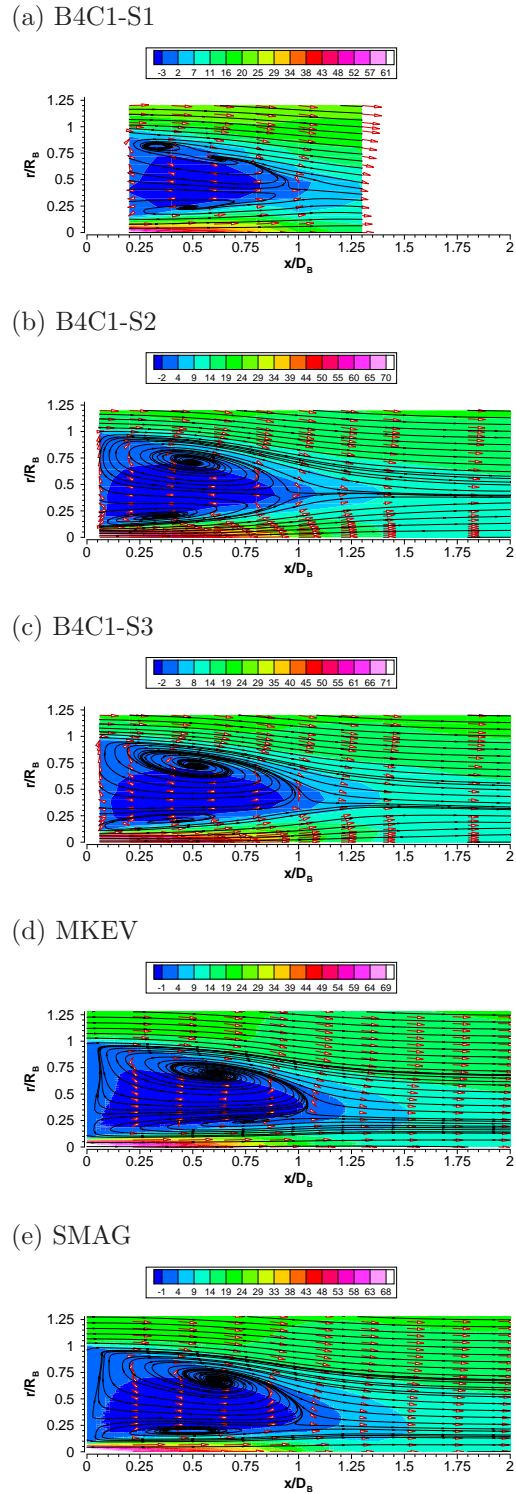
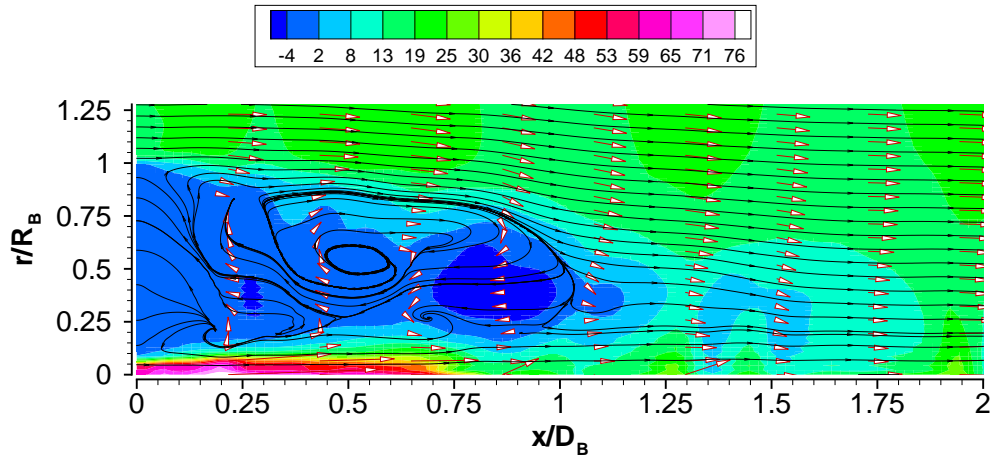


Figure 37: Sydney/Sandia: Time averaged recirculation features as predicted by experiments and LES. The color contours denote the streamwise velocity. Superimposed are the streamlines and the velocity vectors.

(a) MKEV



(b) SMAG

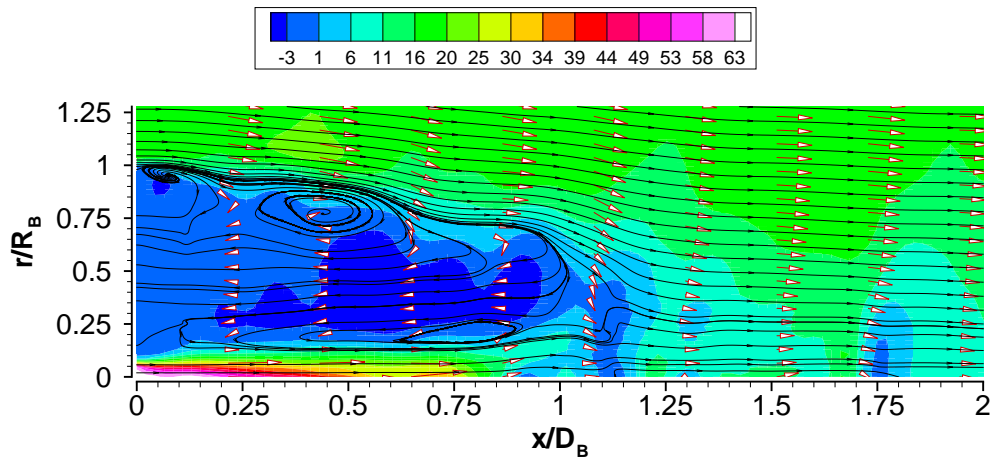


Figure 38: Sydney/Sandia: Instantaneous recirculation features as predicted by the LES. The color contours denote the streamwise velocity. Superimposed are the streamlines and the velocity vectors.

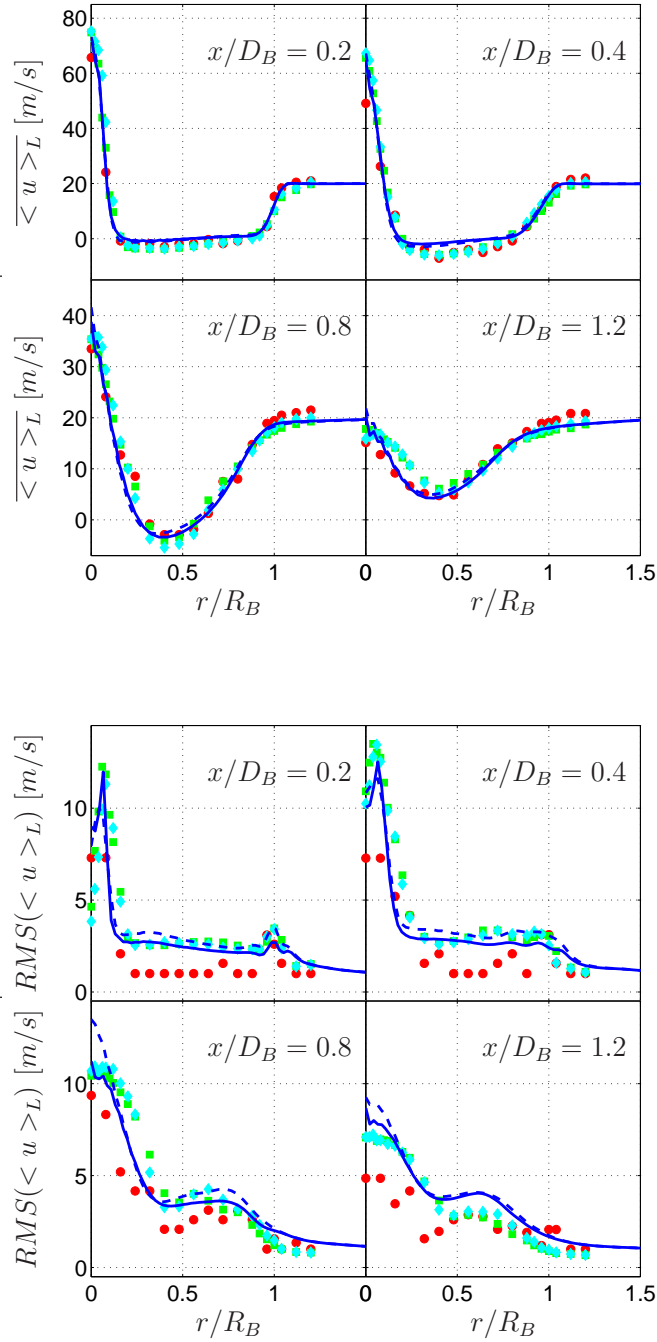


Figure 39: Sydney/Sandia: Radial profiles of the mean and the resolved RMS values of the streamwise velocity for the non-reacting flow. — MKEV, - - SMAG, ● B4C1-S1, ■ B4C1-S2, ◆ B4C1-S3.

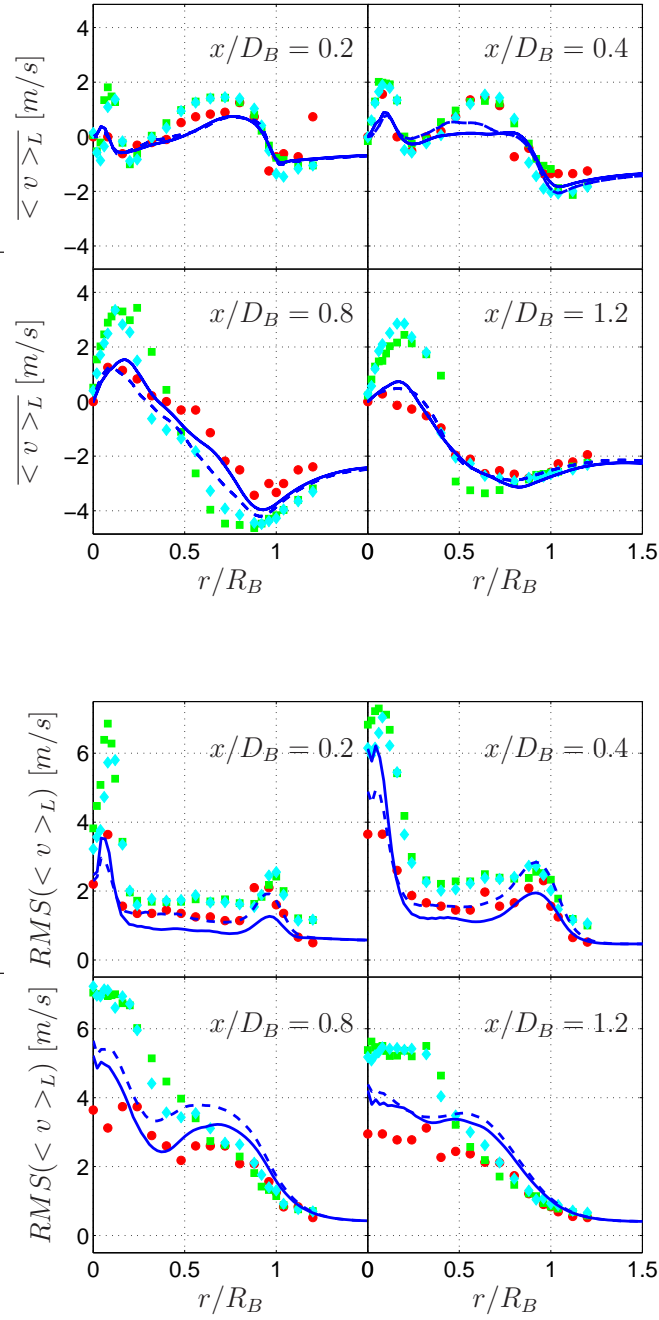
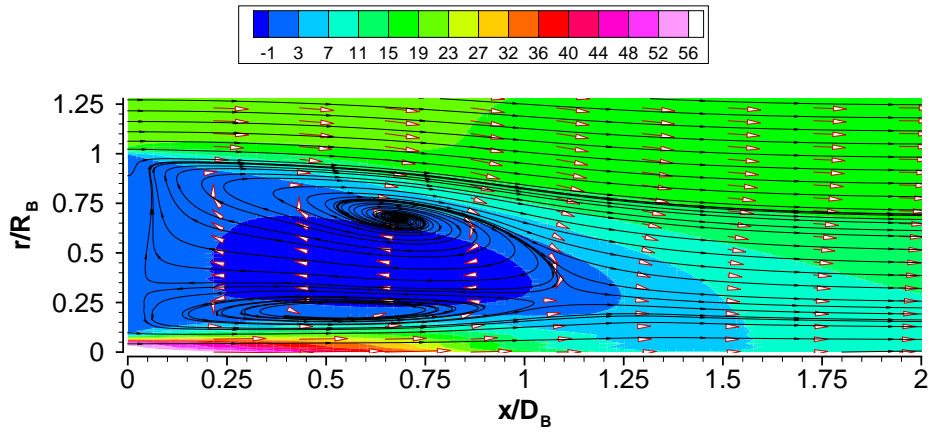
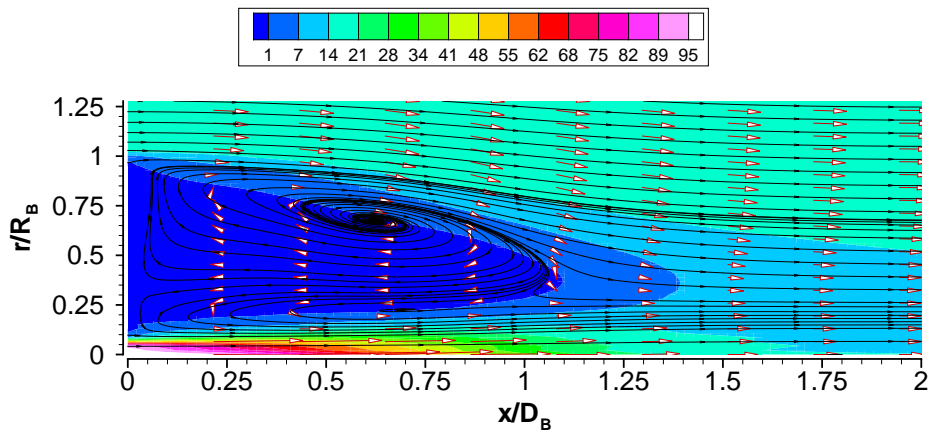


Figure 40: Sydney/Sandia: Radial profiles of the mean and the resolved RMS values of the radial velocity for the non-reacting flow. — MKEV, - - SMAG, ● B4C1-S1, ■ B4C1-S2, ◆ B4C1-S3.

(a) LES-50



(b) LES-85



(c) LES-143

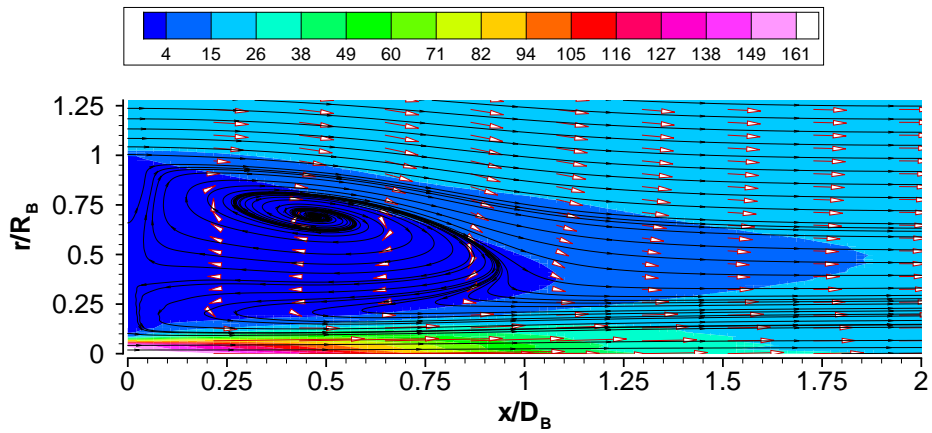


Figure 41: Sydney/Sandia: Time averaged recirculation features as predicted by the LES. The color contours describe the streamwise velocity. Superimposed are the streamlines and the velocity vectors.

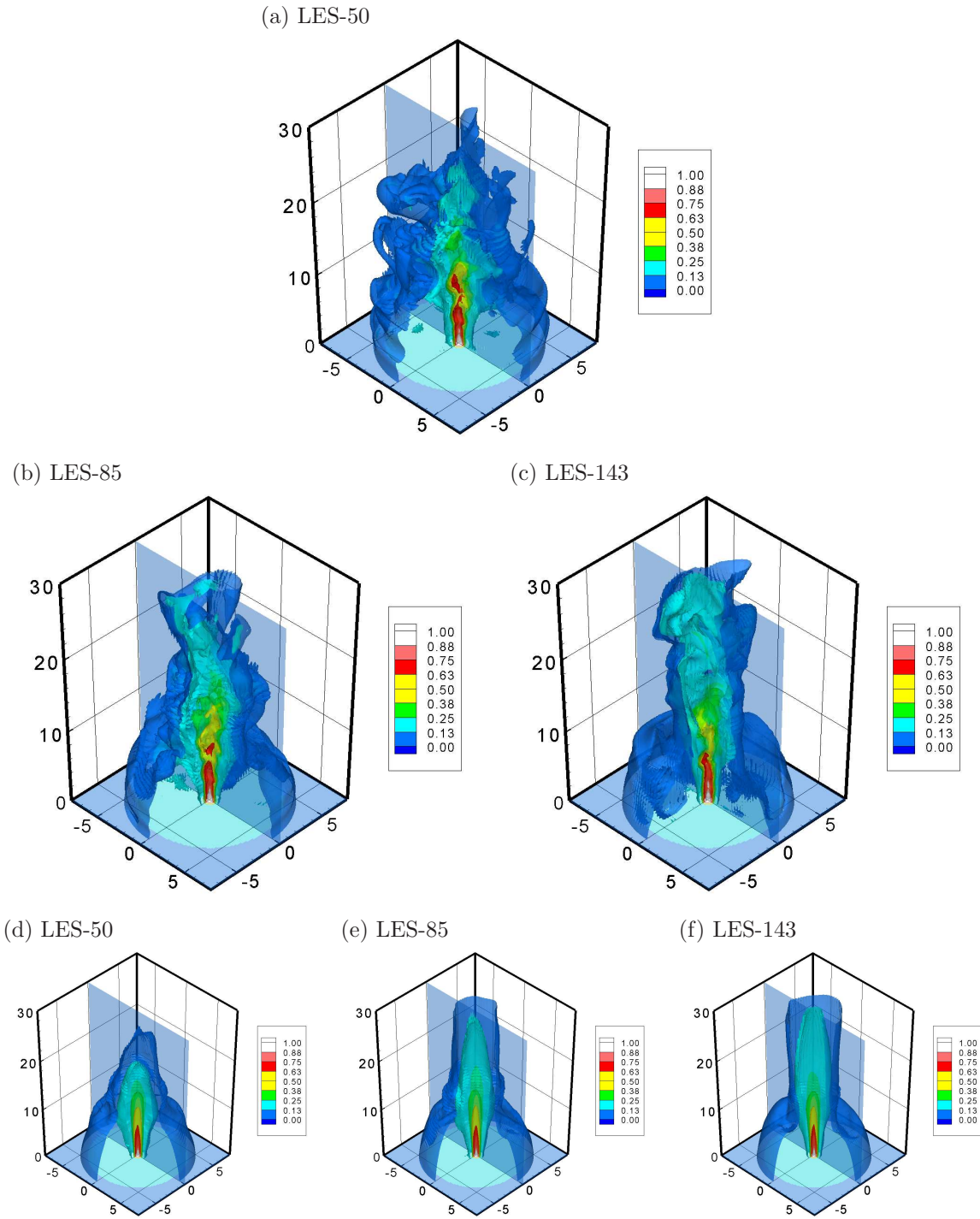


Figure 42: Sydney/Sandia: Instantaneous (a, b, c), and time averaged (d, e, f), contours of the mixture fraction as predicted by the LES of several non-reacting flow configurations. The six iso-surfaces are 0.06 (blue), 0.13, 0.34, 0.45, 0.63, 0.90 (white). The plot's axes are normalized by the diameter of the fuel stream.

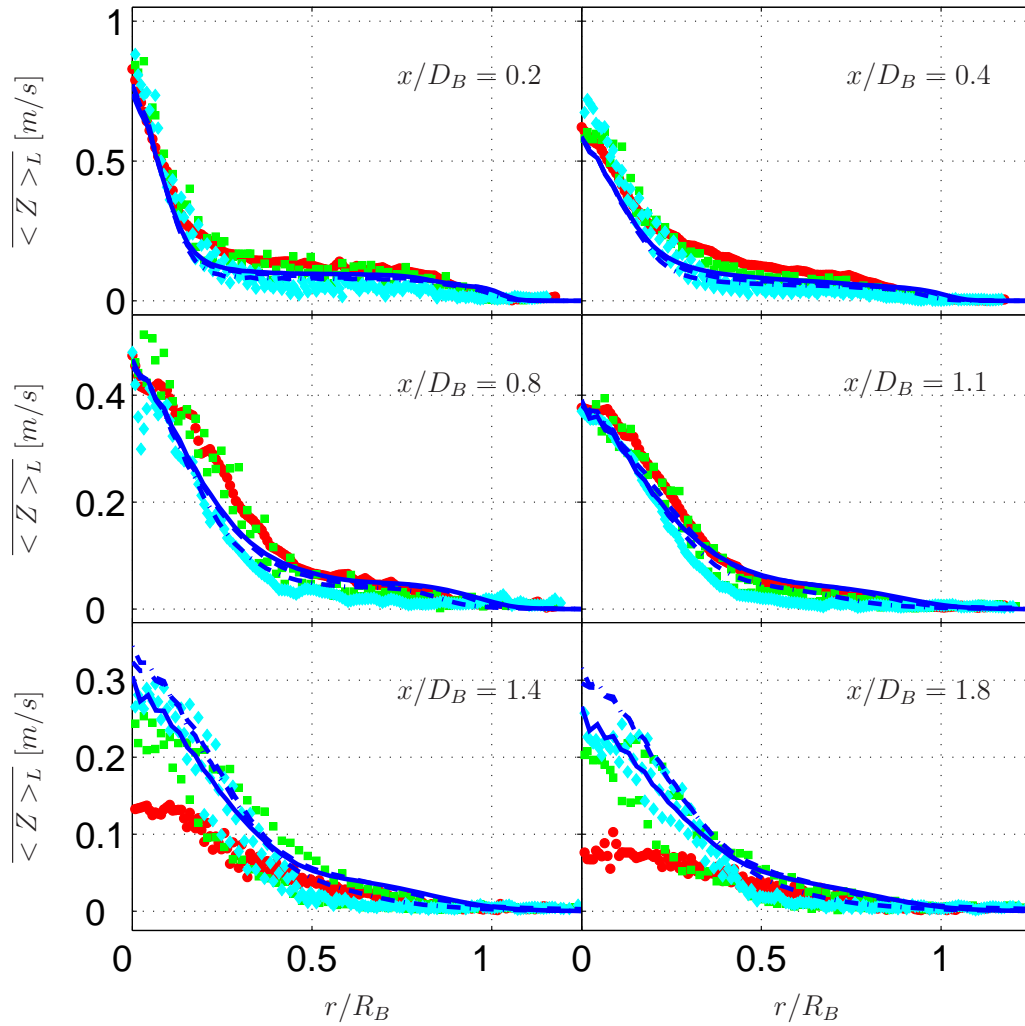


Figure 43: Sydney/Sandia: Radial profiles of the mean values of the mixture fraction as predicted by the LES of several non-reacting flow configurations. — LES-50, - - LES-85, - · - LES-143, ● B4C2-50, ■ B4C2-85, ◆ B4C2-143.

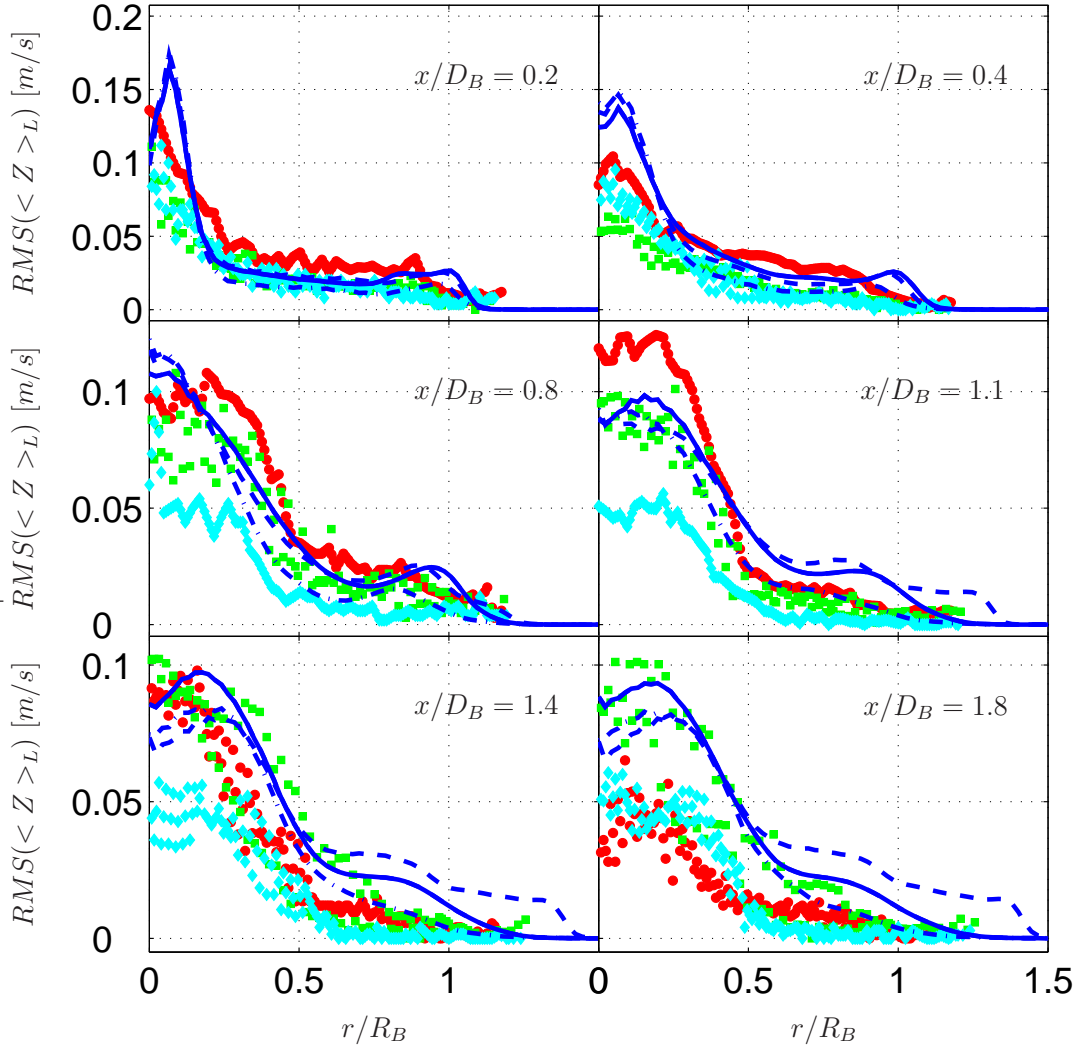


Figure 44: Sydney/Sandia: Radial profiles of the resolved RMS values of the mixture fraction as predicted by the LES of several non-reacting flow configurations. — LES-50, - - LES-85, - · - LES-143, ● B4C2-50, ■ B4C2-85, ◆ B4C2-143.

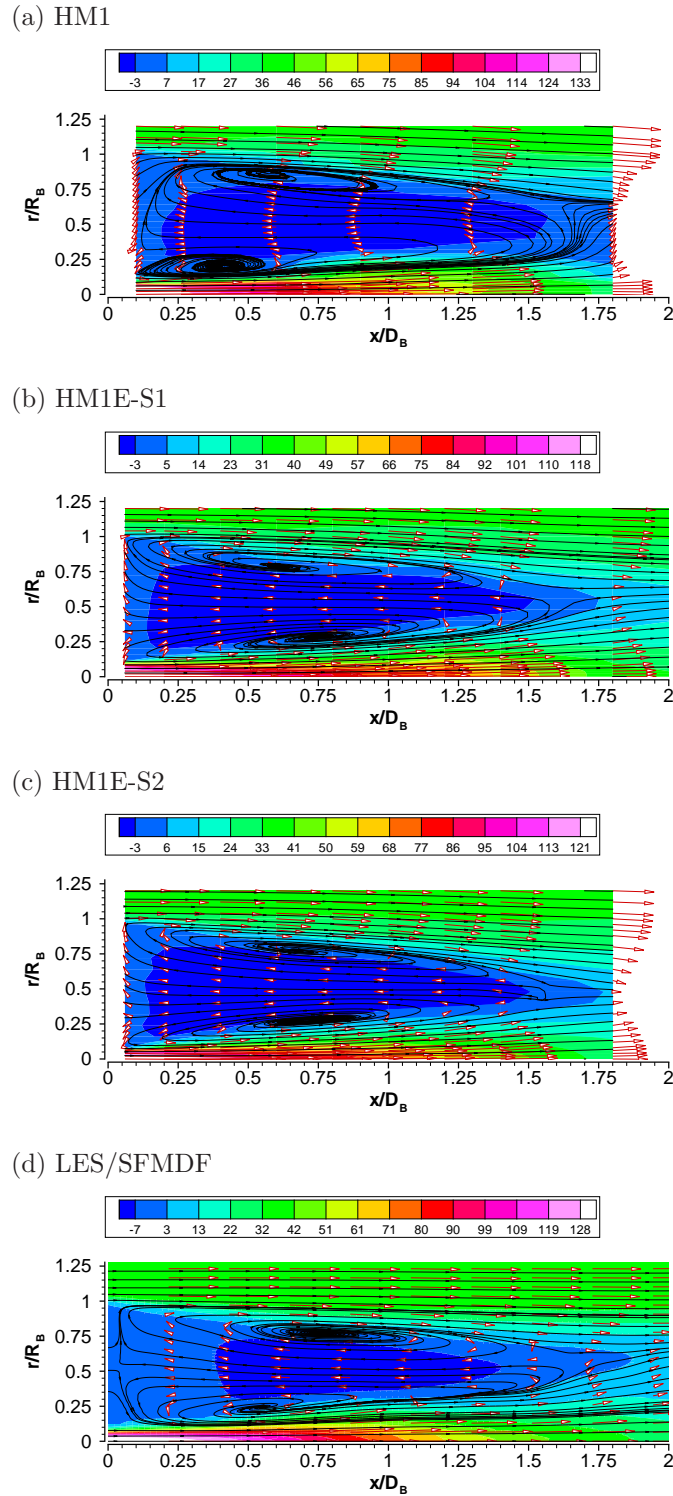


Figure 45: Sydney/Sandia: Time averaged recirculation features as predicted by the LES/SFMDF. The contours denote the streamwise velocity. Superimposed are the streamlines and the velocity vectors.

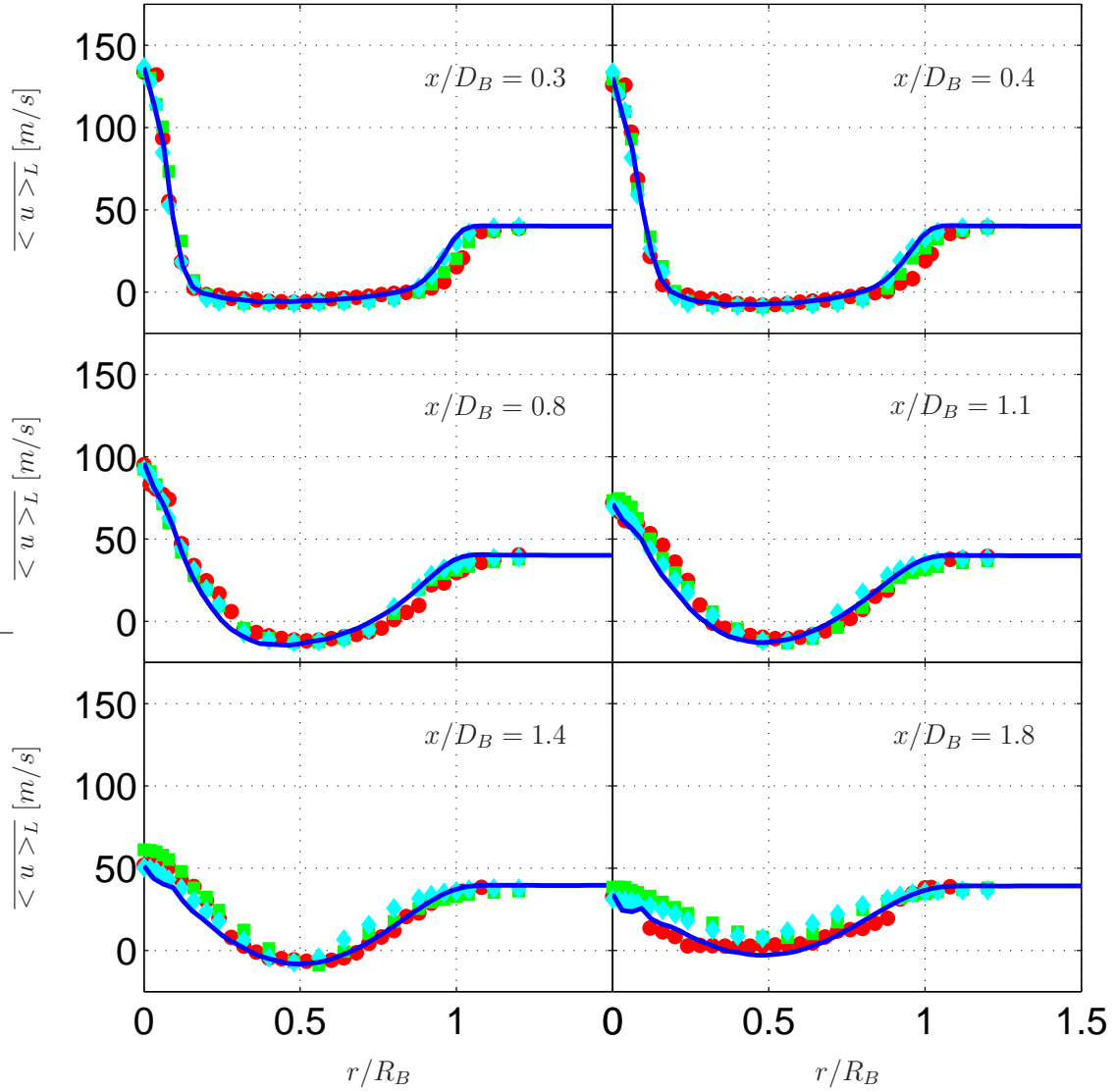


Figure 46: Sydney/Sandia: Radial profiles of the mean value of the streamwise velocity for the reacting flow. — LES/SFMD, ● HM1, ■ HM1E-S1, ◆ HM1E-S2.

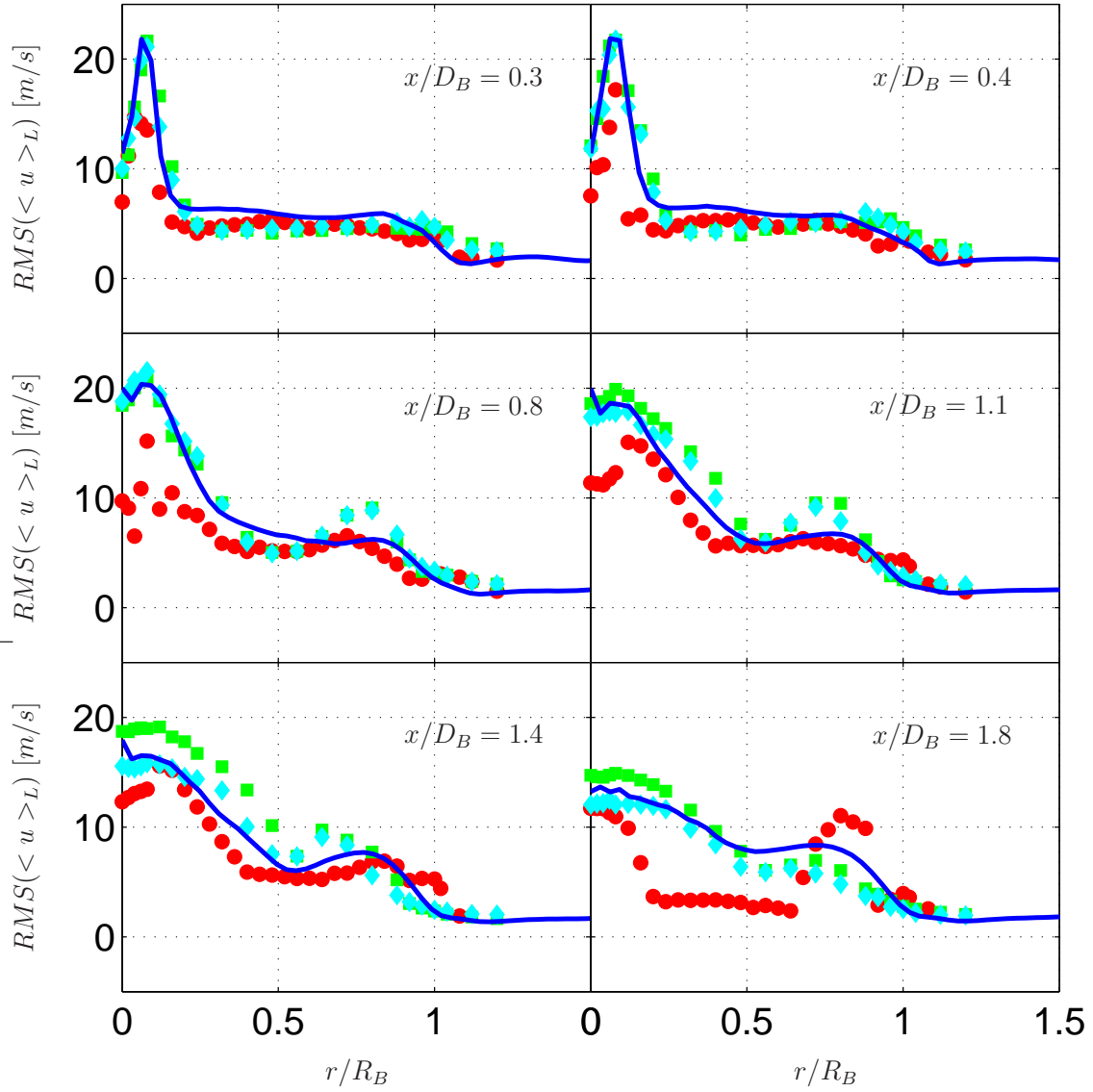


Figure 47: Sydney/Sandia: Radial profiles of the resolved RMS values of the streamwise velocity for the reacting flow. — LES/SFMDF, ● HM1, ■ HM1E-S1, ◆ HM1E-S2.

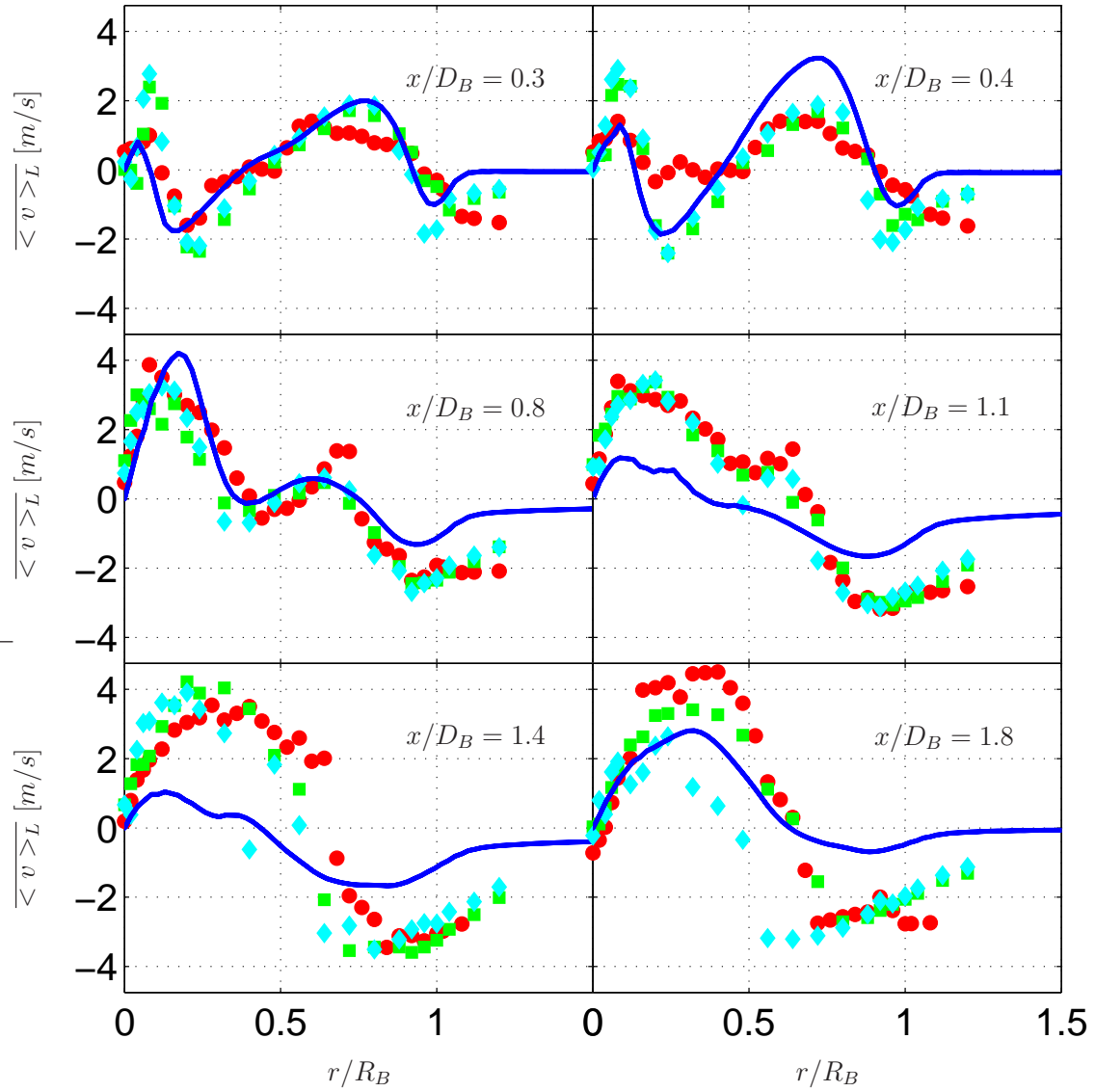


Figure 48: Sydney/Sandia: Radial profiles of the mean values of the radial velocity for the reacting flow. — LES/SFMDF, • HM1, ■ HM1E-S1, ◆ HM1E-S2.

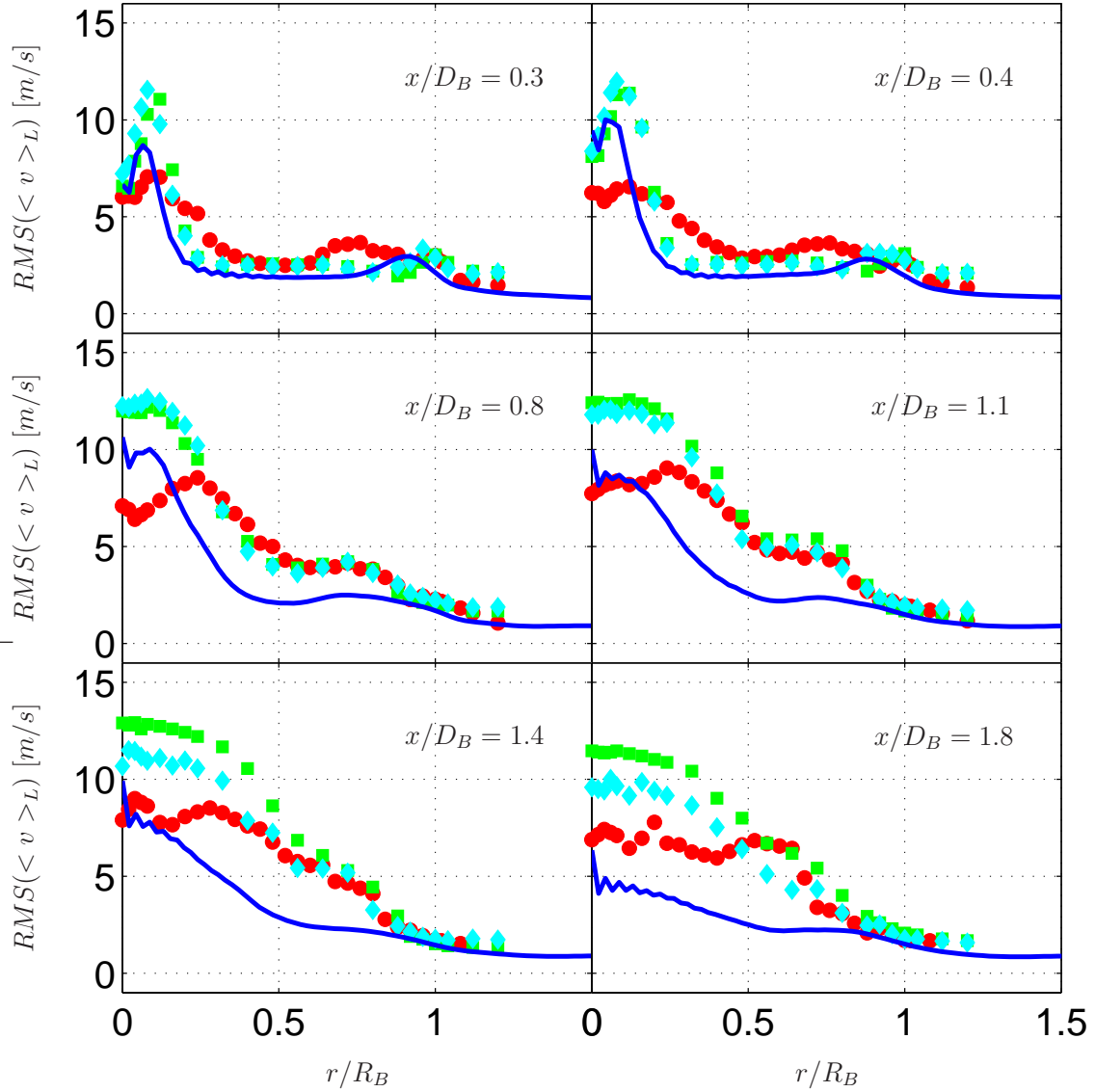


Figure 49: Sydney/Sandia: Radial profiles of the resolved RMS values of the radial velocity for the reacting flow. — LES/SFMD, • HM1, ■ HM1E-S1, ◆ HM1E-S2.

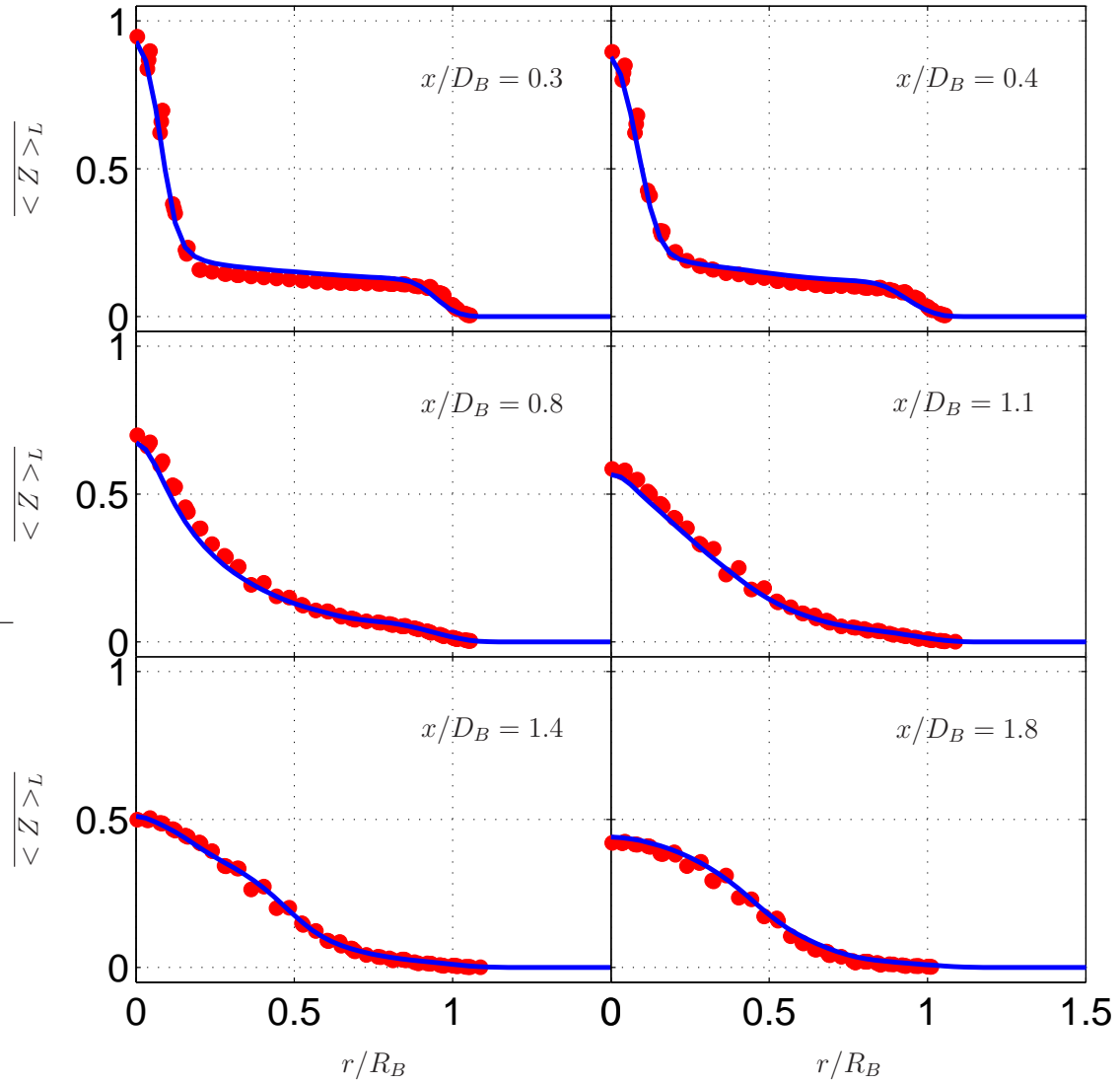


Figure 50: Sydney/Sandia: Radial profiles of the mean values of the mixture fraction for the reacting flow. — LES/SFMDF, • HM1.

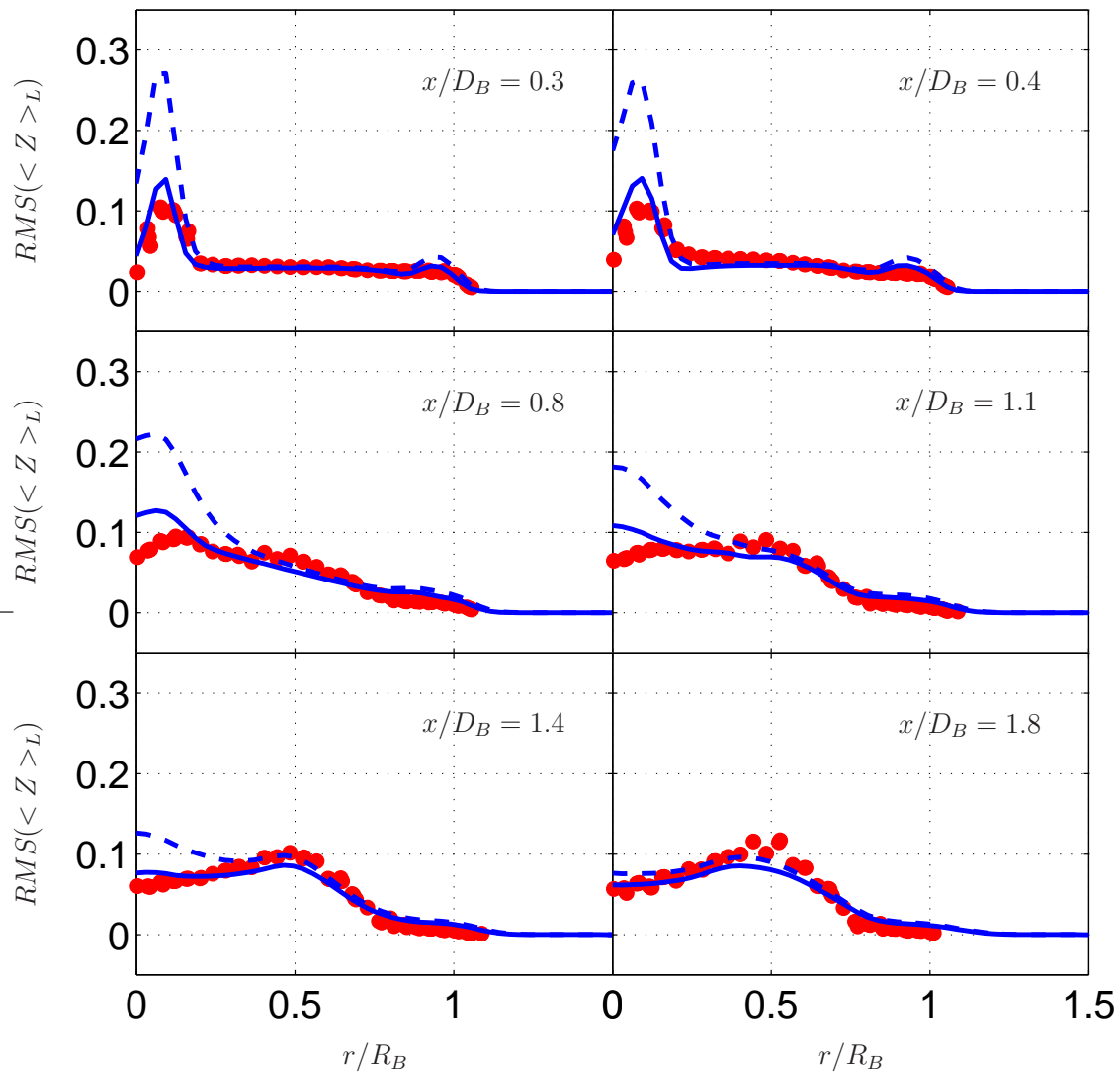


Figure 51: Sydney/Sandia: Radial profiles of the RMS values of the mixture fraction for the reacting flow. — Resolved LES/SFMDF, - - Total LES/SFMDF, • HM1.

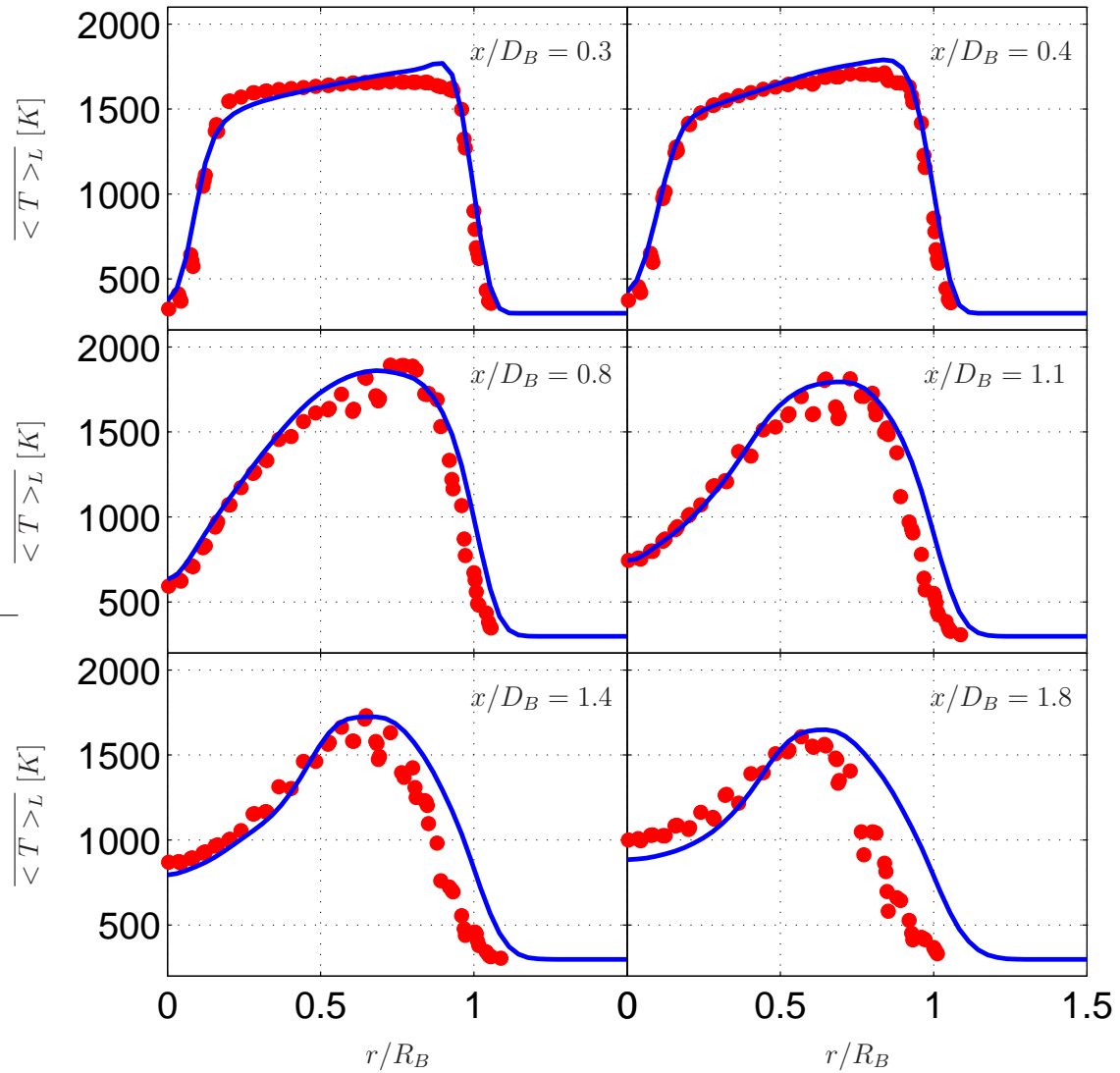


Figure 52: Sydney/Sandia: Radial profiles of the mean values of the temperature for the reacting flow. — LES/SFMDF, • HM1.

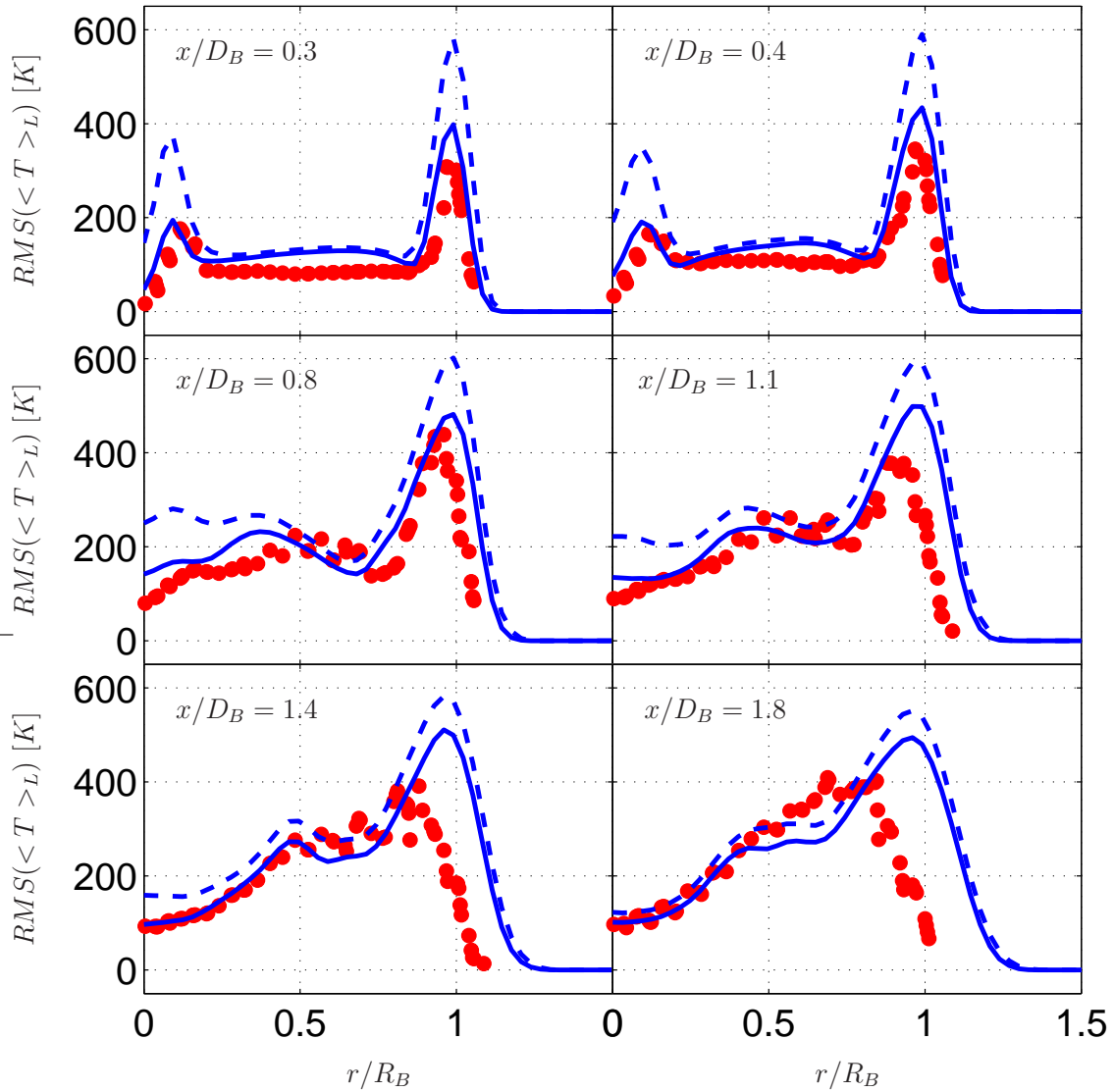


Figure 53: Sydney/Sandia: Radial profiles of the RMS values of the temperature for the reacting flow. — Resolved LES/SFMDF, - - Total LES/SFMDF, • HM1.

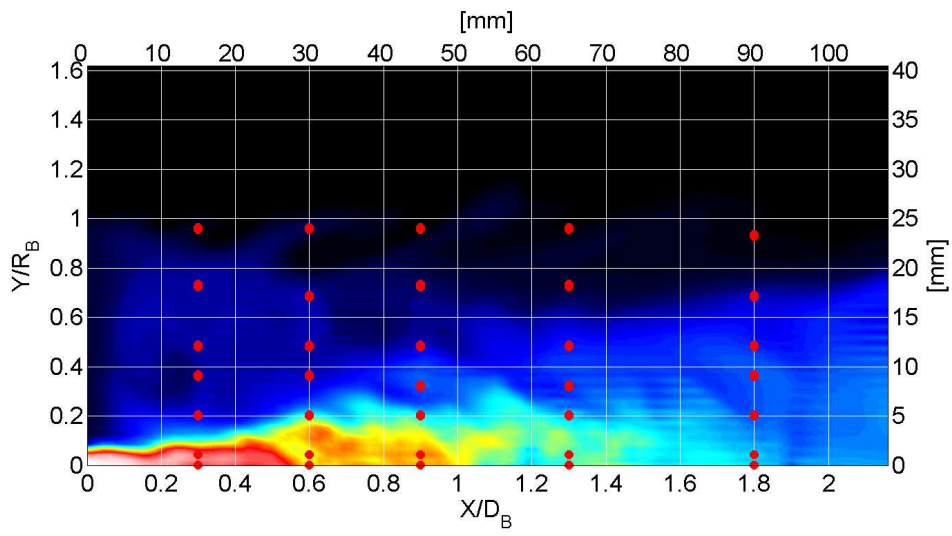


Figure 54: Sydney/Sandia: Locations (•) where the PDFs are available from the experiment.

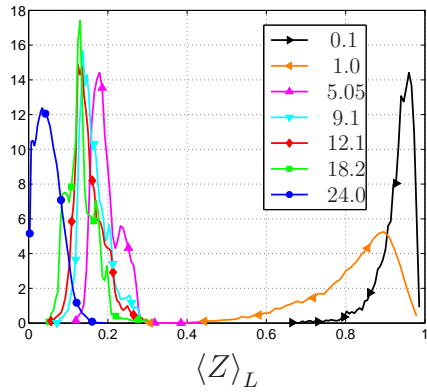
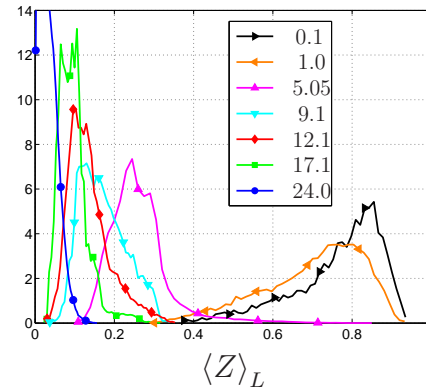
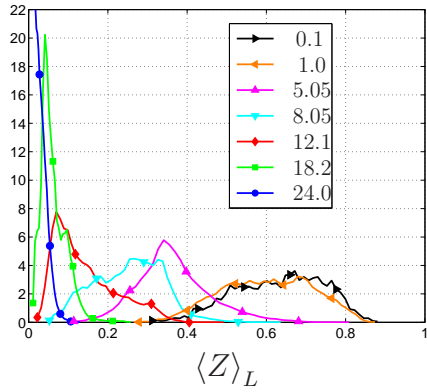
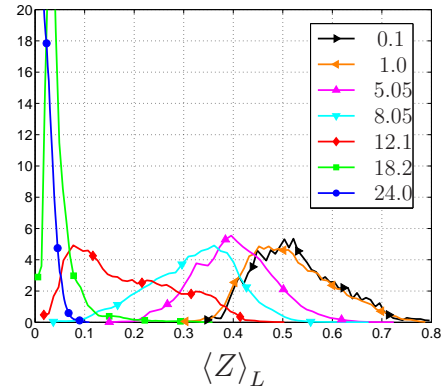
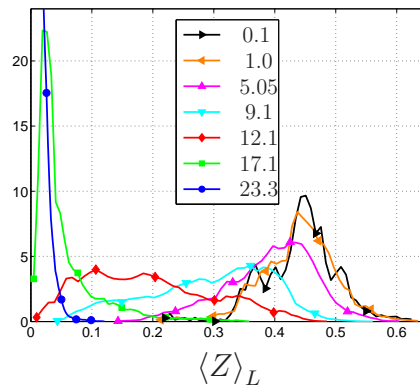
(a)  $x/D_B = 0.3$ (b)  $x/D_B = 0.6$ (c)  $x/D_B = 0.9$ (d)  $x/D_B = 1.3$ (e)  $x/D_B = 1.8$ 

Figure 55: Sydney/Sandia: PDFs of the resolved mixture fraction at several streamwise locations. The legend denotes the radial ( $r$  [mm]) locations.

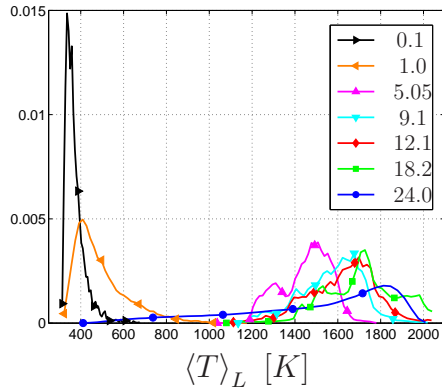
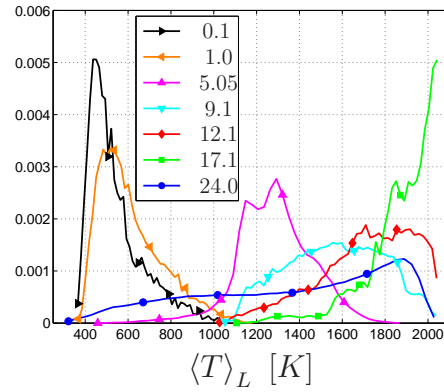
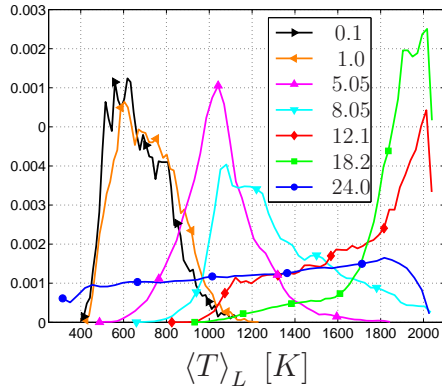
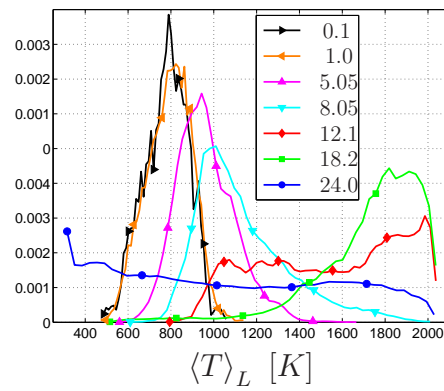
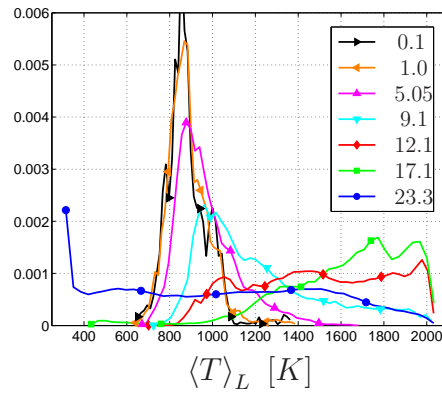
(a)  $x/D_B = 0.3$ (b)  $x/D_B = 0.6$ (c)  $x/D_B = 0.9$ (d)  $x/D_B = 1.3$ (e)  $x/D_B = 1.8$ 

Figure 56: Sydney/Sandia: PDFs of the resolved temperature at several streamwise locations. The legend denotes the radial ( $r [mm]$ ) locations.

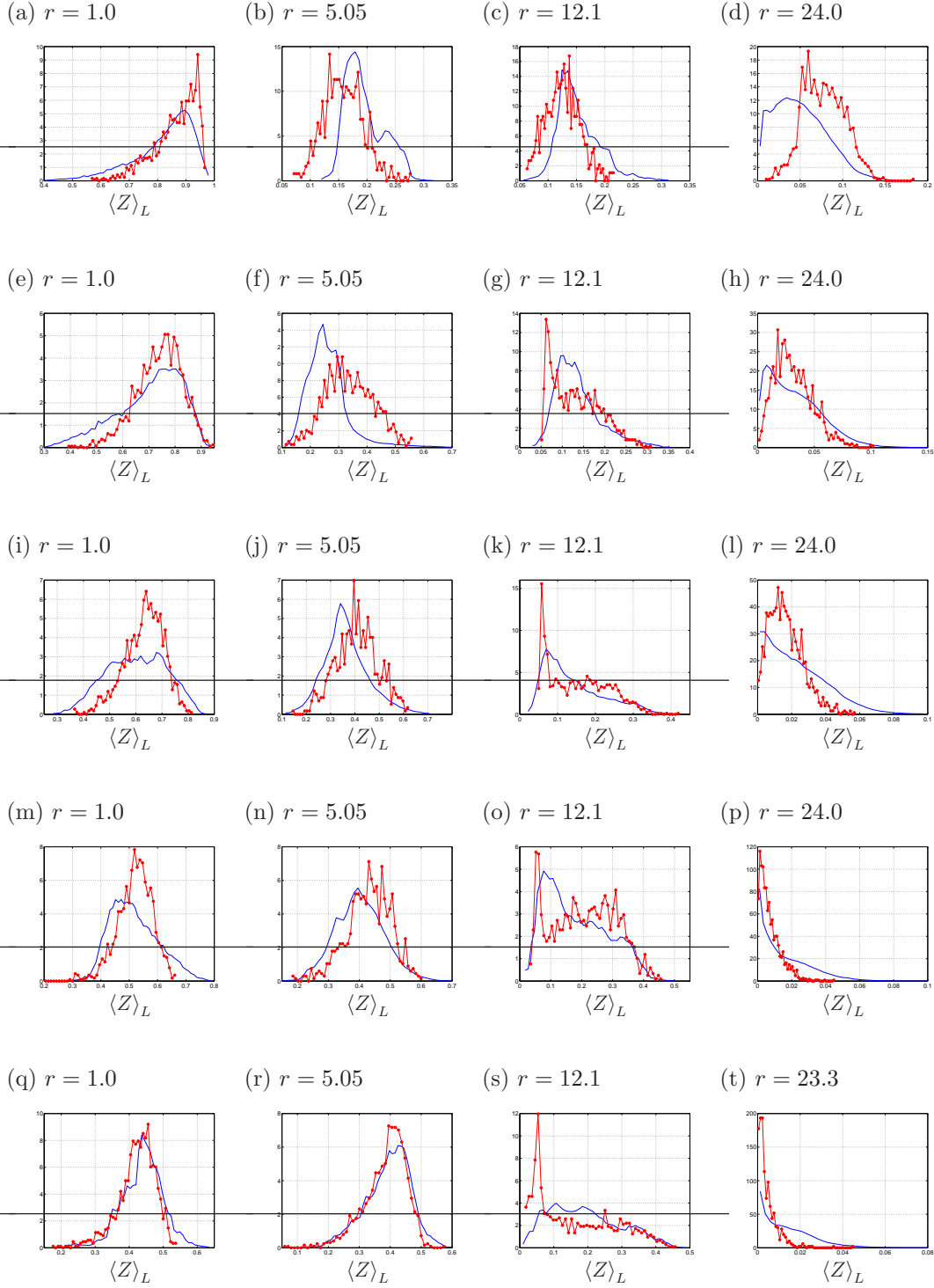


Figure 57: Sydney/Sandia: PDFs of the resolved mixture fraction at (top-to-bottom rows)  $x/D_B = 0.3, 0.6, 0.9, 1.3, 1.8$  and selected radial locations ( $r$  [mm], see Figure 54).

— LES/SFMDF, —●— HM1.

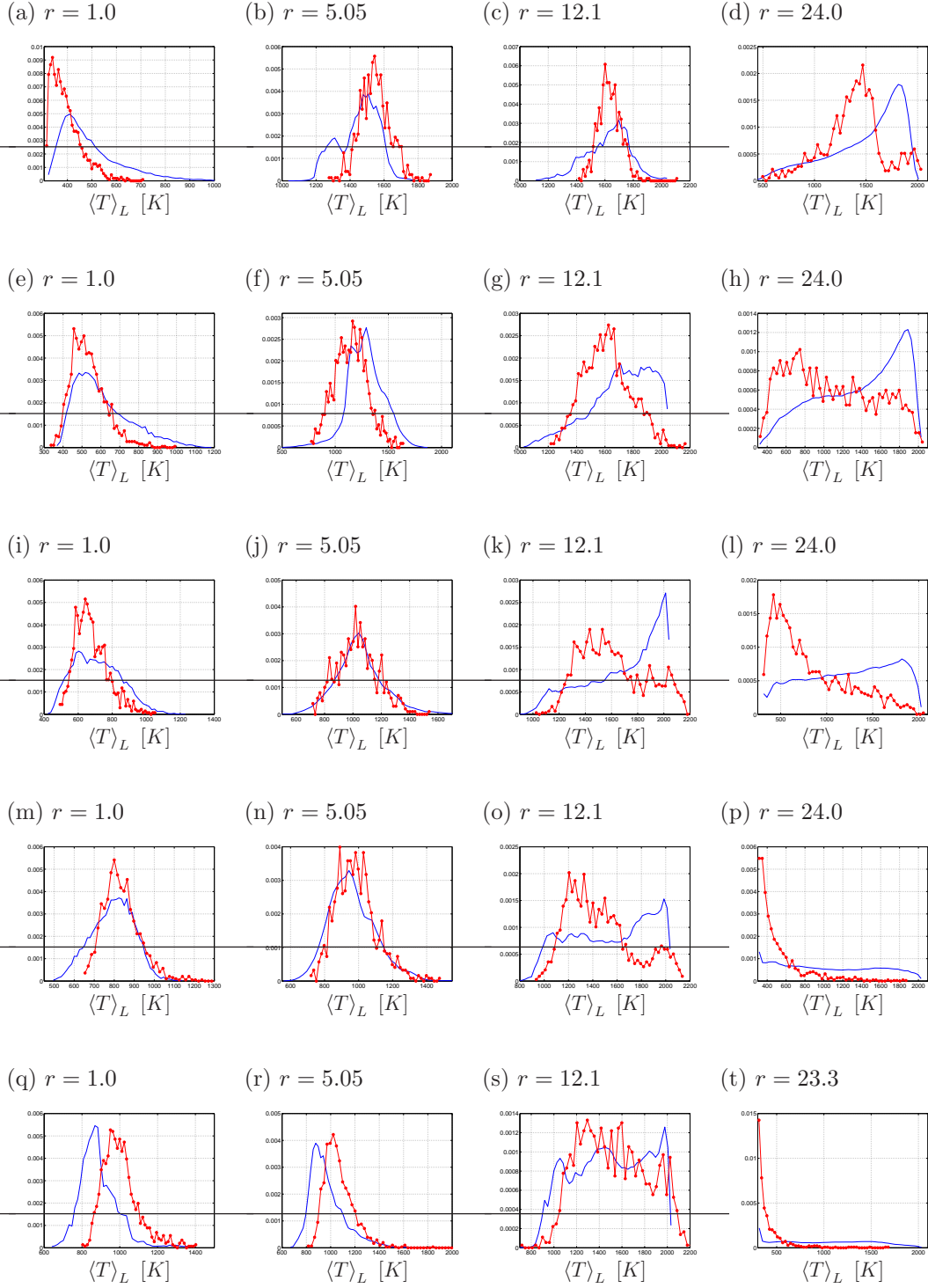


Figure 58: Sydney/Sandia: PDFs of the resolved temperature at (top-to-bottom rows)  $x/D_B = 0.3, 0.6, 0.9, 1.3, 1.8$  and selected radial locations ( $r$  [mm], see Figure 54).

— LES/SFMDF, —●— HM1.

## 4.0 CONCLUSION

The filtered density function (FDF) methodology<sup>25</sup> is now at a stage that it can be used for accurate large eddy simulation (LES) of complex turbulent reacting flows. This is demonstrated in this work by utilizing the scalar filtered mass density function (SFMDf) for LES of a piloted, non-premixed, turbulent, methane jet flame (Sandia/TUD)<sup>1-3</sup> and a bluff-body stabilized hydrogen-methane (Sydney/Sandia)<sup>9,50-58</sup> jet flame. For these flames, the thermo-chemical variables are related to the mixture fraction. This is done by construction of a flamelet library (in a counter-flow jet flame) in which the chemical reaction is modeled by detailed kinetics.<sup>63,64</sup> It is useful to note that the approach here is fundamentally different from those followed in previous flamelet based subgrid scale (SGS) models. In most previous contributions,<sup>48,54,65-68</sup> the FDF of the mixture fraction is *assumed* (e.g. beta or other distributions). Here, a modeled transport equation for the mass weighted FDF of the mixture fraction<sup>12</sup> is considered. This equation is solved by a hybrid finite-difference (FD) / Monte Carlo (MC) method. After establishing the consistency and accuracy of the hybrid solver, the predictive capability of the overall scheme is assessed by comparisons with the experimental data. For these comparisons, the ensemble (long time averaged) values of the hydrodynamic and thermo-chemical variables are considered. The resolved PDFs of several thermo-chemical variables are also considered. Good overall agreements with the experimental data are observed.

There are two ways by which this work can be continued. First, is extension of LES/SFMDf for prediction of flames which experience extinction (such as Sandia Flames E and F) and/or re-ignition (such as the higher blow-off value Sydney/Sandia bluff-body flames). This would provide a more definitive assessment of the predictive capabilities of the FDF methods. Such simulations require consideration of finite-rate

chemistry, as demonstrated in probability density function (PDF) based Reynolds averaged simulations (RAS) of Sandia flames,<sup>46,47</sup> and bluff-body flames.<sup>51–53,57,58</sup> Presently, it is not computationally economical to implement very detailed kinetics in LES/FDF. But implementation of reduced finite-rate kinetics schemes using in situ adaptive tabulation, such as those used in RAS/PDF<sup>46,47,53</sup> is within reach. Second, it is desirable to implement the LES/SFMDF for prediction of other complex flame configurations. Accomplishments of these tasks can be further expedited by reduction and optimization of the computational requirements of the FDF.

## APPENDIX

### ADDITIONAL LES/SFMDP DATA ON SYDNEY/SANDIA FLAME

This appendix provides additional scalar field data as predicted by the LES/SFMDP of the Sydney/Sandia flames. The radial profiles for the mean values of the mass fractions of the oxygen ( $O_2$ ), water ( $H_2O$ ), carbon monoxide ( $CO$ ), hydrogen ( $H_2$ ), carbon dioxide ( $CO_2$ ), and hydroxyl radical ( $OH$ ) are shown in Figs. 59, 61, 63, 65, 66, and 67, respectively. The radial profiles of the RMS values of the oxygen, water, and carbon monoxide are shown in Figs. 60, 62, and 64, respectively. The level of agreement between the experimental data and LES/SFMDP is directly related to that of the flamelet table (Fig. 35). In general, the mean values of the oxygen are underpredicted on the fuel lean side. The mean values of water and hydroxyl radical are overpredicted. The mean values of carbon monoxide and dioxide are underpredicted on the fuel rich side, although the agreement improves at downstream locations. These features are also observed in the RMS values.

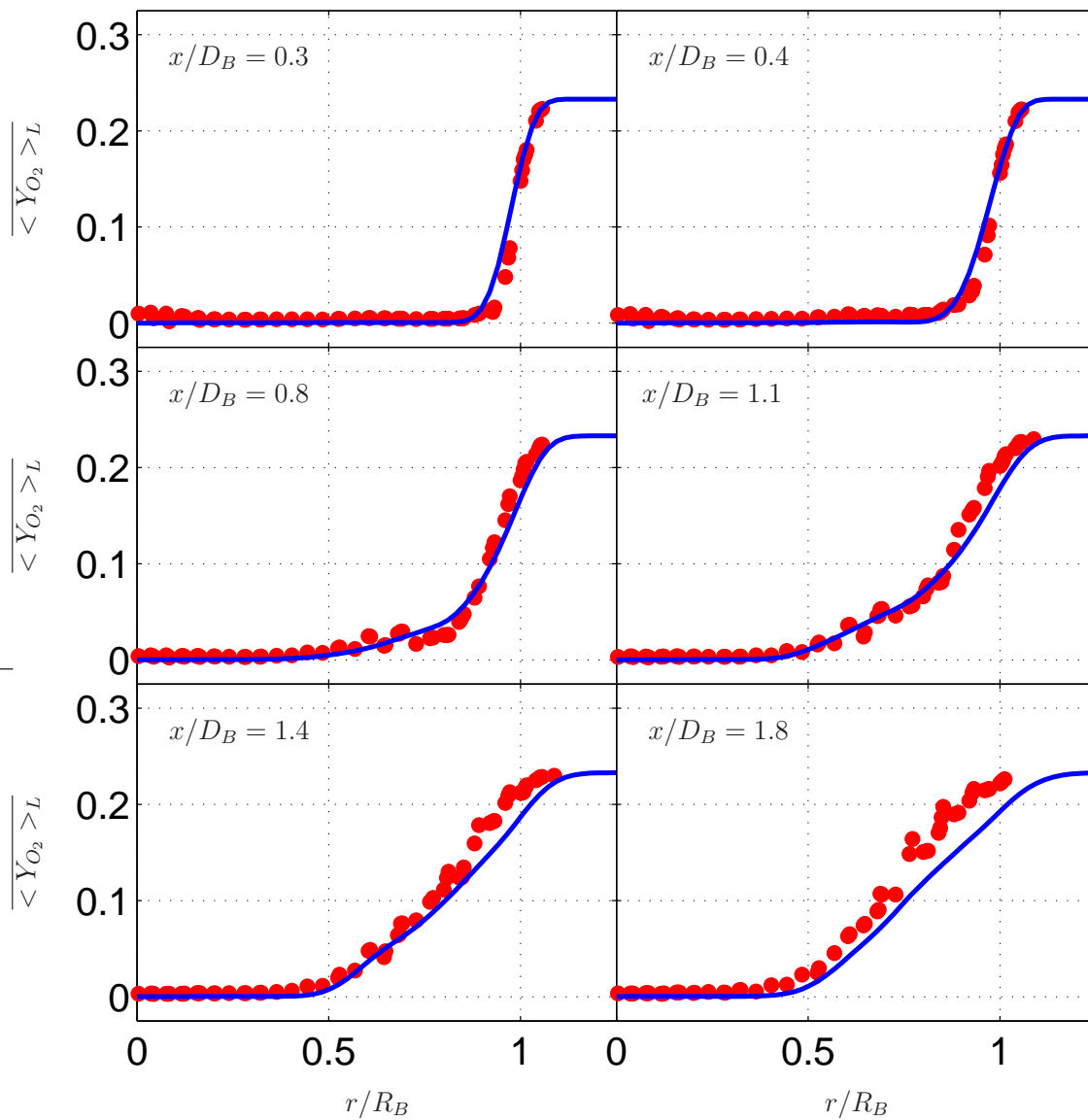


Figure 59: Sydney/Sandia: Radial profiles of the mean values of the oxygen mass fraction.

— LES/SFMDF, • HM1.

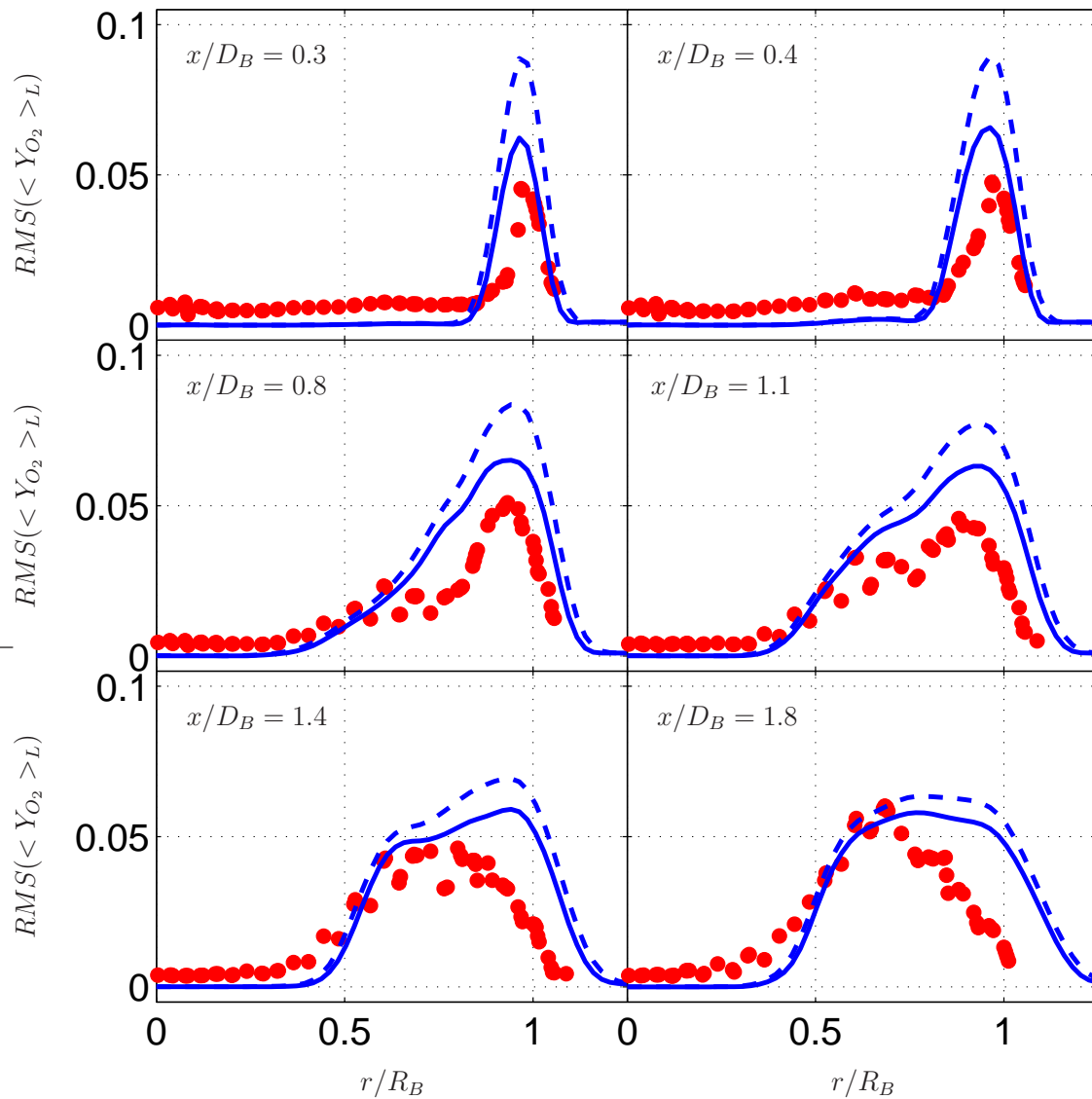


Figure 60: Sydney/Sandia: Radial profiles of the RMS values of the oxygen mass fraction.

— Resolved LES/SFMDF, - - Total LES/SFMDF, • HM1.

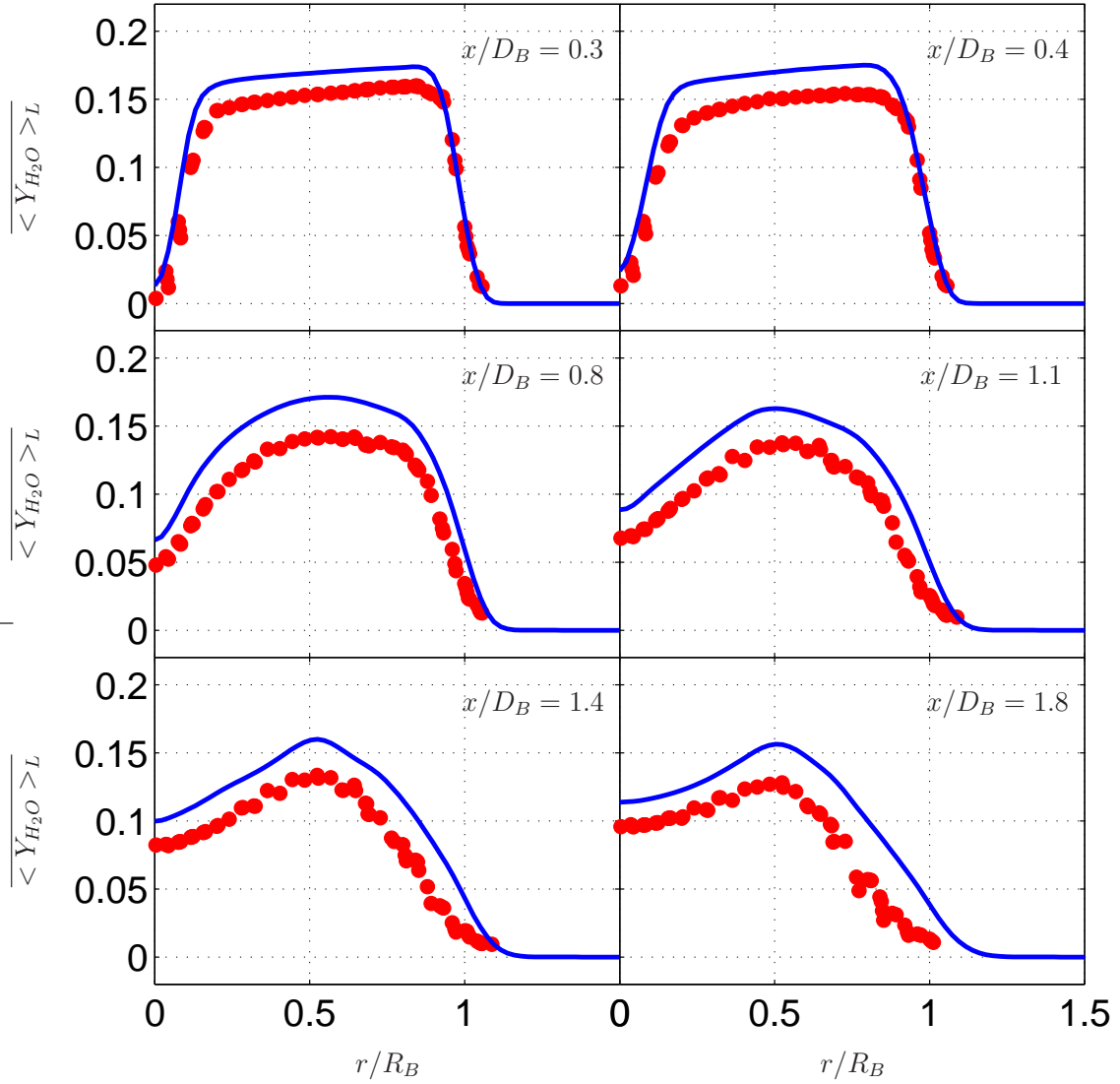


Figure 61: Sydney/Sandia: Radial profiles of the mean values of the water mass fraction.

— LES/SFMDF, • HM1.

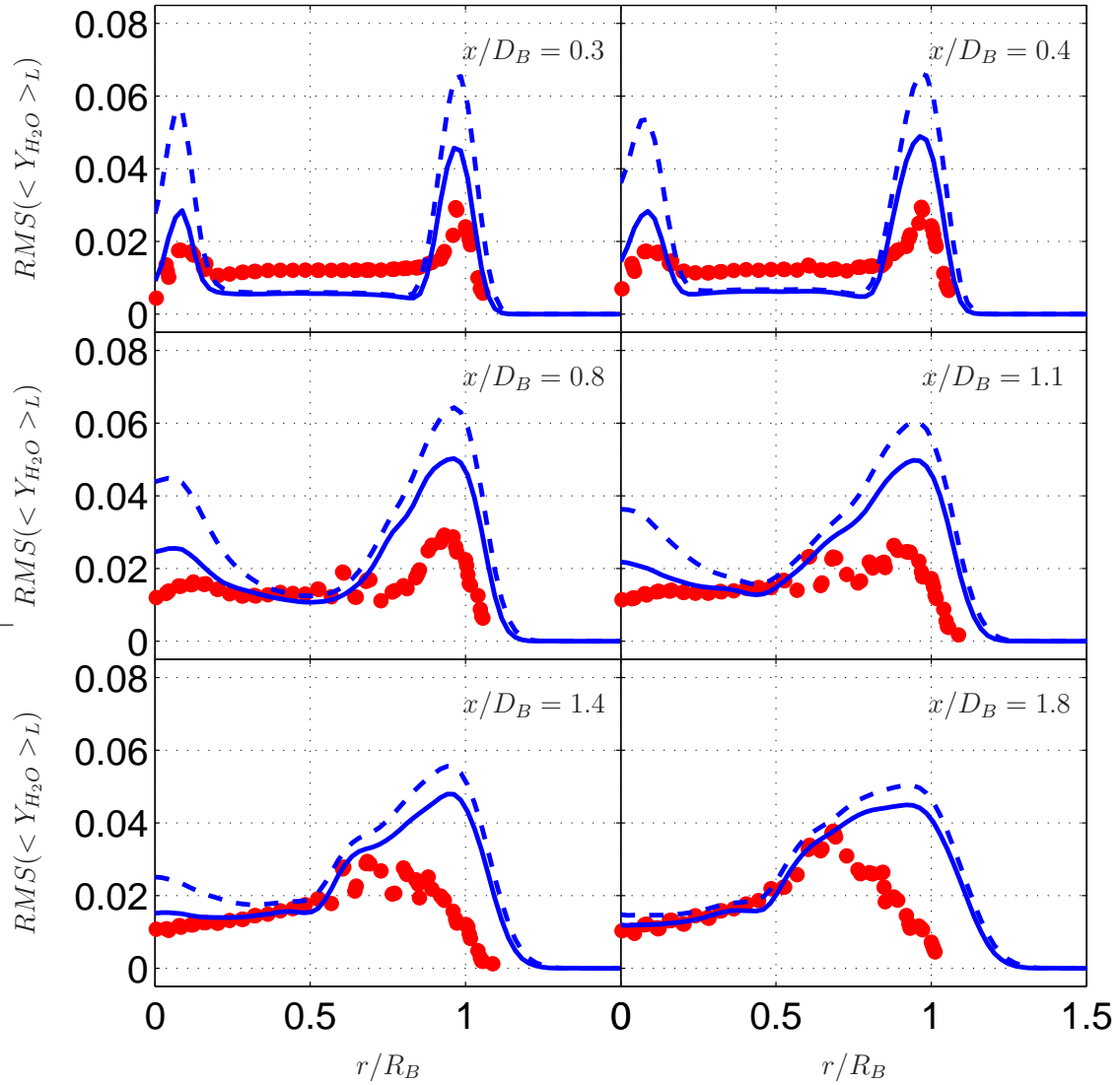


Figure 62: Sydney/Sandia: Radial profiles of the RMS values of the water mass fraction.

— Resolved LES/SFMDF, - - Total LES/SFMDF, • HM1.

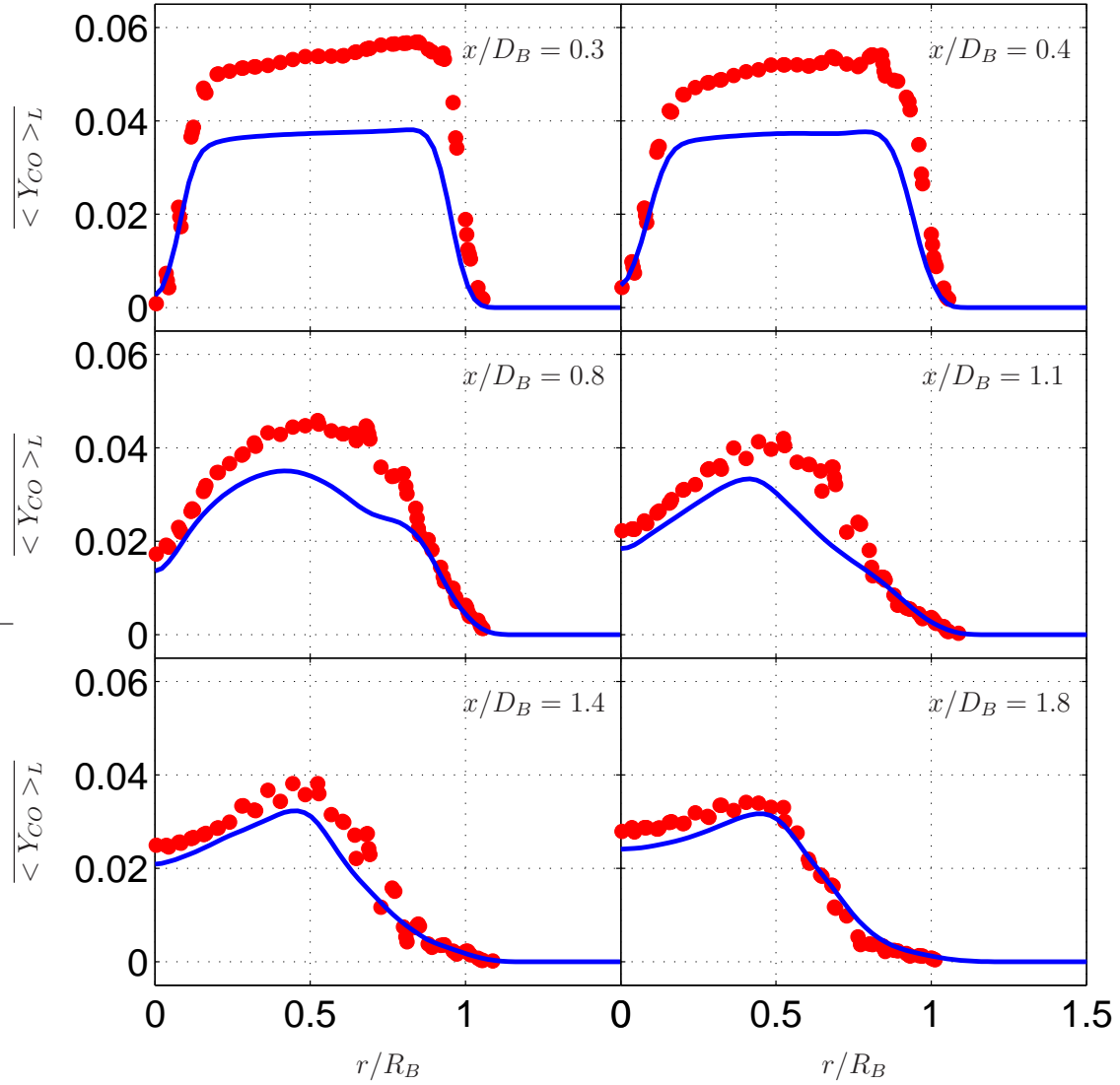


Figure 63: Sydney/Sandia: Radial profiles of the mean values of the carbon monoxide mass fraction. — LES/SFMDF, • HM1.

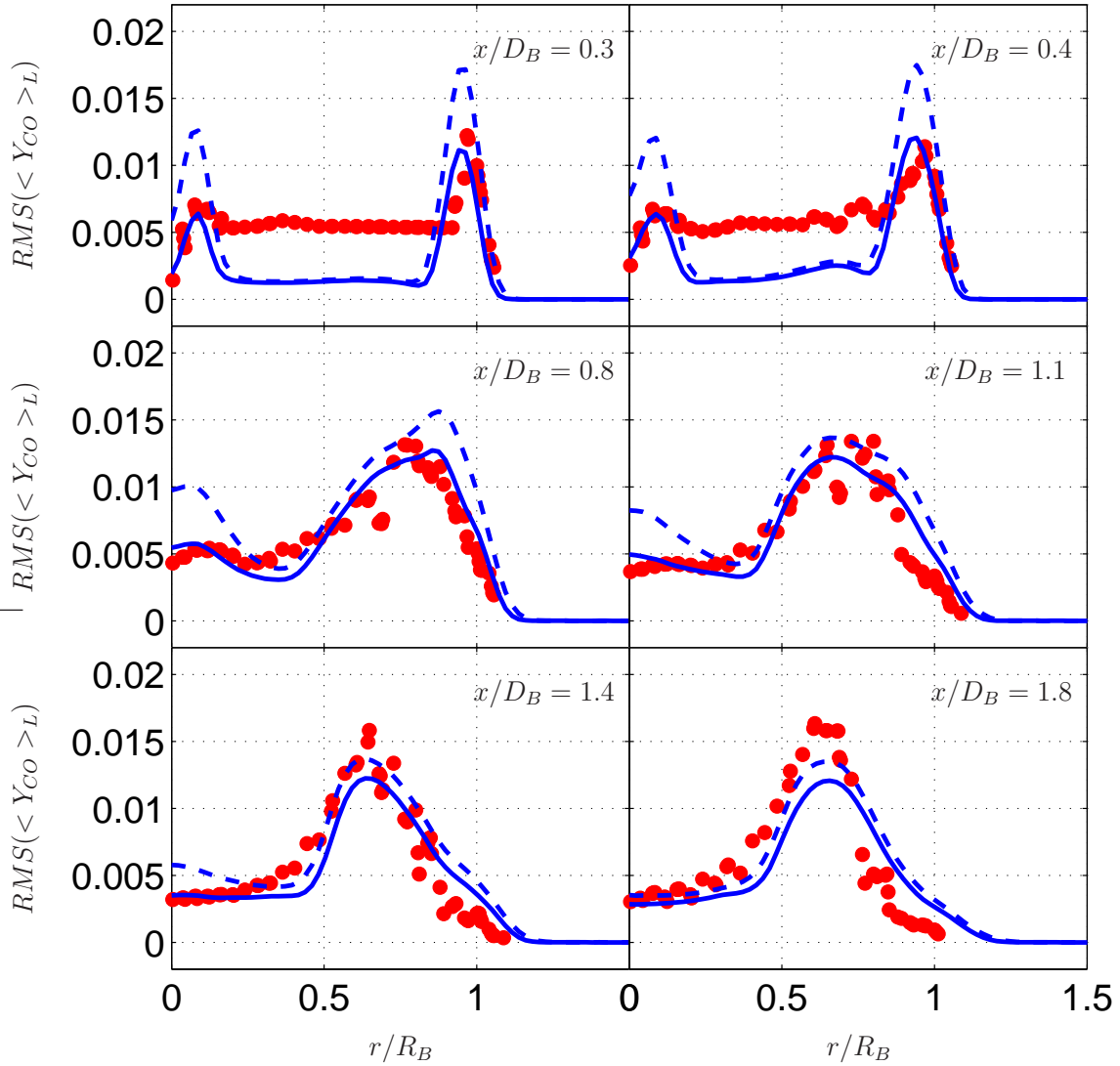


Figure 64: Sydney/Sandia: Radial profiles of the RMS values of the carbon monoxide mass fraction. — Resolved LES/SFMDF, - - Total LES/SFMDF, • HM1.

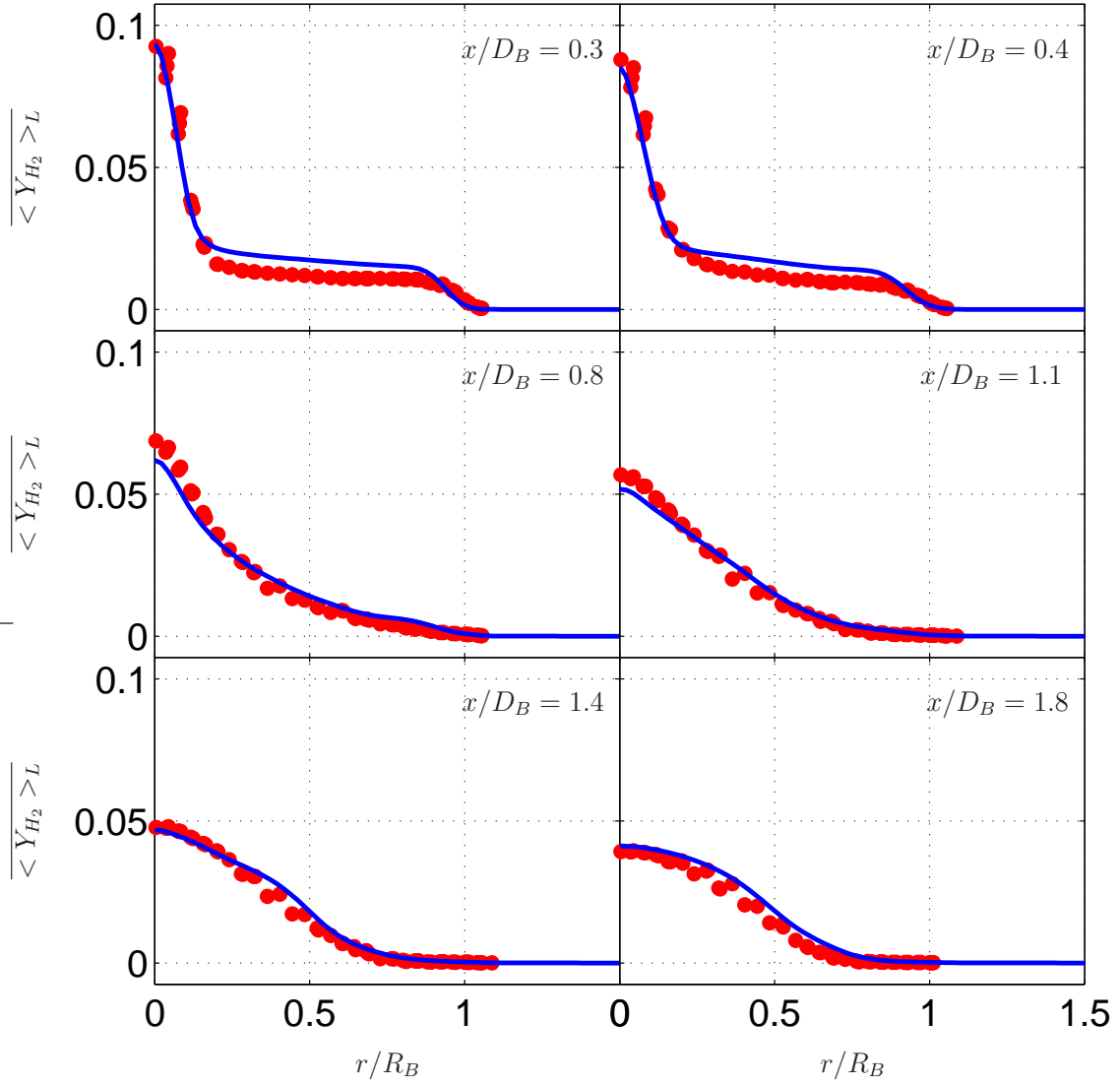


Figure 65: Sydney/Sandia: Radial profiles of the mean values of the hydrogen mass fraction.

— LES/SFMDF, • HM1.

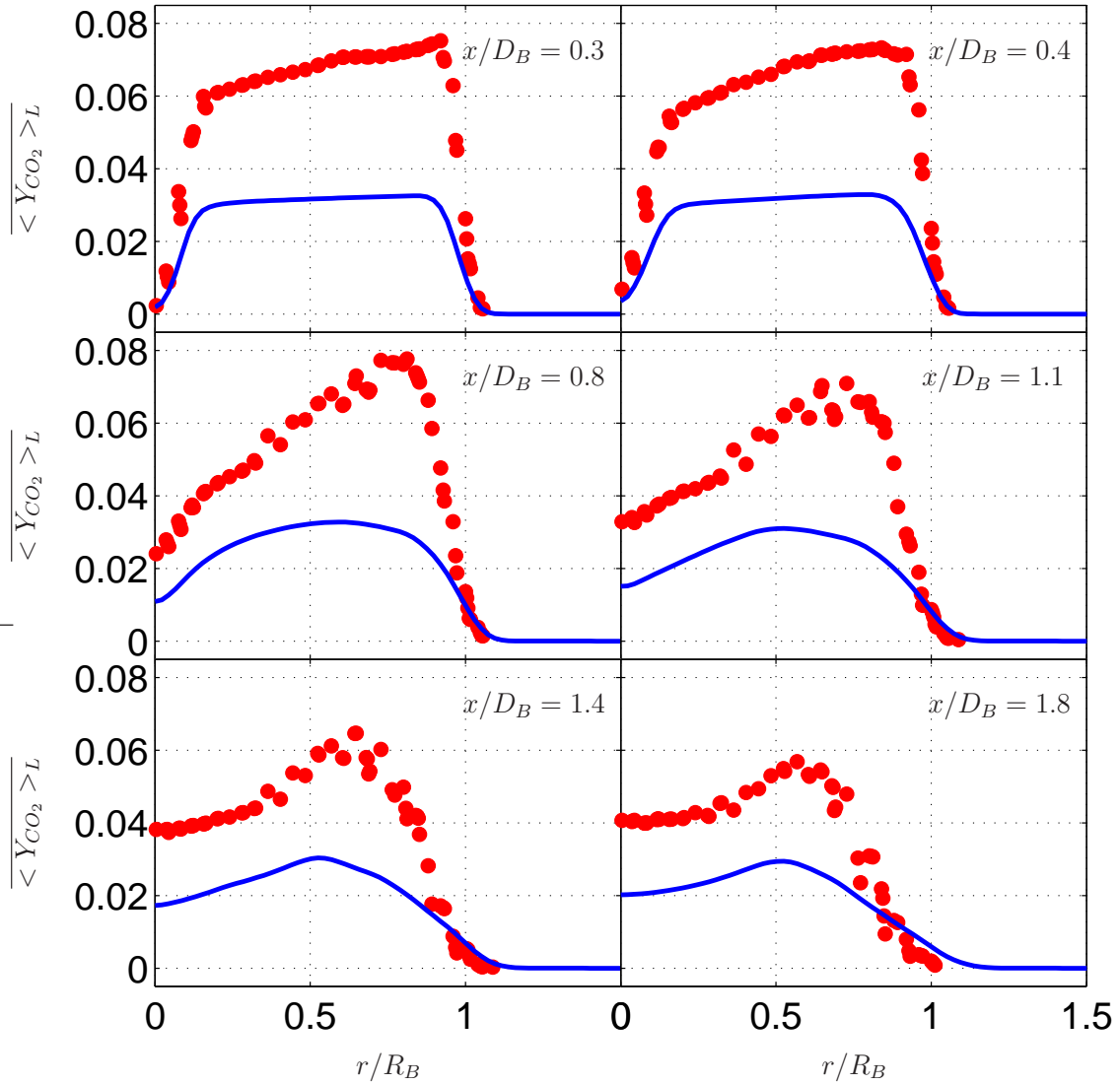


Figure 66: Sydney/Sandia: Radial profiles of the mean values of the carbon dioxide mass fraction. — LES/SFMDF, • HM1.

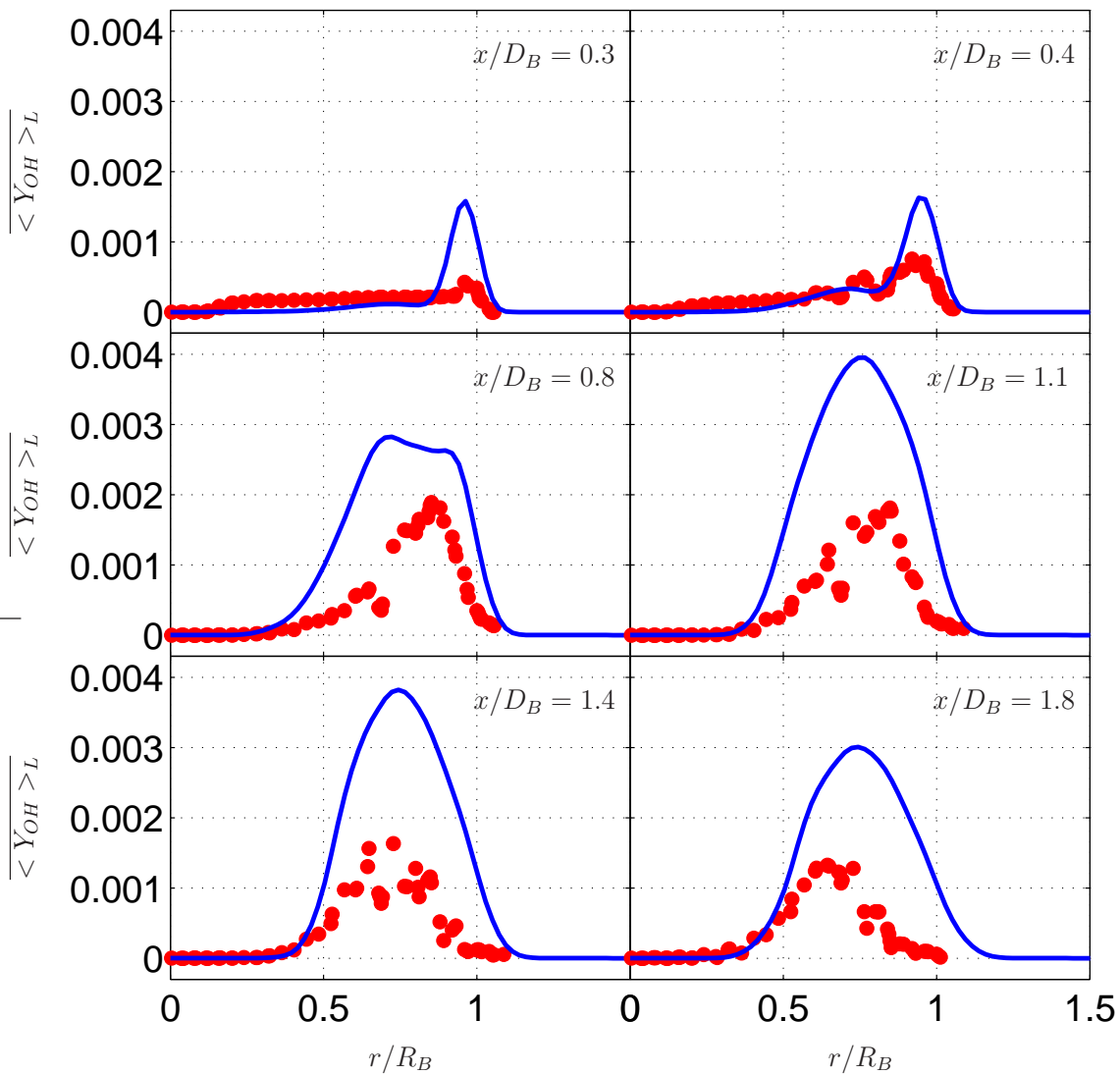


Figure 67: Sydney/Sandia: Radial profiles of the mean values of the hydroxyl radical mass fraction. — LES/SFMDF, • HM1.

## BIBLIOGRAPHY

- [1] Barlow, R. S. and Frank, J. H., Effects of Turbulence on Species Mass Fractions in Methane/Air Jet Flames, *Proc. Combust. Inst.*, **27**:1087–1095 (1998).
- [2] Sandia National Laboratories, TNF Workshop website, Piloted Flames, <http://www.ca.sandia.gov/TNF/pilotedjet.html>, 2005.
- [3] Schneider, C., Dreizler, A., Janicka, J., and Hassel, E. P., Flow Field Measurements of Stable and Locally Extinguishing Hydrocarbon-Fuelled Jet Flames, *Combust. Flame*, **135**:185–190 (2003).
- [4] Masri, A. R., Dibble, R. W., and Barlow, R. S., Raman-Rayleigh Measurements in Bluff Body Stabilised Flames of Hydrocarbon Fuels, *Proc. Combust. Inst.*, **24**:317–324 (1992).
- [5] Masri, A. R., Dally, B. B., Barlow, R. S., and Carter, C. D., The Structure of The Recirculation Zone of a Bluff-Body Combustor, *Proc. Combust. Inst.*, **25**:1301–1308 (1994).
- [6] Masri, A. R., Dibble, R. W., and Barlow, R. S., The Structure of Turbulent Nonpremixed Flames Revealed by Raman-Rayleigh-LIF Measurements, *Prog. Energy Combust. Sci.*, **22**:307–362 (1996).
- [7] Dally, B. B., Masri, A. R., Barlow, R. S., Fiechtner, G. J., and Fletcher, D. F., Measurements of NO in Turbulent Nonpremixed Flames Stabilised on a Bluff-Body, *Proc. Combust. Inst.*, **26**(2):2191–2197 (1996).
- [8] Dally, B. B., Masri, A. R., Barlow, R. S., and Fiechtner, G. J., Instantaneous and Mean Compositional Structure of Bluff-Body Stabilized Nonpremixed Flames, *Combust. Flame*, **114**:119–148 (1998).
- [9] Dally, B. B., Fletcher, D. F., and Masri, A. R., Flow and Mixing Fields of Turbulent Bluff-Body Jets and Flames, *Combust. Theory Modelling*, **2**:193–219 (1998).
- [10] University of Sydney, Thermal Research Group website, Bluff-Body Flames, <http://www.mech.eng.usyd.edu.au/thermofluids/bluff.htm>, 2005.

- [11] Sandia National Laboratories, TNF Workshop website, Bluff-Body Flames, <http://www.ca.sandia.gov/TNF/bluffbod.html>, 2005.
- [12] Jaberri, F. A., Colucci, P. J., James, S., Givi, P., and Pope, S. B., Filtered Mass Density Function for Large Eddy Simulation of Turbulent Reacting Flows, *J. Fluid Mech.*, **401**:85–121 (1999).
- [13] Pope, S. B., *Turbulent Flows*, Cambridge University Press, Cambridge, UK, 2000.
- [14] Peters, N., Laminar Diffusion Flamelet Models in Non-Premixed Turbulent Combustion, *Prog. Energy Combust. Sci.*, **10**:319–339 (1984).
- [15] Peters, N., Laminar Flamelet Concepts in Turbulent Combustion, *Proc. Combust. Inst.*, **21**:1231–1250 (1986).
- [16] Cook, A. W. and Riley, J. J., Progress in Subgrid-Scale Combustion Modeling, in Hafez, M. and Oshima, K., editors, *Computational Fluid Dynamics Review 1998*, pp. 914–931, World Scientific, Singapore, 1998.
- [17] Bilger, R. W., Future Progress in Turbulent Combustion Research, *Prog. Energy Combust. Sci.*, **26**(4-6):367–380 (2000).
- [18] Menon, S., Subgrid Combustion Modelling for Large-Eddy Simulations, *Int. J. Engine Research*, **1**(2):209–227 (2000).
- [19] Peters, N., *Turbulent Combustion*, Cambridge University Press, Cambridge, UK, 2000.
- [20] Oran, E. S. and Boris, J. P., *Numerical Simulation of Reactive Flows*, Cambridge University Press, New York, NY, 2nd edition, 2001.
- [21] Poinso, T. and Veynante, D., *Theoretical and Numerical Combustion*, R.T. Edwards, Inc., Philadelphia, PA, second edition, 2005.
- [22] Veynante, D. and Vervisch, L., Turbulent Combustion Modeling, *Prog. Energy Combust. Sci.*, **28**(3):193–301 (2002).
- [23] Givi, P., Subgrid Scale Modeling in Turbulent Combustion: A Review, AIAA Paper 2003-5081, 2003.
- [24] Givi, P., Model Free Simulations of Turbulent Reactive Flows, *Prog. Energy Combust. Sci.*, **15**:1–107 (1989).
- [25] Pope, S. B., Computations of Turbulent Combustion: Progress and Challenges, *Proc. Combust. Inst.*, **23**:591–612 (1990).
- [26] Pope, S. B., PDF Methods for Turbulent Reactive Flows, *Prog. Energy Combust. Sci.*, **11**:119–192 (1985).

- [27] Madnia, C. K. and Givi, P., Direct Numerical Simulation and Large Eddy Simulation of Reacting Homogeneous Turbulence, In Galperin and Orszag<sup>114</sup>, chapter 15, pp. 315–346.
- [28] Frankel, S. H., Adumitroaie, V., Madnia, C. K., and Givi, P., Large Eddy Simulations of Turbulent Reacting Flows by Assumed PDF Methods, in Ragab, S. A. and Piomelli, U., editors, *Engineering Applications of Large Eddy Simulations*, pp. 81–101, ASME, FED-Vol. 162, New York, NY, 1993.
- [29] Givi, P., Spectral and Random Vortex Methods in Turbulent Reacting Flows, in Libby, P. A. and Williams, F. A., editors, *Turbulent Reacting Flows*, chapter 8, pp. 475–572, Academic Press, London, UK, 1994.
- [30] Colucci, P. J., Jaber, F. A., Givi, P., and Pope, S. B., Filtered Density Function for Large Eddy Simulation of Turbulent Reacting Flows, *Phys. Fluids*, **10**(2):499–515 (1998).
- [31] Garrick, S. C., Jaber, F. A., and Givi, P., Large Eddy Simulation of Scalar Transport in a Turbulent Jet Flow, in Knight, D. and Sakell, L., editors, *Recent Advances in DNS and LES, Fluid Mechanics and its Applications*, Vol. 54, pp. 155–166, Kluwer Academic Publishers, The Netherlands, 1999.
- [32] James, S. and Jaber, F. A., Large Scale Simulations of Two-Dimensional Nonpremixed Methane Jet Flames, *Combust. Flame*, **123**:465–487 (2000).
- [33] Gicquel, L. Y. M., Givi, P., Jaber, F. A., and Pope, S. B., Velocity Filtered Density Function for Large Eddy Simulation of Turbulent Flows, *Phys. Fluids*, **14**(3):1196–1213 (2002).
- [34] Réveillon, J. and Vervisch, L., Subgrid-Scale Turbulent Micromixing: Dynamic Approach, *AIAA J.*, **36**(3):336–341 (1998).
- [35] Gao, F. and O’Brien, E. E., A Large-Eddy Simulation Scheme for Turbulent Reacting Flows, *Phys. Fluids A*, **5**(6):1282–1284 (1993).
- [36] Cook, A. W. and Riley, J. J., A Subgrid Model for Equilibrium Chemistry in Turbulent Flows, *Phys. Fluids*, **6**(8):2868–2870 (1994).
- [37] Zhou, X. Y. and Pereira, J. C. F., Large Eddy Simulation (2D) of a Reacting Plan Mixing Layer Using Filtered Density Function, *Flow, Turb. Combust.*, **64**:279–300 (2000).
- [38] Luo, K. H., DNS and LES of Turbulence-Combustion Interactions, In Geurts<sup>115</sup>, chapter 14, pp. 263–293.
- [39] Tong, C., Measurements of Conserved Scalar Filtered Density Function in a Turbulent Jet, *Phys. Fluids*, **13**(10):2923–2937 (2001).

- [40] Raman, V., Pitsch, H., and Fox, R. O., Consistent Hybrid LES-FDF Formulation for the Simulation of Turbulent Combustion, in *Annual Research Briefs*, Center for Turbulence Research, Stanford University, Stanford, CA, 2004.
- [41] Launder, B. E. and Sandham, N. D., editors, *Closure Strategies for Turbulent and Transitional Flows*, Cambridge University Press, 2002.
- [42] Sheikhi, M. R. H., Drozda, T. G., Givi, P., Jaber, F. A., and Pope, S. B., Large Eddy Simulation of a Turbulent Nonpremixed Piloted Methane Jet Flame (Sandia Flame D), *Proc. Combust. Inst.*, **30**:549–556 (2005).
- [43] Drozda, T. G., Consistency Assessment of Velocity-Scalar Filtered Density Function for Large-Eddy Simulation of Turbulent Flows, M.S. Thesis, Department of Mechanical and Aerospace Engineering, University at Buffalo, State University of New York, Buffalo, NY, 2002.
- [44] Sheikhi, M. R. H., Drozda, T. G., Givi, P., and Pope, S. B., Velocity-Scalar Filtered Density Function for Large Eddy Simulation of Turbulent Flows, *Phys. Fluids*, **15**(8):2321–2337 (2003).
- [45] Sheikhi, M. R. H., Joint Velocity-Scalar Filtered Density Function for Large Eddy Simulation of Turbulent Reacting Flows, Ph.D. Thesis, Department of Mechanical Engineering, University of Pittsburgh, Pittsburgh, PA, 2005, in progress.
- [46] Tang, Q., Xu, J., and Pope, S. B., PDF Calculations of Local Extinction and NO Production in Piloted-Jet Turbulent Methane/Air Flames, *Proc. Combust. Inst.*, **28**:133–139 (2000).
- [47] Xu, J. and Pope, S. B., PDF Calculations of Turbulent Nonpremixed Flames with Local Extinction, *Combust. Flame*, **123**:281–307 (2000).
- [48] Pitsch, H. and Steiner, H., Large Eddy Simulation of a Turbulent Piloted Methane/Air Diffusion Flame (Sandia Flame D), *Phys. Fluids*, **12**(10):2541–2554 (2000).
- [49] Steiner, H. and Bushe, W. K., Large Eddy Simulation of a Turbulent Reacting Jet with Conditional Source-Term Estimation, *Phys. Fluids*, **13**(3):754–759 (2001).
- [50] Masri, A. R., Pope, S. B., and B. D. B., PDF Computations of a Strongly Swirling Nonpremixed Flame Stabilised on a New Swirl Burner, *Proc. Combust. Inst.*, **28**:123–131 (2000).
- [51] Jenny, P., Muradoglu, K., Liu, K., Pope, S. B., and Caughey, D. A., PDF Simulations of a Bluff-Body Stabilized Flow, *J. Comp. Phys.*, **169**:1–23 (2001).
- [52] Muradoglu, K., Liu, K., and Pope, S. B., PDF Modeling of a Bluff-Body Stabilized Turbulent Flame, *Combust. Flame*, **132**:115–137 (2003).

- [53] Liu, K., Pope, S. B., and Caughey, D. A., Calculations of Bluff-Body Stabilized Flames Using a Joint Probability Density Function Model with Detailed Chemistry, *Combust. Flame*, **141**:89–117 (2005).
- [54] Raman, V. and Pitsch, H., Large-Eddy Simulation of a Bluff-Body-Stabilized Non-Premixed Flame Using a Recursive Filter-Refinement Procedure, *Combust. Flame*, **142**(4):329–347 (2005).
- [55] Hossain, M., Jones, J. C., and Malalasekera, W., Modelling of a Bluff-Body Nonpremixed Flame Using a Coupled Radiation/Flamelet Combustion Model, *Flow Turb. Combust.*, **67**:217–240 (2001).
- [56] Kim, S. H. and Huh, K. Y., Use of the Conditional Moment Closure Model to Predict NO Formation in a Turbulent CH<sub>4</sub>/H<sub>2</sub> Flame over a Bluff-Body, *Combust. Flame*, **130**:94–111 (2002).
- [57] Wouters, H. A., Peeters, T. W. J., and D., R., Joint Velocity-Scalar PDF Methods, In Launder and Sandham<sup>41</sup>.
- [58] Kuan, T. S. and Lindstedt, R. P., Transported Probability Density Function Modeling of a Bluff Body Stabilized Turbulent Flame, *Proc. Combust. Inst.*, **30**(1):767–774 (2005).
- [59] Peters, N., Local Quenching Due to Flame Stretch and Non-Premixed Turbulent Combustion, *Combust. Sci. Technol.*, **30**:1–17 (1983).
- [60] Spalding, S. B., Theory of Mixing and Chemical Reaction in the Opposed-Jet Diffusion Flame, *Journal of the American Rocket Society*, **31**:763–771 (1961).
- [61] Liñán, A., The Asymptotic Structure of Counterflow Diffusion Flames for Large Activation Energies, *Acta Astronautica*, **1**:1007–1039 (1974).
- [62] Maruta, K., Yoshida, M., Guo, H., Ju, Y., and Niioka, T., Extinction of Low-Stretched Diffusion Flame in Microgravity, *Combust. Flame*, **112**:181–187 (1998).
- [63] Smith, G. P., Golden, D. M., Frenklach, M., Moriarty, N. W., Eiteneer, B., Goldenberg, M., Bowman, C. T., Hanson, R., Song, S., Gardiner, W. C., Lissianski, V., and Qin, Z., [http://www.me.berkeley.edu/gri\\_mech](http://www.me.berkeley.edu/gri_mech)
- [64] Bowman, C. T., Hanson, R. K., Gardiner, W. C., Lissianski, V., Frenklach, M., Goldenberg, M., Smith, G. P., Crosley, D. R., and Golden, D. M., GRI-Mech 2.11—An Optimized Detailed Chemical Reaction Mechanism for Methane Combustion and NO Formation and Reburning, Report GRI-97/0020, Gas Research Institute, Chicago, IL, 1997.
- [65] De Bruyn Kops, S. M., Riley, J. J., Kosály, G., and Cook, A. W., Investigation of Modeling for Non-Premixed Turbulent Combustion, *Combust. Flame*, **60**:105–122 (1998).

- [66] DesJardin, P. E. and Frankel, S. H., Two-Dimensional Large Eddy Simulation of Soot Formation in the Near-Field of a Strongly Radiating Nonpremixed Acetylene-Air Turbulent Jet Flame, *Combust. Flame*, **119**:121–132 (1999).
- [67] Kempf, A., Forkel, H., Chen, J. Y., Sadiki, A., and Janicka, J., Large-Eddy Simulation of a Counterflow Configuration with and without Combustion, *Proc. Combust. Inst.*, **28**:35–40 (2000).
- [68] Ladeinde, F., Cai, X., Sekar, B., and Kiel, B., Application of Combined LES and Flamelet Modeling to Methane, Propane, and Jet-A Combustion, AIAA Paper 2001-0634, 2001.
- [69] Sagaut, P., *Large Eddy Simulation for Incompressible Flows*, Springer-Verlag, second edition, 2002.
- [70] Ghosal, S. and Moin, P., The Basic Equations for the Large Eddy Simulation of Turbulent Flows in Complex Geometry, *J. Comp. Phys.*, **118**:24–37 (1995).
- [71] Vreman, B., Geurts, B., and Kuerten, H., Realizability Conditions for the Turbulent Stress Tensor in Large-Eddy Simulation, *J. Fluid Mech.*, **278**:351–362 (1994).
- [72] Williams, F. A., *Combustion Theory*, The Benjamin/Cummings Publishing Company, Menlo Park, CA, 2nd edition, 1985.
- [73] Kuo, K. K., *Principles of Combustion*, John Wiley, Hoboken, N.J., second edition, 2005.
- [74] Smooke, M. D. and Giovangigli, V., Formulation of the Premixed and Nonpremixed Test Problems, In Smooke<sup>117</sup>, pp. 1–28.
- [75] Rogallo, R. S. and Moin, P., Numerical Simulation of Turbulent Flow, *Ann. Rev. Fluid Mech.*, **16**:99–137 (1984).
- [76] Wilcox, D. C., *Turbulence Modeling for CFD*, DCW Industries, Inc., La Cañada, CA, 1993.
- [77] Smagorinsky, J., General Circulation Experiments with the Primitive Equations. I. The Basic Experiment, *Monthly Weather Review*, **91**(3):99–164 (1963).
- [78] Yoshizawa, A. and Horiuti, K., A Statistically-Derived Subgrid Scale Kinetic Energy Model for Large Eddy Simulation of Turbulent Flows, *J. Phys. Soc. Japan*, **54**(8):2834–0000 (1985).
- [79] Moin, P., Squires, W., Cabot, W. H., and Lee, S., A Dynamic Subgrid-Scale Model for Compressible Turbulence and Scalar Transport, *Phys. Fluids A*, **3**:2746–2757 (1991).
- [80] Bardina, J., Ferziger, J. H., and Reynolds, W. C., Improved Turbulence Models Based on Large Eddy Simulations of Homogeneous, Incompressible, Turbulent Flows,

Department of Mechanical Engineering Report TF-19, Stanford University, Stanford, CA, 1983.

- [81] Eidson, T. M., Numerical Simulation of the Turbulent Rayleigh-Benard Problem using Subgrid Modelling, *J. Fluid Mech.*, **158**:245–268 (1985).
- [82] O’Brien, E. E., The Probability Density Function (PDF) Approach to Reacting Turbulent Flows, In Libby and Williams<sup>116</sup>, chapter 5, pp. 185–218.
- [83] Pope, S. B., The Probability Approach to Modeling of Turbulent Reacting Flows, *Combust. Flame*, **27**:299–312 (1976).
- [84] Dopazo, C. and O’Brien, E. E., Statistical Treatment of Non-Isothermal Chemical Reactions in Turbulence, *Combust. Sci. Technol.*, **13**:99–112 (1976).
- [85] Borghi, R., Turbulent Combustion Modeling, *Prog. Energy Combust. Sci.*, **14**:245–292 (1988).
- [86] Pope, S. B., Lagrangian PDF Methods for Turbulent Flows, *Ann. Rev. Fluid Mech.*, **26**:23–63 (1994).
- [87] Muradoglu, M., Jenny, P., Pope, S. B., and Caughey, D. A., A Consistent Hybrid-Volume/Particle Method for the PDF Equations of Turbulent Reactive Flows, *J. Comp. Phys.*, **154**(2):342–371 (1999).
- [88] Xu, J. and Pope, S. B., Assessment of Numerical Accuracy of PDF/Monte Carlo Methods for Turbulent Reacting Flows, *J. Comp. Phys.*, **152**:192–230 (1999).
- [89] Muradoglu, M., Pope, S. B., and Caughey, D. A., The Hybrid Method for the PDF Equations of Turbulent Reactive Flows: Consistency Conditions and Correction Algorithms, *J. Comp. Phys.*, **172**:841–878 (2001).
- [90] Arnold, L., *Stochastic Differential Equations: Theory and Applications*, Krieger Publishing Co., Malabar, FL, 1974.
- [91] Risken, H., *The Fokker-Planck Equation, Methods of Solution and Applications*, Springer-Verlag, New York, NY, 1989.
- [92] Gardiner, C. W., *Handbook of Stochastic Methods*, Springer-Verlag, New York, NY, 1990.
- [93] Sung, C. J., Law, C. K., and Chen, J.-Y., An Augmented Reduced Mechanism For Methane Oxidation with Comprehensive Global Parametric Validation, *Proc. Combust. Inst.*, **27**:295–303 (1998).
- [94] Seshadri, K. and Peters, N., Asymptotic Structure and Extinction of Methane-Air Diffusion Flames, *Combust. Flame*, **73**(1):23–44 (1988).

- [95] Bilger, R. W., Esler, M. B., and Starner, S. H., On Reduced Mechanisms for Methane-Air Combustion, In Smooke<sup>117</sup>, pp. 86–110.
- [96] Yilmaz, S. L., Ph.D. Thesis, Department of Mechanical Engineering, University of Pittsburgh, Pittsburgh, PA, 2005, In progress.
- [97] Pope, S. B., Computationally Efficient Implementation of Combustion Chemistry using *in situ* Adaptive Tabulation, *Combust. Theory Modelling*, **1**(1):41–63 (1997).
- [98] Carpenter, M. H., A High-Order Compact Numerical Algorithm for Supersonic Flows, in Morton, K. W., editor, *Twelfth International Conference on Numerical Methods in Fluid Dynamics, Lecture Notes in Physics*, Vol. 371, pp. 254–258, Springer-Verlag, New York, NY, 1990.
- [99] Poinso, T. J. and Lele, S. K., Boundary Conditions for Direct Simulations of Compressible Viscous Flows, *J. Comp. Phys.*, **101**:104–129 (1992).
- [100] Sobczyk, K., *Stochastic Differential Equations with Applications to Physics and Engineering, Mathematics and its Applications. East European Series*, Vol. 40, Kluwer Academic Publishers, Dordrecht; Boston, 1991.
- [101] Kloeden, P. E. and Platen, E., *Numerical Solution of Stochastic Differential Equations, Applications of Mathematics, Stochastic Modelling and Applied Probability*, Vol. 23, Springer-Verlag, New York, NY, 1995.
- [102] Kloeden, P. E., Platen, E., and Schurz, H., *Numerical Solution of Stochastic Differential Equations through Computer Experiments*, Springer-Verlag, New York, NY, corrected second printing edition, 1997.
- [103] Soong, T. T. and Grigoriu, M., *Random Vibration of Mechanical and Structural Systems*, Prentice-Hall, Englewood Cliffs, NJ, 1993.
- [104] Itô, K., *On Stochastic Differential Equations, Memoirs of the American Mathematical Society*, Vol. 4, American Math. Society, Providence, RI, 1951.
- [105] Gikhman, I. I. and Skorokhod, A. V., *Stochastic Differential Equations*, Springer-Verlag, New York, NY, 1972.
- [106] Pope, S. B., On the Relation Between Stochastic Lagrangian Models of Turbulence and Second-Moment Closures, *Phys. Fluids*, **6**(2):973–985 (1994).
- [107] Colucci, P. J., Large Eddy Simulation of Turbulent Reactive Flows: Stochastic Representation of the Subgrid Scale Scalar Fluctuations, Ph.D. Thesis, Department of Mechanical and Aerospace Engineering, University at Buffalo, State University of New York, Buffalo, NY, 1998.
- [108] Danaïla, I. and Boersma, B. J., Direct Numerical Simulation of Bifurcating Jets, *Phys. Fluids*, **12**(5):1255–1257 (2000).

- [109] Schefer, R. W., Namazian, M., and Kelly, J., Velocity Measurements in a Turbulent Nonpremixed Bluff-Body Stabilized Flame, *Combust. Sci. Technol.*, **56**:101–138 (1987).
- [110] Namazian, M., Kelly, J., Schefer, R. W., Johnston, S. C., and Long, M. B., Nonpremixed Bluff-Body Burner Flow and Flame Imaging Study, *Experiments in Fluids*, **8**:216–228 (1989).
- [111] Correa, S. M. and Gulati, A., Measurements and Modeling of a Bluff Body Stabilized Flame, *Combust. Flame*, **89**(2):195–213 (1992).
- [112] Kerstein, A. R., Cremer, M. A., and McMurtry, P. A., Scaling Properties of Differential Molecular Diffusion Effects in Turbulence, *Phys. Fluids*, **7**(8):1999–2007 (1995).
- [113] Vargaftik, N. B., Vinogradov, Y. K., and Yargin, V. S., *Handbook of Physical Properties of Liquids and Gases. Pure Substances and Mixtures*, Begell House, third edition, 1996.
- [114] Galperin, B. and Orszag, S. A., editors, *Large Eddy Simulations of Complex Engineering and Geophysical Flows*, Cambridge University Press, Cambridge, UK, 1993.
- [115] Geurts, B. J., editor, *Modern Simulation Strategies for Turbulent Flow*, R. T. Edwards, Inc., Philadelphia, PA, 2001.
- [116] Libby, P. A. and Williams, F. A., editors, *Turbulent Reacting Flows, Topics in Applied Physics*, Vol. 44, Springer-Verlag, Heidelberg, 1980.
- [117] Smooke, M. D., editor, *Reduced Kinetic Mechanisms and Asymptotic Approximations for Methane-Air Flames, Lecture Notes in Physics*, Vol. 384, Springer-Verlag, Berlin, 1991.